CONSTRAINING TECTONIC AND CLIMATIC CONTROLS ON GLACIAL/POSTGLACIAL LANDSCAPE EVOLUTION USING NUMERICAL MODELING

BY

JINGTAO LAI

DISSERTATION

Submitted in partial fulfillment of the requirements
for the degree of Doctor of Philosophy in Geology
in the Graduate College of the
University of Illinois at Urbana-Champaign, 2020

Urbana, Illinois

Doctoral Committee:

Associate Professor Alison M. Anders, Chair and Director of Research
Associate Professor Lijun Liu
Assistant Professor William Guenthner
Associate Director Jonathan Tomkin

ABSTRACT

Earth's dynamic surface is shaped by the interactions between surface processes, tectonics, and climate. During the Late Cenozoic, repeated glaciations have affected the landscapes of many high-latitude regions and mountain ranges around the world, including both active subduction belts and stable continental interiors. The glacial/interglacial climate perturbations have caused repeated transitions between glacial and fluvial processes. During cold glacial periods, erosion and deposition by ice sheets and glaciers has left a clear imprint on Earth's surface, creating unique landforms such as flat till plains, wide U-shaped valleys, steep mountain peaks, and deep fjords. As the climate transitioned into warm interglacial periods, these unique landforms further influenced the pace and style of postglacial fluvial and hillslope processes. How do tectonic and climatic conditions impact the rates and spatial patterns of glacial erosion? How do the inherited glacial landforms influence the development of postglacial landscapes? To answer these questions, my work focuses on exploring the sensitivity of landscape characteristics to variability in climate, tectonics, and surface process regime using numerical landscape evolution modeling. I model the hydrological connection of upland closed depressions to growing channels (via filling and spilling or through shallow subsurface flow) in postglacial low-relief till plains. My models show that connection leads to greater rates of channel network expansion and distinctive channel morphologies as compared with cases in which those closed depressions remain hydrologically isolated. To model glacial landscape evolution, I couple a sliding-dependent glacial erosion model with a sophisticated ice dynamics model. I investigate the impact of climatic and tectonic conditions on glacier basal thermal regimes and glacial erosion. Numerical simulations reveal that glacial erosion patterns follow the patterns of the basal thermal regime determined by geothermal heat and climate. I find a robust tendency for increasing glacial erosion with increasing geothermal heat flux. As geothermal heat flux increases, the area of significant glacial erosion expands into higher elevations and the location of maximum erosion migrates up-valley because high geothermal heat flux creates warm-based areas in high elevations. Climate conditions also influence the distribution of warm- and cold-based ice and, consequently, patterns of glacial erosion. Cold temperatures create cold-based glacier areas at high elevations, while high precipitation rates tend to cause warm-based

conditions by increasing the thickness of glaciers and lowering the melting point of ice. As a result, glaciers in a cold and dry climate result in limited erosion at high elevations, and most glacial erosion focuses at low elevations in major valleys. In contrast, a warm and wet climate causes a large amount of erosion at high elevations. My model results suggest that climate controls the spatial patterns of glacial erosion primarily through changing the basal thermal regime rather than altering the equilibrium line altitudes of glaciers. In addition to numerical modeling, I also analyze global digital elevation data. My analysis suggests that glacial erosion significantly increases ridge-valley relief compared with fluvial incision. The results also show that relief increases with latitude, implying that high elevation ridges might be protected from erosion by cold-based glaciers in high latitude regions. By combining numerical modeling with observations, my research provides important insights into the feedbacks and interactions between tectonics, climate, and surface processes.

ACKNOWLEDGMENTS

There are many who helped me along the way on this journey to a Ph.D., and I would like to take this opportunity to thank all of them.

I would like to express my special thanks to my advisor Dr. Alison Anders for her endless support through each stage of my Ph.D. study. Her patience and encouragement created a warm environment for me as an international student. Her expertise and guidance helped me define the path of my research and allowed me to study what I have always wanted. Her insightful feedback helped bring my research to a higher level. During the past five and a half years, she did everything to prepare me for a future career as an independent researcher. I could not have imagined having a better mentor for my Ph.D. study.

I would also like to thank the rest of the dissertation committee: Drs. Jonathan Tomkin, Lijun Liu, and Willy Guenthner, for their constructive feedback and encouragement. Jonathan is an expert in glacial landscape evolution modeling, and I benefited a lot from discussions with him. Lijun's inspiring thoughts always drove me to think about science from different perspectives. Willy's expertise in thermochronology helped me connect my modeling results to observational data.

I would like to acknowledge Dr. Nicole Gasparini for her help in setting up and developing Landlab model components. I am grateful to Dr. Andy Aschwanden and Dr. Ed Bueler for constructive discussions that helped formulate research questions and methodology. I want to thank Constantine Khrulev for his help in implementing landscape evolution models into PISM.

The Department of Geology provided me with many important resources. I am grateful to all the faculty and staff for creating a positive environment. Special thanks to Lana Holben for taking care of everything and being a supportive friend for all the graduate students. I would like to thank the Department for providing funding that allowed me to travel to so many places. The Keeling computer cluster at the School of Earth, Society, and Environment was essential for my numerical modeling research.

All the graduate students brought me so much joy on this journey. I would like to thank Yuchen Liu and Ching Chang for all the fun we had at the Texas Roadhouse. Yan Zhan is

always a good friend and I enjoyed our time at the gym. Many thanks to my groupmates, Cecilia Cullen and Nooreen Meghani for their support. I am grateful to all my officemates in Room 4065 at NHB for making our office a joyful workplace.

It is hard to express my gratitude to my parents. They have always been supportive no matter what decisions I made. Finally, I want to say many thanks to my partner, Yingfeng Yang. She gave me strength that allows me to fight and a purpose that I want to fight for. Thank you for bringing light into my life.

To my parents and Yingfeng

For their love and support

TABLE OF CONTENTS

CHAPTER 1: INTRODUCTION

Earth's dynamic surface is shaped by the interactions between lithosphere, atmosphere, and biosphere. Understanding how surface processes operate and how landscapes evolve helps is a fundamental part of a full understanding of the Earth system. Better constraints on the dynamics of surface processes enable better natural hazard assessment and environmental management. Understanding Earth's surface landscapes and potential feedbacks between different systems on Earth's surface, therefore, are crucial for both scientific communities and societies.

1.1 Tectonics, climate, and topography

It has long been recognized that topography of mountain ranges results from the competition between tectonic activities that elevate the bedrocks and erosive surface processes that are affected by climate. The feedbacks and interactions between tectonics, climate, surface processes, and topography make it difficult to fully understand how tectonics and climate influence the development of topography. Erosion/deposition directly controls the elevation and relief of mountain belts, and topography in turn affects erosion and deposition through the dependency of their rates on the gradients of channels and hillslopes. Tectonics directly affect the topography by elevating bedrock and may influence erosion rates by the fracturing of bedrock (Dühnforth et al., 2010; Molnar et al., 2007) and earthquake-triggered landslides (Dadson et al., 2003). Climate controls the rates of surface processes through different precipitation (Ferrier et al., 2013; Moon et al., 2011) and alters the dominant surface processes from fluvial to glacial processes by changing the temperature (Zhang et al., 2001). Erosion/deposition and topography could in turn influence tectonics and climate. The most obvious impact of surface processes on tectonics is that erosion/deposition could induce the isostatic uplift or subsidence of the lithosphere. Focused erosion could also modify the patterns of deformation in the lithosphere (Willett, 1999). High topography blocks the moisture in the atmosphere and creates orographic precipitation (Anders et al., 2008; Roe, 2005), and affects the atmospheric circulation. Erosion and chemical weathering of surface rocks modulate the CO_2 concentration in the atmosphere and affect the global climate (Raymo et al., 1988). Furthermore,

climate and tectonics could also affect each other directly (e.g., volcanism and climatic loading/unloading of the lithosphere).

Although the evolution of topography is complicated by tectonic and climatic controls, the topography tends to evolve towards an equilibrium state, in which the supply of rock mass provided by tectonic activities is balanced by erosive surface processes that remove the rocks. This equilibrium state partially arises from the feedbacks between the rates of surface processes and topography. For example, in a fluvial landscape, because the rates of fluvial incision and hillslope erosion depend on the slopes of topography, steep river channels and hillslopes created by rock uplift will be lowered by rapid erosion and the topography will tend to a dynamic steady state in which the channels and hillslopes are adjusted so that erosion rates balance rock uplift rates. A change in boundary conditions (for example, a sudden change of rock uplift rates) or a change in the dominant surface processes (for example, a shift from fluvial to glacial erosion due to cooling climate) may break the established balance and trigger a pulse of adjustment that may persist for 10^3 to 10^6 years (Dadson and Church, 2005; Gasparini et al., 2007; Moon et al., 2015). The morphology of a landscape that is not in a state of equilibrium, therefore, may depend more on recent changes in tectonics or climate than on the present-day configuration.

The cooling climate since the late Cenozoic is one of the most important changes in recent geological history. The cold climate has induced glaciations in polar regions and other high mountain ranges, and the legacy of glacial erosion and deposition has a profound impact on present-day topography.

1.2 Glaciation as a geomorphic process

Glaciation is a powerful geomorphic process that affects not only the development of landscapes beneath ice sheets and glaciers but also the pace and style of surface processes in periglacial regions. The growth and decay of large continental ice sheets influences the rates and patterns of surface processes around the world by loading/unloading the lithosphere, changing the sea level, and affecting atmospheric circulation. Even when the ice has melted away, the inherited glacial landforms control the pace and style of surface processes in the postglacial era (Moon et al., 2011). Feedbacks between cooling climate, intensive glacial erosion, and enhanced chemical weathering may serve as a positive feedback that promotes further cooling and glaciation (Foster and Vance, 2006).

In the past 2.6 million years, repeated glaciations have directly and indirectly affected many high-latitude regions, including northern Europe and North America, and high-altitude regions, such as the Alps, the Andes, and the Himalayas. Significant Quaternary glaciations, especially the most recent one, the Last Glacial Maximum (LGM), which reached its maximum extent around 20,000 years ago, have left a clear imprint on much of Earth's surface. During the LGM, the Laurentide Ice Sheet once covered large parts of North America, including the northern portion of the US Midwest. The Laurentide Ice Sheet eroded rocks of the Canadian Shield and transported them to the southern edge of the ice sheet, forming moraines and till plains. Depositional glacial processes filled pre-existing river valleys and disrupted previous fluvial networks. After the ice retreated, the rates and patterns of fluvial and hillslope processes are controlled by the inherited glacial landforms featuring low-relief till plains with limited drainage networks. In Chapter 2, I explore the dependency of fluvial network expansion on the hydrological connection in postglacial landscapes, using numerical modeling and observations from the glaciated northern portion of the US Midwest.

Glaciers and ice sheets erode the underlying rocks primarily through two mechanisms: 1) abrasion, the grinding away of the bedrock by rock fragments embedded in sliding ice, and 2) quarrying, the removal of large rock blocks aided by the changing pressures of overlying ice and subglacial meltwater. Erosion of localized subglacial meltwater flow also controls the formation of some glacial landforms such as subglacial tunnels, but its contribution to glacially eroded sediment budget is negligible compared with abrasion and quarrying (Beaud et al., 2016). Glacial abrasion creates a polished bedrock surface with striations, and the rate of abrasion is strongly controlled by the basal sliding velocity of glaciers (Hallet, 1979). Quarrying, also known as plucking, can detach large blocks of rock along joint planes from the bedrock. The rate of quarrying depends not only on the sliding velocity but also on the fluctuating and differential stresses exerted on a bedrock obstacle by ice and meltwater (Hallet, 1996; Iverson, 1991, 2012).

The rates of both abrasion and quarrying largely depend on the sliding velocity of glaciers, which is controlled by the basal thermal states of glaciers. A glacier could be 1) cold-based, in which the basal ice is frozen to the bed, 2) warm-based, in which the basal ice is at the pressure melting point, or 3) polythermal, in which both cold-based and warm-based portions coexist. Geomorphologists often assume that glacial erosion occurs exclusively below warm-based glaciers (Kleman, 1994; Kleman and Glasser, 2007; Thomson et al., 2010), because, under

cold-based glaciers, basal sliding is limited since the ice is frozen to the bed, while warm-based glaciers could actively slide along the bed, aided by the lubrication of subglacial meltwater. An appropriate representation of the basal thermal regime may therefore crucial for computing rates and patterns of glacial erosion in numerical models. However, previous numerical modeling studies either neglect the role of the basal thermal regime by assuming the glacier is entirely warm-based (MacGregor et al., 2000; Prasicek et al., 2018), or only include a highly simplified approximation of the thermodynamics of glaciers (Braun et al., 1999; Herman and Braun, 2008; Yanites and Ehlers, 2012). In Chapters 3 and 4, I attempt to bridge this gap by using a numerical model to address how climate and tectonics affect the basal thermal regime and consequently glacial erosion.

1.3 Landscape evolution modeling

Three decades ago, the term "landscape evolution model" simply meant a conceptual framework that describes the development of a landscape over geological time (Tucker and Hancock, 2010). The improvement of our ability to measure topography in the past two decades has driven the outburst of mathematical theories of landscape evolution that describes how specific geomorphic processes interact with the topography and drive the evolution of landscapes. Nowadays, a "landscape evolution model" now refers to the governing equations of a landscape evolution theory and the numerical methods that compute approximate solutions to the governing equations (Tucker and Hancock, 2010). Tremendous advances in modeling landscape evolution have greatly improved our ability to understand how geomorphic processes control the development of landforms and rates of landscape evolution, and to explore possible feedbacks between different components of the Earth system. In this dissertation, I use landscape evolution models for fluvial and glacial processes to explore the evolution of glacial and postglacial landscapes.

1.3.1 Fluvial processes model

Models for fluvial incision are typically classified into two end-member types: 1) detachment-limited models, in which the rate of incision is controlled by the stress exerts upon the bedrock by water and the mechanical properties of bedrock, and 2) transport-limited models, in which the rate of incision depends on the transport capacities of rivers. In postglacial

environments, the incision into glacial tills is dominated by detachment-limited processes (Gran et al., 2013).

The stream power model (Howard, 1994) is the most widely used detachment-limited fluvial incision model. The rate of incision is approximated as a power function of drainage area, A, and channel gradient, S:

$$E_f = K_f A^m S^n. \quad (1.1)$$

K_f is the erosional coefficient which incorporates the influence of climate, lithology, vegetation, and hydrology on fluvial incision. m and n are constants.

In landscape evolution models with raster grids, the water flow direction is usually determined through the D8 algorithm, in which all water leaving a cell flows toward the adjacent cell that lies in the direction of the steepest descent. In low-relief postglacial landscapes, however, the D8 algorithm provides a poor approximation of the actual flow direction because the landscapes contain many closed local depressions. Water may flow out of these depressions through shallow groundwater or spillover of surface water. In Chapter 2, I attempt to simulate the hydrological connection between closed depressions and external drainage networks and explore its impact on the development of fluvial networks in postglacial landscapes.

1.3.2 Glacial processes model

The rate of glacial erosion is commonly approximated as a function of the sliding velocity in landscape evolution models (e.g., Braun et al., 1999; MacGregor et al., 2000; Tomkin and Braun, 2002; Yanites and Ehlers, 2012):

$$E_g = K_g |\boldsymbol{u}_s|^l, \quad (1.2)$$

where K_g is an erosional coefficient and l is a constant. Field observations suggest that the value of l ranges from 1 to 2 and K_g ranges from 10^{-7} to 10^{-4} depending on the choice of l (Herman et al., 2015; Humphrey and Raymond, 1994; Koppes et al., 2015). This erosion model is supported by the theory of glacial abrasion (Hallet, 1979). Although it neglects the influence of subglacial hydrology, this model still reproduces the qualitative patterns of glacial quarrying in glacial landscape evolution models (Hallet, 1996; Iverson, 2012; Ugelvig et al., 2016).

Ice in glaciers is a slow-moving fluid and its motion follows the Stokes equations. However, solving the full Stokes equations is computationally challenging, especially for modeling glacial landscape evolution over long geological timescales. Fortunately, the thickness

of ice sheets and glaciers are often much smaller than their horizontal scales. The small depth-to-width ratio could reduce the Stokes equations into simpler forms.

Ice is a non-Newtonian flow and its deformation follows the Glen's flow law:

$$\dot{\epsilon}_{ij} = A\tau_E^{n-1}\tau_{ij}, \tag{1.3}$$

where $\dot{\epsilon}_{ij} = \frac{1}{2}\left(\frac{\partial u_i}{\partial x_j} + \frac{\partial u_j}{\partial x_i}\right)$ is the strain rate tensor, A is ice softness, n is a constant, τ_{ij} is the stress tensor, and $\tau_E^2 = \frac{1}{2}\tau_{ij}\tau_{ij}$ (using the summation convention). The value of the exponent, n, is usually 3.

The evolution of ice thickness, H, is controlled by mass continuity:

$$\frac{\partial H}{\partial t} = M - \nabla \cdot (\boldsymbol{u}H), \tag{1.4}$$

where M is the mass balance and $\boldsymbol{u}$ is vertically integrated ice velocity. The mass balance includes surface accumulation and ablation, as well as melting at the base of glaciers. The ice velocity term, $\boldsymbol{u}$, is the sum of internal deformation velocity, $\boldsymbol{u}_d$, and basal sliding velocity, $\boldsymbol{u}_s$:

$$\boldsymbol{u} = \boldsymbol{u}_s + \boldsymbol{u}_d. \tag{1.5}$$

Due to the small depth-to-width ratio of ice sheets and glaciers, the deformation velocity, $\boldsymbol{u}_d$, is often approximated using the Shallow Ice Approximation (SIA; Hutter, 1983):

$$\boldsymbol{u}_d = -\frac{2A(\rho g)^n}{n+1} H^{n+1} |\nabla h|^{n-1} \nabla h, \tag{1.6}$$

where ρ is the density of ice, g is gravitational acceleration, h is ice surface elevation, and n is the exponent in the Glen's flow law (Eq. 1.3).

The calculation of sliding velocity, $\boldsymbol{u}_s$, is more complicated than deformation velocity and the method differs in different models depending on the choice of sliding laws and stress balance schemes. A sliding law describes the relationship between sliding velocity and basal shear stress, $\boldsymbol{\tau}_b$. Most models apply a Weertman-style sliding law:

$$\boldsymbol{u}_s = -\frac{C_s}{N} |\boldsymbol{\tau}_b|^{m-1} \boldsymbol{\tau}_b. \tag{1.7}$$

C_s is a sliding coefficient, m is a constant, and N is the effective water pressure, which the difference between ice overburden pressure and meltwater pressure.

If we assume that the basal shear stress is completely balanced by the driving stress, or the basal shear stress is proportional to the driving stress, then

$$\boldsymbol{\tau}_b = f_b \rho g H \nabla h, \tag{1.8}$$

where f_b is a constant. Combining this equation with the Weertman-style sliding law will result

$$\boldsymbol{u}_s = -\frac{C_s(\rho g)^m}{N} H^m |\nabla h|^{m-1} \nabla h. \tag{1.9}$$

Many previous glacial landscape evolution models have used the above equation or its similar forms to simulate the sliding velocity (e.g., Braun et al., 1999; Herman et al., 2011; Prasicek et al., 2018; Tomkin and Braun, 2002; Yanites and Ehlers, 2012). However, the underlying assumption of this equation, that the basal shear stress is proportional to the driving stress, is open to question. In fast-sliding glaciers, the longitudinal pushing and stretching due to velocity variation is also an important component that balances the driving force (Bueler and Brown, 2009; Hindmarsh, 2006). An extreme example is the floating ice shelves whose driving force is completely balanced by internal pushing and stretching because the basal ice-water interfaces are slippery. Therefore, the membrane stress that represents such longitudinal effects should be included in the stress balance equation.

A common approach to solve the membrane is the Shallow Shelf Approximation (SSA; Morland, 1987) for which the stress balance is:

$$\frac{\partial}{\partial x_1}\left[2\bar{\nu}H\left(2\frac{\partial u_{SSA,1}}{\partial x_1}+\frac{\partial u_{SSA,2}}{\partial x_2}\right)\right]+\frac{\partial}{\partial x_2}\left[\bar{\nu}H\left(\frac{\partial u_{SSA,1}}{\partial x_2}+\frac{\partial u_{SSA,2}}{\partial x_1}\right)\right] + \tau_{b,1} = \rho g H \frac{\partial h}{\partial x_1}, \tag{1.10a}$$

$$\frac{\partial}{\partial x_1}\left[\bar{\nu}H\left(\frac{\partial u_{SSA,1}}{\partial x_2}+\frac{\partial u_{SSA,2}}{\partial x_1}\right)\right]+\frac{\partial}{\partial x_2}\left[2\bar{\nu}H\left(\frac{\partial u_{SSA,1}}{\partial x_1}+2\frac{\partial u_{SSA,2}}{\partial x_2}\right)\right] + \tau_{b,2} = \rho g H \frac{\partial h}{\partial x_2}. \tag{1.10b}$$

Here, x_1 and x_2 denote two horizontal directions, and $\boldsymbol{u}_{SSA} = (u_{SSA,1}, u_{SSA,2})$ is the horizontal velocity field corresponding to the SSA stress balance. $\bar{\nu}$ is the vertically-averaged effective viscosity:

$$\bar{\nu} = \frac{B}{2}\left(\frac{1}{2}\dot{\epsilon}_{ij}\dot{\epsilon}_{ij}+\frac{1}{2}\dot{\epsilon}_{ij}^2\right)^{\frac{1-n}{2n}}, \tag{1.11}$$

where $B = A^{-\frac{1}{n}}$ is the ice hardness.

The SSA velocities are often used as effective sliding velocities (i.e., $\boldsymbol{u}_s = \boldsymbol{u}_{SSA}$) in ice sheet models (Bueler and Brown, 2009; Winkelmann et al., 2011). Such a SIA+SSA hybrid

scheme enables the models to simulate the basal sliding velocity more accurately than the traditional equations (Eq. 1.9).

In Chapters 3 and 4, I combine the glacial erosion model (Eq. 1.2) with the Parallel Ice Sheet Model (Bueler and Brown, 2009; Winkelmann et al., 2011), an ice sheet model using the SIA+SSA hybrid scheme. In addition to better constraints on basal sliding velocity, PISM also has a better representation of thermodynamics than previous glacial landscape evolution models that only account for vertical heat transportation (e.g., Herman and Brandon, 2015; Tomkin and Braun, 2002). PISM incorporates an enthalpy-based scheme for the conservation of energy which improves the modeled basal thermal regime both in space and time (Aschwanden et al., 2012). This coupled landscape evolution model enables the simulation of glacial erosion with improved representations of glacier dynamics and energy conservation than previous models.

1.4 Overview

In this dissertation, I explore the processes that control the pace and style of landscape evolution in glacial and postglacial environments using numerical landscape evolution modeling combined with observational data. In Chapter 2, I investigate how the routing of water over the low-relief post-glacial surface influences the rate of evolution and morphology of evolving post-glacial river networks. The key finding of this work is that the connection of upland closed depressions to growing channels (via filling and spilling or through shallow subsurface flow) leads to greater rates of channel network growth and distinctive channel morphologies as compared with cases in which those closed depressions remain hydrologically isolated.

In Chapters 3 and 4, I couple a glacial erosion model with an ice sheet model with sophisticated thermodynamics to examine the sensitivities of glacier dynamics and glacial erosion to various tectonic and climatic conditions. In Chapter 3, I investigate the response of glacial erosion to increased geothermal heat flow. The model results reveal a tendency for increased glacial erosion with increasing geothermal heat flow, suggesting a novel interaction between tectonics and glacial erosion: tectonics may accelerate glacial erosion by elevating geothermal heat. In Chapter 4, I investigate the impact of climate on the patterns and rates of glacial erosion. This research suggests that climate controls glacial erosion primarily through the basal thermal regime and glacial erosion tends to be maximized at the transition between cold-based and warm-based ice. This finding challenges the traditional view that glacial erosion is

greatest at the intersection between bedrock topography and the equilibrium line altitudes of glaciers.

In Chapter 5, in order to compare numerical modeling results from Chapters 3 and 4 with actual topographic data, I calculate the geophysical relief of mountain ranges using digital elevation data. My analysis suggests that glacial erosion is more efficient than fluvial incision in creating deep valleys because glacial terrains have higher ridge-valley relief than fluvial landscapes. This finding is consistent with the numerical modeling results. The results also show that relief increases with latitude, implying that high elevation ridges might be protected from erosion by cold-based glaciers in high latitude regions.

CHAPTER 2: MODELED POST-GLACIAL LANDSCAPE EVOLUTION AT THE SOUTHERN MARGIN OF THE LAURENTIDE ICE SHEET: HYDROLOGICAL CONNECTION OF UPLANDS CONTROLS THE PACE AND STYLE OF FLUVIAL NETWORK EXPANSION

Abstract[1]

Landscapes of the US Central Lowland were repeatedly affected by the Laurentide Ice Sheet. Glacial processes diminished relief and disrupted drainage networks. Deep valleys carved by meltwater were disconnected from the surrounding uplands. The upland area lacking surface water connection to the drainage network is referred to as non-contributing area (NCA). Decreasing fractions of NCA on older surfaces suggests that NCA becomes drained over time. We propose that the integration could occur via: 1) capture of NCA as channels propagate into the upland or, 2) subsurface or intermittent surface connection of NCA to external drainage networks providing increased discharge to promote channel incision. We refer the two cases as "disconnected" and "connected" since the crucial difference between them is the hydrological connection of the upland to external drainage. We investigate the differences in evolution and morphology of channel networks in low relief landscapes under disconnected and connected regimes using numerical simulations. We observe substantially faster rates of erosion and integration of the channel network in the connected case. The connected case also creates longer, more sinuous channels than the disconnected case. Sensitivity tests indicate that hillslope diffusivity has little influence on the evolution and morphology. The fluvial erosion coefficient has significant impact on the rate of evolution, and it influences the morphology to a lesser extent. Our results and a qualitative comparison with landscapes of the glaciated US Central Lowland suggest that connection of NCAs is a potential control on the evolution and morphology of post-glacial landscapes.

[1] This chapter is published as Lai, J. and Anders, A. M.: Modeled Postglacial Landscape Evolution at the Southern Margin of the Laurentide Ice Sheet: Hydrological Connection of Uplands Controls the Pace and Style of Fluvial Network Expansion, Journal of Geophysical Research: Earth Surface, 123(5), 967–984, doi:10.1029/2017JF004509, 2018.

Keywords

post-glacial landscapes, numerical landscape evolution models, fluvial erosion, geomorphology, non-contributing area, Central Lowland of the United States

2.1 Introduction

Landscapes in the glaciated portions of the Central Lowland physiographic province (Fenneman and Johnson, 1946) of the United States were repeatedly affected by the southernmost portions of the Laurentide Ice Sheet during the Quaternary (Colgan et al., 2003; Fullerton et al., 2003). In this region, different locations have been most recently glaciated at ~25 ka (Wisconsin Episode), ~130 ka (Illinois Episode) and >500 ka (Pre-Illinois Episodes) (Fig. 2.1; Curry et al., 2011). Depositional glacial processes diminished pre-glacial relief by filling valleys and left constructional landforms including low-relief till plains and relatively high relief moraines (Brown et al., 1998; Colgan et al., 2003). As the ice retreated, meltwater collected in subglacial or proglacial lakes leaving fine-grained, sorted sediment in the form of glacial lake plains (e.g., Johnson et al., 1999). Glacial lakes episodically drained in outburst floods, carving deep valleys (e.g., Lord and Kehew, 1987; Teller, 2003). For example, Glacial Lake Agassiz stored much of the meltwater from the Des Moines Lobe following the Last Glacial Maximum, and draining of the glacial lake caused ~70 m of vertical incision of the Minnesota River Valley (Belmont et al., 2011; Gran et al., 2013). Valleys carved by meltwater incision provide the majority of the post-glacial landscape relief in areas occupied by the southern portions of the Wisconsin Episode Des Moines and Lake Michigan Lobes.

However, meltwater valleys did not provide a landscape-wide integrated drainage network (Fig. 2.2). Instead, a significant fraction of the area of low-relief till plains and glacial lake plains was occupied by closed depressions and remained unconnected to external drainage networks (e.g., Miller et al., 2009). This area is referred to by hydrologists as non-contributing area (NCA) because it does not typically contribute surface runoff to stream networks. The water table in NCA in this region is typically near or above the ground surface, resulting in poorly drained soils and, prior to the advent of intensive agriculture, large areas of wetland (Fig. 2.2). The prevalence of NCA varies as a function of the time since most recent glaciation with older surfaces characterized by well-integrated drainage networks and few undrained depressions

(Ruhe, 1952). The boundary of the Late Wisconsin Des Moines Lobe was mapped by Ruhe (1952) using the contrast in drainage network maturity between the poorly drained areas within the lobe and the mature drainage networks developed in Pre-Illinois Episode glacial till blanketed by Wisconsin Episode loess. Beyond the Late Wisconsin Des Moines Lobe boundary, fluvial networks had > 500,000 years to develop with the most recent glaciation leaving only a blanket of ~5 m of loess draped over the topography (Bettis et al., 2003).

We propose that the integration of NCA into external drainage networks could occur via at least two different paths: 1) through capture of NCA as channel heads propagate into the upland or, 2) through connection, perhaps intermittent, of NCA to the external drainage network via spillover of surface water from a closed depression or groundwater flow across surface water divides. The crucial difference between these two mechanisms is the fate of precipitation falling on the upland NCA. If the water delivered to the upland NCA is lost to the atmosphere through evapotranspiration or infiltrates into deep aquifers, then the integration of NCA requires headward extension of channels that eventually breach the drainage divide separating the NCA from the externally drained area. In this case, which we refer to as the "disconnected" case, the growth of a channel network causes drainage of upland closed depressions. Alternatively, if water that falls on the upland NCA is routed to external fluvial networks as spillover from lakes filled to capacity or as shallow groundwater flow, then this drainage of water off the uplands can cause channel incision within the established tributary and/or along surface flow paths. In this case, which we call the "connected" case, the NCA defined by subtle surface topographic divides are misnamed as the NCA do contribute to external drainage. The low relief of some post-glacial uplands coupled with the occurrence of near-surface water tables increases both the possibility of filling of shallow lakes to the point of spilling out of closed depressions and the likelihood that the groundwater divide and surface water divide are not co-located. Both of these situations allow for precipitation falling within surficial closed depressions to flow into integrated drainage networks.

We investigate the difference in morphology and rate of growth of channel networks in low relief landscapes under disconnected and connected drainage regimes using numerical simulations of fluvial and hillslope processes. We hypothesize that drainage network growth is more rapid when the landscape is hydrologically connected than when areas of internal drainage remain isolated from external drainage networks. We further hypothesize that the morphology of

channel networks grown under connected and disconnected drainage conditions differ significantly. We use a set of idealized models to test these hypotheses and then qualitatively compare our models with a real landscape in Illinois. Uncertainty in both the post-glacial and the pre-agricultural landscapes of Illinois and the glaciated Central Lowland more generally prevents a rigorous validation of the model, which is not intended to simulate the evolution of a particular place. Instead, we view the simulations and their comparison with real topography as motivating a hypothesis that channel networks in the glaciated Central Lowland reflect frequent hydrologic connection of greater portions of the landscape than expected from the surface topography as a target for future research.

2.2 Background

As process-oriented study of post-glacial drainage network development is limited, we begin by noting that drainage networks expand into un-channelized areas in a number of geomorphic settings including surfaces blanketed by debris during volcanic eruptions and surfaces emerging from water via relative base level fall. These cases motivate our exploration of network integration under conditions with hydrologically connected versus disconnected uplands. Drainage network integration in a hummocky debris avalanche that resulted from the 1980 eruption of Mount St. Helens was observed to occur under both connected and disconnected regimes (Janda et al., 1984; Simon, 1999). However, network integration at Mount St. Helens was completed within a few years, aided by the lack of vegetation to stabilize the surface and the high relief. Lower relief settings of channel network growth include passive margin great escarpments and tidal flats. Passive margin great escarpments are similar to the landscapes we are studying in that closed depressions dominate both. In the glaciated portion of the Central Lowland, valleys cut into the upland create the relief, while passive margin escarpments concentrate relief along the coast-parallel escarpment bounding a low-relief upland. Evolution of the escarpment is frequently modeled as headward propagation of channels disconnected from the upland (e.g., Colberg and Anders, 2014; Kooi and Beaumont, 1994; Matmon et al., 2002), and proceeds at very slow rates in some places (Brown et al., 2002; Heimsath et al., 2000). The upland above the escarpment typically includes a developed drainage network routing water away from the escarpment, which decreases the possibility of hydrological connection of the uplands to streams on the escarpment face relative to what may

occur on the immature uplands of the glaciated Central Lowland. Growth of channel networks on tidal flats has been observed at rates of up to meters per year (Pethick, 1969) and numerical modeling which includes the effects of vegetation, erosion and sedimentation suggest that headcutting into a disconnected upland is the major mechanism of channel network expansion on tidal flats (D'Alpaos et al., 2005).

Headward erosion of channels is a longstanding model of channel network development on immature surfaces (e.g., Dunne, 1980; Kooi and Beaumont, 1994). In a review of channel network development, Dunne (1980) differentiated between different mechanisms of runoff generation (Hortonian overland flow and shallow subsurface flow) and found that headward growth of channels is observed in both cases and theoretically requires exceeding a threshold overland flow length or a threshold drainage area, respectively. In both cases, the water supplied to the channel head is a first-order control on headward erosion (Dunne, 1980). In a detachment-limited erosion case headward migration of channel heads requires sufficient water supply and relief (Howard, 1994). We assert that detachment-limited erosion is appropriate for the fluvial networks we model based on the findings of Gran et al. (2013) who compare the modeled evolution of the Le Sueur River to measured morphology and ages of strath terraces. The LeSueur River, a tributary of the Minnesota River, incised into Late Wisconsin Episode glacial till following the catastrophic drainage of Lake Agassiz through the Minnesota River Valley (e.g., Belmont et al., 2011). The knick zone and strath terraces observed in the Le Sueur River cannot be reproduced using a transport-limited erosion model, but are better fit with a detachment-limited model (Gran et al., 2013). Glacial till is less cohesive than well-lithified bedrock, but is frequently overconsolidated when dewatered (e.g., Boulton and Paul, 1976) and has been observed to erode in stream beds in competent clasts, rather than by disaggregation. When channel heads cut into low relief landscapes with hydrologically disconnected uplands, both the water supply and the channel slope are limited and provide little energy for further headward erosion. For example, passive margin great escarpments commonly cut into uplands which slope gently away from the escarpment, limiting drainage area of channel heads above the escarpment and slowing their rates of propagation (Matmon et al., 2002). In post-glacial low relief landscapes, if the uplands are hydrologically disconnected, both water supplies and slope are limited by the low relief of topography. Therefore, we predict that growth of channels in low-relief post-glacial landscapes proceeds at slow rates when the uplands remain disconnected.

However, if surface topography does not define the true catchment supplying water to the channel head, the speed of headward erosion should increase as water from connected uplands is routed to channels, either via groundwater flow or through spillover from lakes and wetlands.

The erosion of spillways out of closed depressions is another model for the growth of channel networks that has been previously explored (Simon, 1999; Spencer and Pearthree, 2001). When a closed depression's water storage capacity is exceeded, water pours out through the lowest portion of the boundary, referred to as the spillway. If the shear stress of the flow over the spillway exceeds the threshold for incision, a channel may be carved during a spillover event, as has been studied in the context of the overtopping of earthen dams (e.g., Hanson, 1991). In addition to driving the erosion of spillways, the spillover event potentially provides an additional source of water from the upland to a channel head. This water is not derived from the drainage area of the channel but comes from a region of NCA that becomes connected during the spillover event to the external drainage network (Fig. 2.3). Thus, even if spillover events do not generate sufficient shear stress to erode channels in the low-slope uplands, they increase the erosive power of the growing channel network, favoring more rapid propagation of channel heads than in the case in which NCAs are always unconnected. In addition to surface water connection of NCA to external networks during spillover events we consider the possibility that some of the precipitation falling on NCA may be passed to external drainage networks via groundwater flow over topographic divides. The subtle topography, humid climate, and layered stack of glacial sediments present over much of the glaciated Central Lowland favor both spillover and groundwater connection of NCA and motivate our consideration of these factors as potential drivers of channel network evolution in this region.

Prior to the conversion to intensive agriculture, the glaciated Central Lowlands province hosted extensive wetlands (Zedler, 2003) indicating that surface water ponding was common, at least seasonally. At times of high water, spillover from closed depressions is likely to have connected to external drainage networks. Gradual sedimentation in closed depressions diminished their storage capacity over time, increasing the likelihood of spillover events. The shallow depth of the water table and low relief of upland topography favors the lateral transport of groundwater from uplands to fluvial networks. The surficial geology of the Central Lowlands typically includes tens to more than a hundred meters of glacially-derived sediments including till, outwash, and loess (Soller et al., 1999). Deposits of sorted sand and gravel occur in a range

of geometries including isolated lenses, long and thin stringers, and thin laterally extensive sheets above basal till (Grimley et al., 2016a). Permeability contrasts between glacial till and outwash promote lateral flow within sorted sediments typically found at the upper surface of till sheets (Atkinson et al., 2014). Additionally, lateral flow of water at the interface between loess and underlying till is observed in streambanks. Contributions of groundwater from beyond the surface water divide to streamflow in a formerly glaciated, generally low-relief basin in Ontario have been suggested by Dickinson and Whiteley (1970) based on observations of spring discharge and streamflow. Additionally, in the Prairie Potholes region of North Dakota, glaciated during the Wisconsin Episode, groundwater flow directions have been observed to reverse during dry versus wet years, requiring groundwater flow across surface water divides (Winter and Rosenberry, 1998). Therefore, the connection of upland closed depressions to external drainage networks is plausible in the glaciated portions of the Central Lowlands of the United States.

We explore the ramifications of such connections for the pace of evolution and the morphology of drainage networks using a set of numerical simulations. We hypothesize that channel networks can expand more rapidly into low-relief glacial uplands when water from these uplands is routed to growing channels than if upland NCAs remain hydrologically disconnected and that network morphology differs in these two cases. We test this hypothesis by comparing the relative rates of channel network integration in connected and disconnected drainage regimes in a numerical landscape evolution model build on the LandLab platform (Hobley et al., 2017) and consider a wide range of parameter values for the fluvial incision constant and hillslope diffusivity.

2.3 Methods

We use the Landlab model platform (Hobley et al., 2017) to simulate the evolution of post-glacial landscapes, starting from a flat low-relief surface. The surface evolves via detachment-limited fluvial incision and hillslope diffusion. The model is coupled with a new flow routing algorithm (Barnes et al., 2014a) that represents upland connection by spillover of water from closed depressions.

2.3.1 Governing equations

The model presented here simulates the evolution of upland topography relative to a pre-existing valley incised by meltwater. The elevation, *h*, measured relative to a base level is constrained by conservation of mass, giving:

$$\frac{dh}{dt} = U - \nabla \cdot \boldsymbol{q}, \tag{2.1}$$

where *t* is time, $\boldsymbol{q}$ is the volume flux of transportable sediment per unit width of the land surface, *U* is the rate of change of elevation relative to base level, and ∇ represents divergence of a variable. We assume that U is 0 because the Central Lowlands are tectonically stable. Postglacial isostatic adjustments are neglected because of the complicated temporal history and relatively low magnitude of isostatic change in this region. Migration of the forebulge through the Central Lowland caused changes in sign of the isostatic motion through time with current rates of subsidence of ~1mm/yr in much of the province (Sella et al., 2007). The impacts of this wave of uplift and subsidence may have driven incision of large rivers, but we examine the growth of small tributaries to a large valley incised during glacial melting and assume that the incision of the master valley was larger than any later isostatic response. The total sediment flux, $\boldsymbol{q}$, includes fluxes through fluvial processes and hillslope processes. The sediment flux therefore can be expressed as a sum of these components:

$$\nabla \cdot \boldsymbol{q} = \nabla \cdot \boldsymbol{q_f} + \nabla \cdot \boldsymbol{q_h}, \tag{2.2}$$

where $\boldsymbol{q_f}$ is fluvial sediment flux and $\boldsymbol{q_h}$ is hillslope sediment flux.

Fluvial sediment transport (q_f) requires both detachment of bed material and transport of these materials. Following Gran et al. (2013), we use a detachment-limited erosion rule for incision into glacial till. We assume all of the sediments are moved out of the model domain and deposition of sediment is not allowed. Specifically, we use the stream-power law with a threshold to represent the fluvial erosion process (Howard, 1994; Whipple and Tucker, 1999), which gives the fluvial sediment flux as:

$$\nabla \cdot \boldsymbol{q_f} = K(A^m S^n - \theta_c). \tag{2.3}$$

In the above equation, *K* is the effective fluvial erosion coefficient, *A* is drainage area, *S* is slope, *m* and *n* are positive constant, and θ_c is a threshold minimum power required for channel formation. *K* is a dimensional coefficient that is sensitive to lithology and climate with units of $L^{1-2m}T^{-1}$. We use standard *m* and *n* values of 0.5 and 1(Whipple and Tucker, 1999). Many

landscape evolution models using the stream power incision law include an erosion threshold or critical shear stress required to initiate erosion (e.g., Howard, 1994; Perron et al., 2008). A field study in the coastal mountains of Oregon and California (Montgomery and Dietrich, 1992) found that at channel heads, the product of slope and the square root of drainage area ($A^{0.5}S$) is on the order of 10 m. In the low-relief landscapes of the Central Lowland, we know of no similar analysis of the relationship between slope and drainage area at channel heads. The pervasive and extensive modification of this landscape for agriculture, including both extension of the drainage network to 2-3 times its pre-settlement length by ditching (e.g., Rhoads et al., 2016) and the creation of grassed waterways, designed to drain surface runoff while preventing gullying (Chow et al., 1999), make it difficult to identify pre-agricultural channel heads or assess their slopes prior to human modification. Acknowledging the poor analogue to Montgomery and Dietrich (1992), we use their threshold value of 10 m as we have no better constraint. The threshold for incision is crucial to include because we solve the equations on a finely-spaced grid and do not expect that fluvial incision can be assumed to occur within each grid cell.

We idealize hillslope processes with a diffusion equation as is commonly done for landscapes with low to moderate hillslope gradient (e.g., Perron et al., 2008). Specifically, the hillslope sediment flux is proportional to the topographic gradient:

$$\boldsymbol{q_h} = -D\nabla h, \tag{2.4}$$

where D is the diffusivity and ∇h represents the topographic gradient. Our modeled landscapes have low relief and low hillslope gradient, making Eq. 2.4 an adequate description of hillslope processes.

With our assumptions, Eqs. 2.1-2.4 yield a description for the time evolution of the topography:

$$\frac{dh}{dt} = -K(A^m S^n - \theta_c) + D\nabla^2 h. \tag{2.5}$$

2.3.2 Model

We discretize Eq. 2.5 and numerically solve it using the modeling platform LandLab (Hobley et al., 2017). LandLab is an open-source community model that allows users to couple surface process modules acting on a gridded terrain. Existing Landlab modules allow for representation of diffusive hillslope transport and threshold stream-power based fluvial incision. We model fluvial erosion through *FastscapeEroder* module, and we use *LinearDiffuser* module

to represent hillslope processes. The *FlowRouter* module can calculate flow direction and accumulation from topography based on the steepest decent (D8) algorithm. We develop and implement two additional modules to represent the filling and spilling of isolated depressions. The *PitFiller* module implements the priority-flood depression-filling algorithm described by Barnes et al. (2014b). This module fills the depressions by flooding the whole domain inwards from the open boundaries, and a priority queue is used to guarantee that all the depressions are filled up to their spillover points. The *FlowRouterOverFlat* module calculates the flow direction across topography with flats created by the *PitFiller* module. This approach is presented by Barnes et al. (2014a), and it operates by calculating a gradient away from higher edges of depressions as well as a gradient towards lower edges of depressions, resulting in a convergent flow field without changing the actual topography.

We differentiate between connected and disconnected upland cases by considering two different flow routing schemes across the land surface. In the disconnected case, the flow routing method is D8 algorithm, that is, the water is passed to a single neighboring cell along the path of steepest descent. Precipitation falling into the catchments of closed depressions is assumed to evaporate or infiltrate into deep groundwater. Thus, there is no hydrologic connection between the closed depressions and the incised valley. Alternatively, in the connected case we assume that all the closed depressions are always filled with water to their spill points and precipitation falling on the upland flows through these lakes and across flat land surfaces into the river channel network. The routing of flow across flats is similar to common conditioning of DEMs to force all areas to be externally drained. In this case, water added to channels provides additional energy for the propagation of channel heads into the upland. There is no erosion of flat surfaces along flow paths because stream power erosion goes to zero where the slope is zero. The routing used in the connected case is a reasonable simulation of the surface pathways for water spilling out of closed depressions and contributing to channel networks. This routing is not necessarily a good approximation of how groundwater may be routed and future work is needed to explore other potential routing scenarios. Nevertheless, we suggest that the rate of network evolution in the connected case is likely fairly insensitive to the routing scheme given the assumption that all NCA actually contributes water to external drainage networks. Thus, our simulations likely provide an illustration of the first-order impact of connected versus disconnected NCA on channel network evolution even if connection is largely occurring through groundwater flow.

In all cases we use drainage area as a proxy for precipitation, which is equivalent to imposing a steady and uniform precipitation rate. We do not model stochastic storm events and do not explicitly model discrete spillover events or erosion of spillways. Instead we focus on the integrated effects of connected uplands versus disconnected uplands. We acknowledge that an intermediate condition between the two end-member scenarios we model is more likely to have occurred in the real landscapes of the Central Lowlands but chose to focus on identifying the differences in evolution rate and channel morphology for the end-member cases as a means of constraining the potential importance of routing for network evolution.

2.3.3 Spatial domain, initial conditions, and boundary conditions

The model domain is a 5 km square grid of 10 m by 10 m pixels. The size of this domain is consistent with typical spacing of meltwater valleys in Central Lowland. The initial conditions of the model include a low-relief upland surface. We use a high-resolution model to allow for future investigations of the impacts of small-scale glacial geomorphic features such as ribbed moraines and subglacial fluting on channel network evolution. For this first study, we use a flat upland surface represented by a mean elevation with noise normally distributed about zero with a standard deviation of 0.4 m. This initial condition is meant to simulate a glacial lake plain, which represents an end-member of a homogeneous surface with no preferred flow directions. The noise is chosen to be similar to that observed presently in some glacial lake plains from the Central Lowland that date from the Late Wisconsin glaciations. Specifically, 1-m resolution LiDAR data from the bed of Glacial Lake Minnesota in southwestern Minnesota has a standard deviation of 0.67m about a constant mean elevation. Similarly, the standard deviation of elevation in a 1-m resolution DEM of the Glacial Lake Leveritt basin of south-central Illinois is 0.34 m. All simulations start from the same initial seed so that differences in channel networks between cases do not result from the initial condition. We note that in the connected flow routing case the initial topography determines the size and shape of the catchments providing water to the open boundary.

The left boundary of the domain is open in terms of flow routing, which means that mass can flow across this boundary. The other three boundaries are closed and do not allow mass transfer across them. These boundary conditions slow the growth of channels as the domain approaches a fully-integrated channel network, however, for the majority of our simulation the

channel network does not approach full integration. The open boundary represents an important component – the valley incised by meltwater at the end of the most recent glaciation. Its elevation is determined by a prescribed meltwater valley depth. The depth of such valleys is usually several tens of meters: the upper Sangamon River valley in central Illinois is 10-20 m deep, the Minnesota River catastrophically carved a 70 m deep valley during drainage of Glacial Lake Warren (Belmont et al., 2011), the Illinois River carved a gorge ~40-50 m deep during the Kankakee Torrent (Hajic, 1990), and the Wabash River carved a similar valley ~30-40 m deep (Wayne and Thornbury, 1951). We impose a valley depth of 40 m in our model. The incised valley has no slope and acts only as a boundary of the domain, imposing a base level on tributaries. The other three boundaries have the same elevation as the uplands. All the boundaries have fixed elevations for the duration of the model run.

2.3.4 Experiment design

The simulations presented in this paper were run for 30,000-1,500,000 years. The duration of the model runs is comparable to the range of time since most recent glaciation observed across the southern margin of the Laurentide Ice Sheet in the Central Lowlands (Fig. 2.1, Curry et al., 2011; Roy et al., 2004). Our model therefore represents various stages of post-glacial evolution, or, equivalently, fluvial network development on surfaces of different age. *FastscapeEroder* module in LandLab uses implicit time integration to ensure stability. We explored a range of time steps to check for convergence, and based on these results, we use a time step of 100 years as it is stable and efficient for long-term simulations.

We explored the sensitivity of the model to variation in the erosional parameters – fluvial erosion coefficient, K and diffusivity, D. We use values 0.001, 0.0001, and 0.00001 for K. We also examined cases with values 0.01, 0.001, and 0.0001 for D. These values are in the range typical of numerical landscape evolution models (e.g., Han et al., 2015; Perron et al., 2008). The fluvial erosion coefficient represents effects of both lithology and climate (Whipple and Tucker, 1999). High values of K represent wet climates and/or easily eroded bedrock. We find that the impact of variation in K in the disconnected case is minimal. Similarly, we do not observe substantial impacts on the morphology and evolution of landscapes as a result of changes in D for both the connected and disconnected cases. Therefore we focus on two different flow routing

schemes, representing connected NCA with different values of *K* (Experiments C_base, C_soft and C_hard) and disconnected NCA (Experiment D_base) (Table 2.1).

2.4 Results

2.4.1 Disconnected vs. connected

Our primary goal is to determine the impact of two different flow routing schemes on the rate of growth of channel networks and morphology of modeled landscapes. Unsurprisingly, tributary channels grow much more quickly in the connected case than in the disconnected case (Fig. 2.4). When the upland NCA remains disconnected from the external drainage network, most of the upland remains unchanged after 50,000 years of evolution (Fig. 2.4d), and channel growth occurs only near the pre-existing valley. In contrast, in the connected case, several long channels have begun to dissect the upland after 50,000 years of evolution (Fig. 2.4a). Fluvial erosion is sensitive to the fluvial erosion coefficient (Fig. 2.4a-c), but the importance of flow routing is greater. When the fluvial erosion coefficient is one order of magnitude smaller, the connected case still produces longer channels than the disconnected case with unchanged fluvial erosion coefficient (Fig. 2.4c and d). Additionally, the channels in connected cases show more variation in length, and they are more sinuous than channels in disconnected cases (Fig. 2.4).

We quantify the evolution of channel networks by calculating the percent of the domain which is connected by a strictly downslope path to the pre-existing incised glacial valley and refer to this quantity as "integrated" into the external drainage network. The faster rate of channel expansion in the connected case results in more rapid increase in integrated area than in the disconnected case (Fig. 2.5a). The increase in integrated area is equivalent to the decrease of NCA. Thus, both connected and disconnected cases predict that NCA becomes integrated over time (Fig. 2.5a). After 50,000 years of evolution, in the disconnected case, less than 5% of the initial NCA has become integrated into the channel network (solid gray line in Fig. 2.5a). In the connected, however, almost 30% of the initial NCA becomes integrated after 50,000 years (solid black line in Fig. 2.5a). The rate of integration is sensitive to the fluvial erosion coefficient, but the flow routing scheme is still the primary control on integration. Even when the fluvial erosion coefficient is one order of magnitude lower, the increasing rate of percent integrated in the connected case is still faster than the disconnected case (dashed black line in Fig. 2.5a).

The increase in percent integrated in the disconnected case (gray line in Fig. 2.5a) is more linear than in the connected case, showing that the channel network grows at a constant rate. In the connected case, the integration and channel growth are initially rapid and decrease over time (Fig. 2.5a).

We also compute the volume of material eroded within the domain as a function of time. The rate of volume loss follows a similar pattern to that of integration (Fig. 2.5b). The volume loss rate in the disconnected case is much smaller than in the connected case, and it is constant over time (black and gray solid lines in Fig. 2.5b). In the connected case, the volume loss rate increases early in the simulation, reaches a peak value after ~12,500 years, then the rate starts to decrease. Flow routing is an important control on volume loss rates, but the fluvial incision constant also plays a strong role. When the fluvial erosion constant is an order of magnitude smaller in the connected case, it produces a trend in total erosion that is similar to the disconnected case (black dashed line and gray solid line in Fig. 2.5). This result indicates that there is a significant difference in the relationship between integration and total volume loss in the connected versus the disconnected cases. We probe this difference by comparing landscapes at the same state of drainage integration in the connected and disconnected cases.

Different flow routing regimes result in different landscape morphology even when the same fraction of the landscape is integrated into external drainage networks (Fig. 2.6). For a base case fluvial erosion constant 15% of the landscape is integrated in 25,600 years in the connected case and 1,326,000 years in the disconnected case (Fig. 2.6a and d). Fluvial networks in the connected case have longer and more sinuous channels than the disconnected case. The channels in the disconnected case are closely spaced and of similar length. Many channels in the disconnected case are 500-1000 m long (Fig. 2.7d). In contrast, in each of the connected cases, there are several long channels that are over 1 km long, and their lengths are more variable (Fig. 2.7b) than channels in the disconnected case. Both connected and disconnected cases generate many short channels that are less than 500 m (Fig. 2.7a and d).

The total eroded volume required to accomplish the same amount of integration of the landscape into external drainage networks is very different in the connected and disconnected cases (Fig. 2.8). To accomplish the same degree of integration, the connected case removes much less sediment than the disconnected case, indicating that the connected case is more efficient in integration than the disconnected case. For example, when 10% of the upland is integrated, the

total volume loss in the disconnected is twice as much as the connected case (black and gray solid lines in Fig. 2.8a). In the disconnected case the rate of erosion is much slower and the total amount of erosion needed to achieve integration is larger than in the connected case. Thus the very slow evolution of the disconnected case depends on both slow rates of erosion and inefficiency of erosion in producing integration of area into external drainage networks.

The difference between the disconnected and connected cases in their efficiency of integrating area into external drainage networks creates significant differences in hypsometry (Fig. 2.9). When 15% of the upland is integrated, in the connected case, 40% of the integrated area remains high and does not change much compared to initial elevation (black solid line in Fig. 2.9b). In the disconnected case, however, only 10% of the integrated area remains high (gray solid line in Fig. 2.9b). Instead, 40% of the integrated area is lower than the half-depth of the pre-existing valley.

The difference in efficiency of erosion and integration between the connected and disconnected cases can also be observed by comparing the net erosion and percent integrated when the accumulated discharge is the same (Fig. 2.10). Essentially, this is comparing the landscapes under the two flow routing regimes when they have been shaped by the same amount of flow out of the domain. The accumulated discharge is computed by assuming a precipitation rate of 1 m/year and summing the product of drainage area and precipitation within the integrated portion of the landscape through time. Total erosion and percent integrated in the disconnected case initially changes more rapidly with increasing accumulated discharge than the connected case (gray solid line versus black solid line in Fig. 2.10). The disconnected case is more efficient at erosion than the connected case when the accumulated water volume is less than ~800 km^3 (black and gray solid lines in Fig. 2.10a). Similarly, the disconnected case results in higher fraction of integrated area when the accumulated water volume is less than ~300 km^3 (black and gray solid lines in Fig. 2.10b). However, at higher accumulated discharges, the connected case saw more total erosion and greater amounts of integration than the disconnected case, indicating that the efficiency of integration and erosion increases relative to the disconnected case as greater volumes of water act on the landscape.

In summary, when the depressions on the upland are hydrologically connected, the growth of channel network is faster than when the depressions are disconnected. The channel network in the connected case has longer and more sinuous channels than the disconnected case.

The same degree of integration in the disconnected case requires more erosion and produces a landscape with much more low-elevation area relative to the connected case. Holding the volumes of water constant shows that the disconnected case is more efficient than the connected case at eroding and integrating the drainage network only for limited volumes of accumulated discharge.

2.4.2 Sensitivity to fluvial erosion coefficient

We tested the sensitivity of our results to variation in the fluvial erosion constant and the hillslope diffusivity in the connected and disconnected cases. Changing the value of diffusivity to 0.01 and to 0.0001 has minimal impact on the evolution and morphology of landscapes, although higher diffusivity values do result in fewer tributary channels. However, the fluvial erosion coefficient, K, does significantly impact the rate of landscape evolution and also influences morphology to a lesser extent.

A high value of the fluvial erosion coefficient results in faster growth of channel network. After 50,000 years evolution, Experiment C_soft has longer and wider channels and larger integrated area than cases with lower *K* values (Fig. 2.4). Over 50% of the whole domain becomes integrated after 50,000 years in Experiment C_soft (black dash-dotted line in Fig. 2.5a). In contrast, less than 5% is integrated after 50,000 years in Experiment C_hard (black dashed line in Fig. 2.5a). High values of the fluvial erosion coefficient also create high total erosion rates (Fig. 2.5b).

The fluvial erosion coefficient also has control on the landforms when the percent of integrated area is the same. When *K* is higher, the fluvial network has shorter channels (Fig. 2.7), but there are more tributary channels (Fig. 2.6). However, fewer tributaries in the low *K* cases might be a result of diffusion, because the low *K* cases need more time to accomplish the same degree of channel integration than high K cases, allowing more time for diffusion in the low *K* cases. When the same percent of integration is accomplished, the cases with higher values of *K* cause more overall erosion (Fig. 2.8), and in consequence, there are more areas with high elevations preserved in the low *K* cases.

The connected case with a low value of *K* (Experiment C_hard) has the highest efficiency of integration (black dashed line in Fig. 2.8a). Although Experiment C_hard has a very slow erosion rate, more parts of the upland are integrated than in other connected cases when the same

amount of material is eroded (Fig. 2.8). In other words, when K is higher, the fluvial network is more efficient at erosion but less efficient at integration. Thus, the efficiency of integration is not equivalent to the efficiency of erosion. In the case with the low value of K, channels are shallowly incised and erosion of tributary valley walls is very limited, meaning that network integration occurs with minimal mass removal. In contrast, when the value of K is larger, channels are wider and more deeply incised into the upland and more material is removed for the same degree of network integration.

2.5 Discussion - fundamental importance of hydrologic connection

In our numerical model the connection or disconnection of NCA on the uplands to growing channels has profound implications for both the rate and style of drainage network growth. The fundamental importance of connection to the modeled evolution motivates careful consideration of the potential role of hydrological connection of the uplands in driving evolution of the landscapes of the glaciated Central Lowland of the United States.

The majority of the landscape in central North America has been extensively modified to allow for intensive agriculture. Channel networks have been artificially extended by ~300% in the Upper Sangamon River Basin of East-Central Illinois, for example (Rhoads et al., 2016). This post-settlement modification of landscapes means that there are very few opportunities to observe hydrologic processes as they would have been before intensive agriculture. Prior to agricultural development, ponds, lakes, wetlands and sloughs were common in the wet prairies of central Illinois (Winsor, 1987). The western Canadian Prairies are similar to the Central Lowland in their glacial history and the lack of a well-defined, externally-draining fluvial network. Instead, much of the land drains to seasonal or persistent wetlands or sloughs (Stichling and Blackwell, 1957). In this environment, wetland closed depressions have variable connection to streams over time, acting as non-contributing area when water levels are low and episodically connecting and discharging into stream networks when full (Shook and Pomeroy, 2011). It is reasonable to assume that these wetlands also contributed episodically to streamflow via filling and spilling. Therefore, we believe that the connection of NCA in the glaciated Central Lowland may have occurred in these landscapes prior to anthropogenic modification and extension of the drainage networks.

The pace of network growth in our numerical model as well as the form of the modeled channel networks can be qualitatively compared to landscapes of the Central Lowland. However, we emphasize that our numerical model is not meant as a simulation of the evolution of a particular place but as an idealization of processes contributing to post-glacial evolution. Therefore, we qualitatively compare characteristics of a channel network developed on late Wisconsin episode low-relief till plains adjacent to the Sangamon River Valley incised during the end of this most recent glaciation (Fig. 2.11) to our modeled landscapes.

The Upper Sangamon Valley, in East Central Illinois, carried meltwater of the Lake Michigan Lobe during its retreat following glaciation approximately 20,000 years ago (Grimley et al., 2016b, 2016a). Moraines define the drainage divide around most of the basin except the north-east boundary below the Champaign Moraine. South of the Champaign Moraine, the Sangamon Valley incised ~15m and tributaries developed on both sides of the valley (Fig. 2.11). On the southern side of the lower valley, short tributaries incise into the Cerro Gordo Moraine and Camp Creek breaches the moraine. The high relief of the moraine likely contributed to active channel incision here. In contrast, on the northern side of the valley the drainage divide is not defined by a glacial moraine, but a broad low-relief plain separates the Sangamon basin from the Salt Creek watershed to the north. Prior to agricultural drainage, the area between the Sangamon River and Salt Creek included significant areas without incised streams. Three longer tributaries of the Sangamon (Friends Creek, Goose Creek and Madden Creek) were likely connected to the main stem of the Sangamon River prior to incision (Rhoads et al., 2016). Broad convexities in the long profiles of these streams suggest that knick zones generated by incision of the Sangamon have propagated upstream, though typical slopes of $\sim 10^{-3}$ make these features difficult to measure (Rhoads et al., 2016). Smaller tributaries on the north side of the basin have a distribution of lengths including many channels with lengths of several kilometers (Fig. 2.11). We mapped these channels using a 1-m resolution DEM derived from LiDAR (ISGS) along with georeferenced DRG maps of the original USGS paper topographic quadrangle maps. The location of the pre-agricultural channel head was estimated for these channels by eye using valley morphology and channel straightness to assess channelized reaches. We assume that ditching extended from the pre-agricultural channel head and that straightening of natural streams was limited, making our length estimates minimum values. Channel lengths were measured by digitizing stream segments from the channel heads down slope to meet the incised

Sangamon Valley. Over the ~45km length of the reach, we measure ~100 channels on the northern side of the valley with lengths > 100m (Fig. 2.11). Within the area shown in Fig. 2.2, a domain the same size as our model domain, we measure 20 channels longer than 100m, including seven longer than 1km. Our numerical model with disconnected flow routing is unable to produce channels of this length or variety of lengths. In contrast, our model with connected flow routing does produce channels with a range of lengths, including lengths of more than a kilometer, over timescales of ~25,000 years (Fig. 2.7). We stress that our model is not meant as a simulation of evolution channels in the Sangamon Basin, and we cannot be certain of the post-glacial topography or geometry of the channel network at the time of incision of the Sangamon. We simply compare the channel network to our model to suggest that connection of NCA to external drainage networks may have influenced their evolution, motivating future work aimed at reconstructing the history of fluvial network growth and hydrological connection in the Central Lowland of the United States.

Having established that the pace of evolution and morphology of modeled channel networks formed via connected drainage regimes is plausibly similar to that observed in real systems we consider what the qualitative impact of temporal variability in climate and connection of NCA may have been. First, we recognize that the endmember scenarios of disconnected and connected drainage are unlikely to be realized in the real system – an intermediate case with connection occurring in some places for a fraction of the time is more likely. The modeled integration rate is much faster in the connected case than in the disconnected case, suggesting that even if the connection of NCA is intermittent and only occurs during a small fraction of the time, it may still dominate the expansion of channel networks. The climate of the Central Lowland during the Holocene was very dynamic. Holocene pollen data documents broad-scale migration of the forest/prairie border, suggesting that precipitation decreased in the early Holocene and increased again in the late Holocene (Bartlein et al., 1984). Changes in vegetation and precipitation are both likely to have significantly influenced landscape evolution. Changes from forest to prairie vegetation are likely to have strongly influenced the resistance to erosion at the channel head. Therefore, we expect that values of the fluvial incision constant, K, should change with vegetation type. An increase in precipitation can accelerate erosion by increasing surface runoff. Moreover, the connection of NCA via filling and spilling is more likely to happen under wet conditions. Thus, intervals of connection were likely limited to or

more frequent during wet periods, and the channel networks present may dominantly have evolved under wetter than average conditions.

In our model, the connection of NCA is via flow paths that would be expected for un-channelized surface flow spilling out of closed depressions. Groundwater flow is another potential way to add water from NCA on uplands to external drainage networks. The presence of strong permeability contrasts in the subsurface due to layering of glacial till, outwash, and loess favor lateral flow of water. The existence of a shallow water table near the surface, especially in wet conditions, also supports lateral flow at shallow depths. Observations from North Dakota within the prairie potholes region document reversals in the direction of water movement between wetlands and groundwater accompanying cycles of drought and wetter conditions(Winter and Rosenberry, 1998). We have not attempted here to model the paths of subsurface flow, but suggest that groundwater routing in the wet and low-relief post-glacial setting of the pre-agriculture Central Lowlands is an interesting target for future research. We predict that connection through subsurface flow would result in a similar rate of drainage integration as in the case of connected surface flow, but anticipate a different planform evolution channel network because surface topography would not control flow routing. We note that the planform channel network in our current model is strongly dependent on the initial conditions because the initial allocation of water to the edge of the main valley depends on the initial topography. Depending on the routing scheme developed to model groundwater routing, surficial initial conditions would likely become less important to the planform evolutions.

In conclusion, in our numerical model the connection and disconnection of NCA in uplands have significant impacts on both evolution and morphology of post-glacial landscape. When upland closed depressions are connected to external drainage, much faster rates of erosion and integration, and longer, more sinuous channels occur than when upland NCA remain disconnected. The connected case accomplishes the same degree of integration with lower total erosion than the disconnected case. Although it is difficult to observe such hydrologic connection in today's landscape due to extensive agricultural activities, a simple comparison between real landscapes and model results suggests that hydrologic connection of NCA could have had a profound importance in the evolution of post-glacial landscapes in Central Lowland of the United States.

2.6 Figures and tables

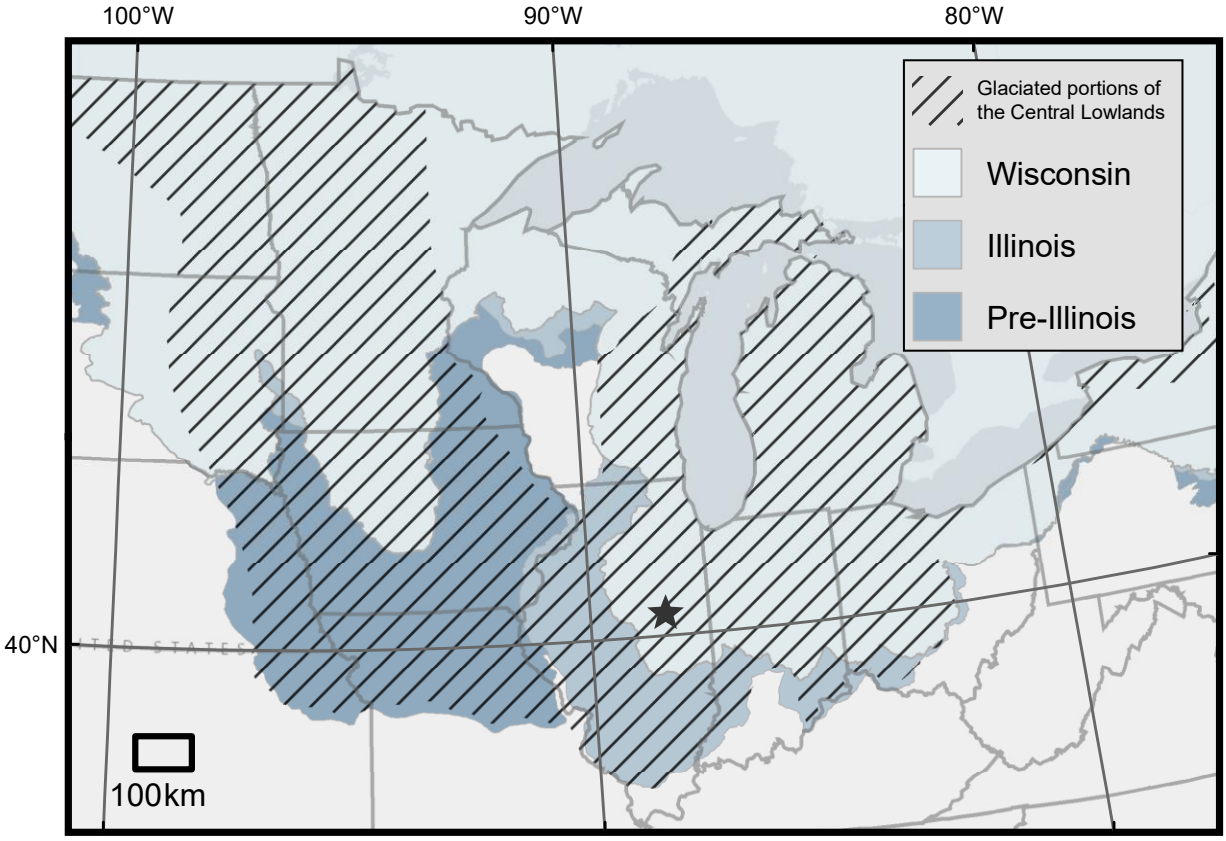

Figure 2.1 The glaciated portions of the Central Lowlands of the Interior Plain physiographic province of the United States (Fenneman and Johnson, 1946) are indicated by the hashed line. Within this region, ice advanced many times during the Pleistocene with different portions glaciated most recently during the Wisconsin Episode (Marine Isotope Stage (MIS) 2-4), shown in light blue, the Illinois Episode (MIS 6), shown in medium blue, and during multiple episodes in the early and middle Pleistocene, referred to as Pre-Illinois Episodes (Fullerton et al., 2003). This region, therefore, contains areas most recently glaciated ~10,000 years ago and areas most recently glaciated > 500,000 years ago. The star symbol shows the location of Upper Sangamon River basin in east-central Illinois.

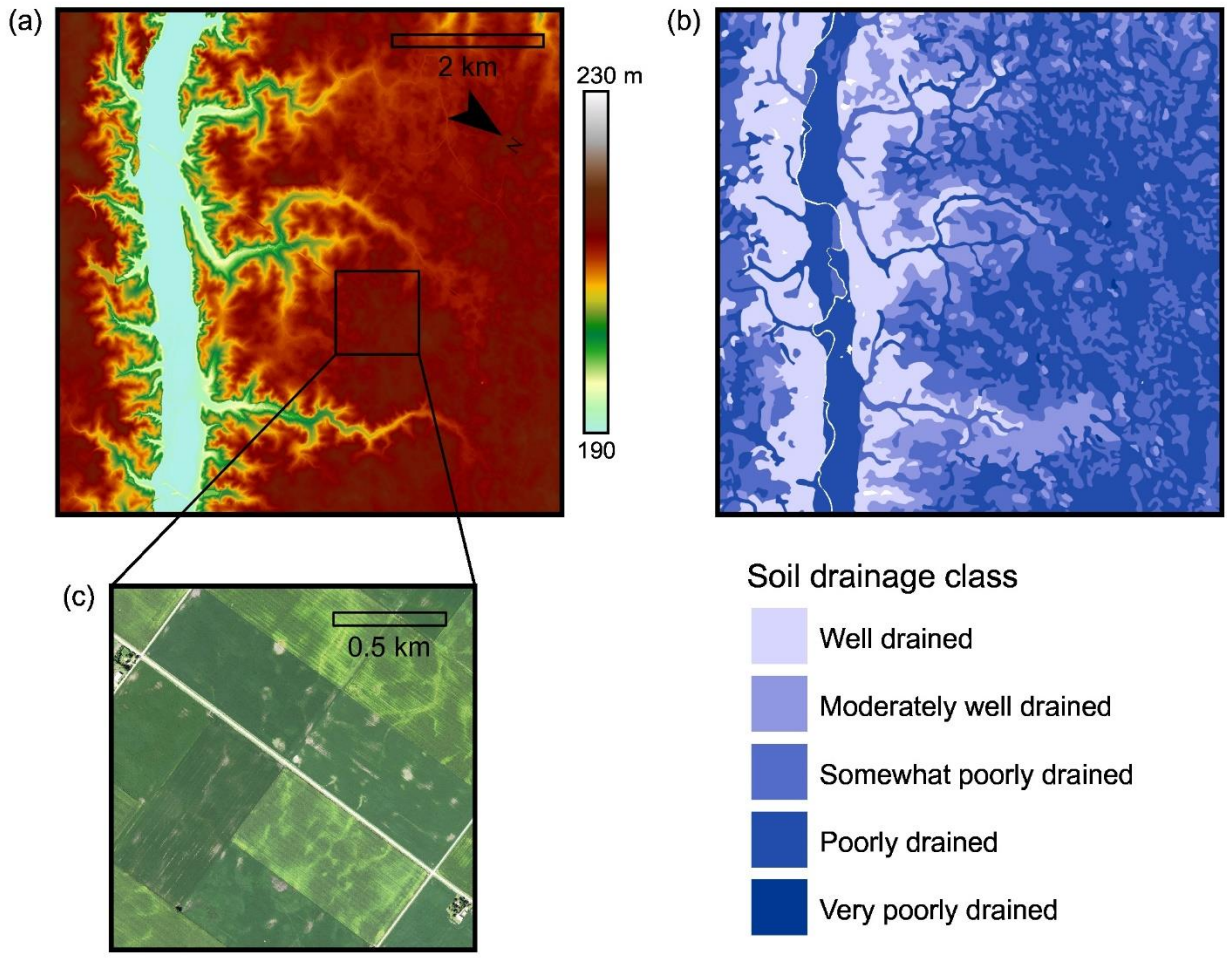

Figure 2.2 Panel a, a 1-m resolution DEM constructed from LiDAR data (ISGS) from the Sangamon River in East-Central Illinois, shows an incised valley ~15m deep cut during recession of Late Wisconsin Episode glaciers ~20,000 years ago (Grimley et al., 2016a). Three large tributaries extend from the north-west side of the valley into a flat, low-relief upland that lacked integrated drainage prior to agricultural ditching. Soil survey data in panel b (retrieved from Web Soil Survey, see references), colored by drainage class, show that soils formed under very poor drainage are common across the upland, indicating saturation to the soil surface was common and standing water was likely present, at least seasonally, in closed depressions on the upland. Mottled colors within agricultural fields in aerial photography in panel c (ISGS) reflect differences in soil moisture related to microtopography that persist despite artificial subsurface drainage.

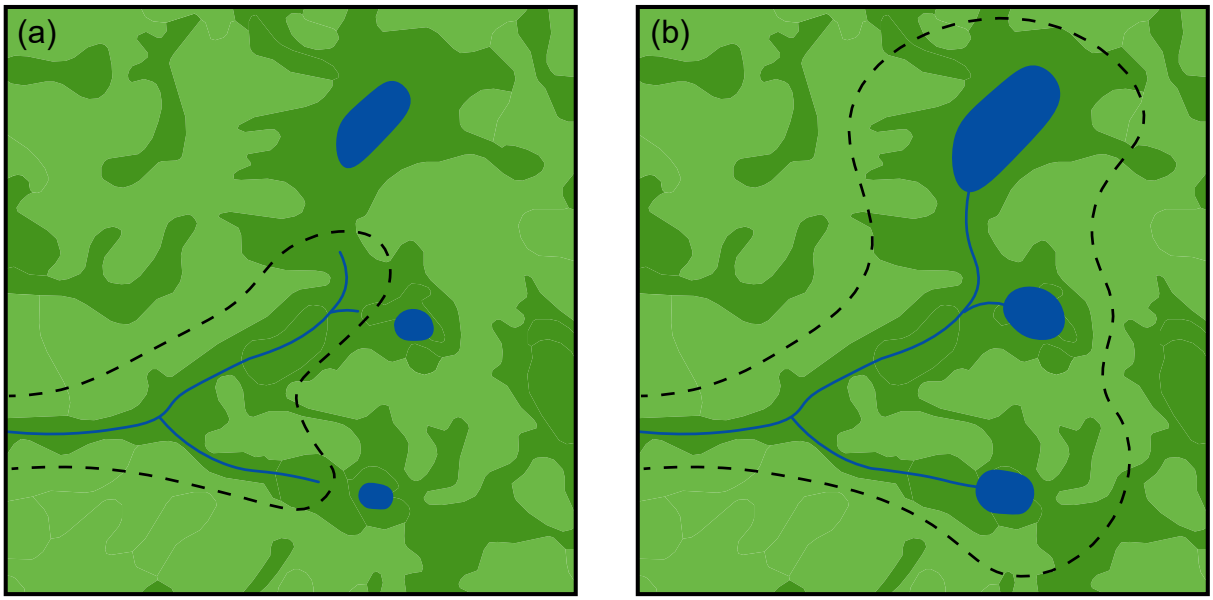

Figure 2.3 The disconnected drainage case is illustrated in panel a where a channel, shown as a blue line, receives water from the catchment defined by the black dashed line. Dark green areas are regions of poorly drained soil with light green areas better drained. Lakes formed in closed depressions remain isolated from the channel network until the channel head extends into their basins. In the connected case, shown in panel b, the drainage network receives water from a larger area, despite the fact that subtle topographic divides may separate closed depressions from the channel network. During spillover events, like that shown in panel b, lakes connect to the external drainage network effectively increasing the drainage area.

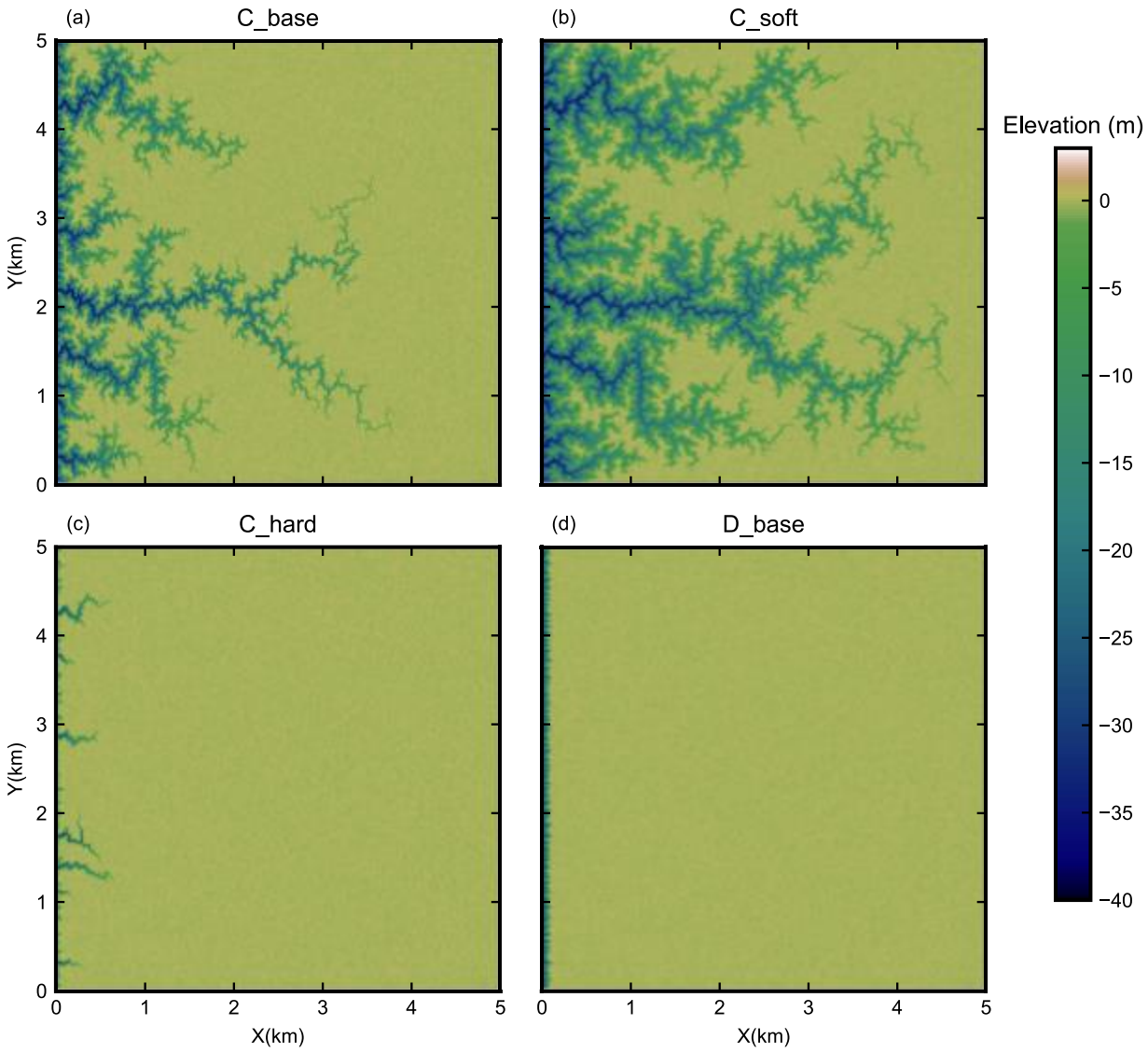

Figure 2.4 The modeled landscapes after 50000 years evolution, case parameters given in Table 2.1. (a), (b) and (c) are results of connected case with different fluvial erosion coefficient values. (d) is the result of the disconnected case. The diffusivity value is 0.001 in all four simulations.

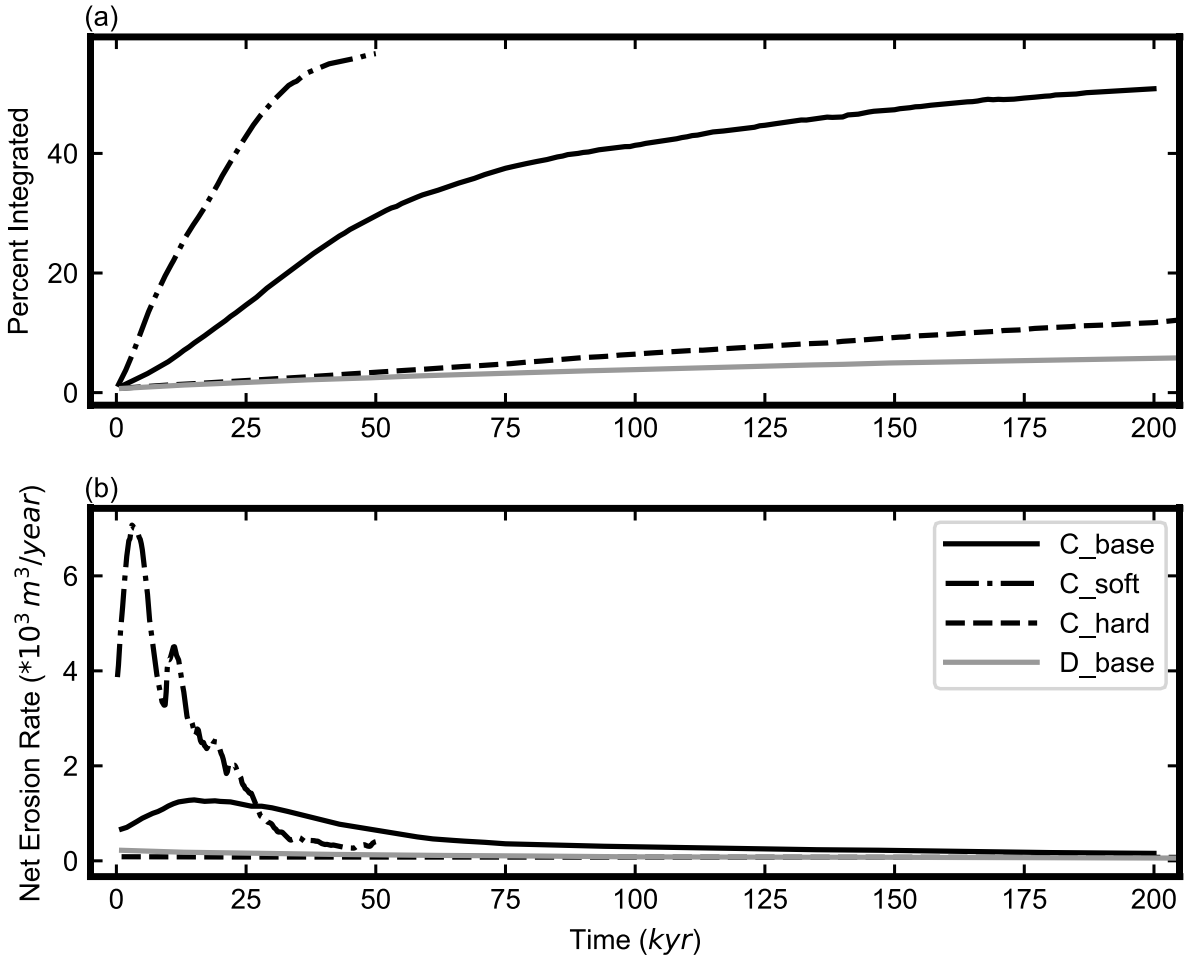

Figure 2.5 The evolution of percent integrated and net erosion rate over time. Black lines are results of connected cases with different fluvial erosion coefficient values, and the result of the disconnected case is shown as gray line. The diffusivity value is 0.001 in all four simulations. (a): the evolution of percent integrated. (b): the evolution of total mass loss rate.

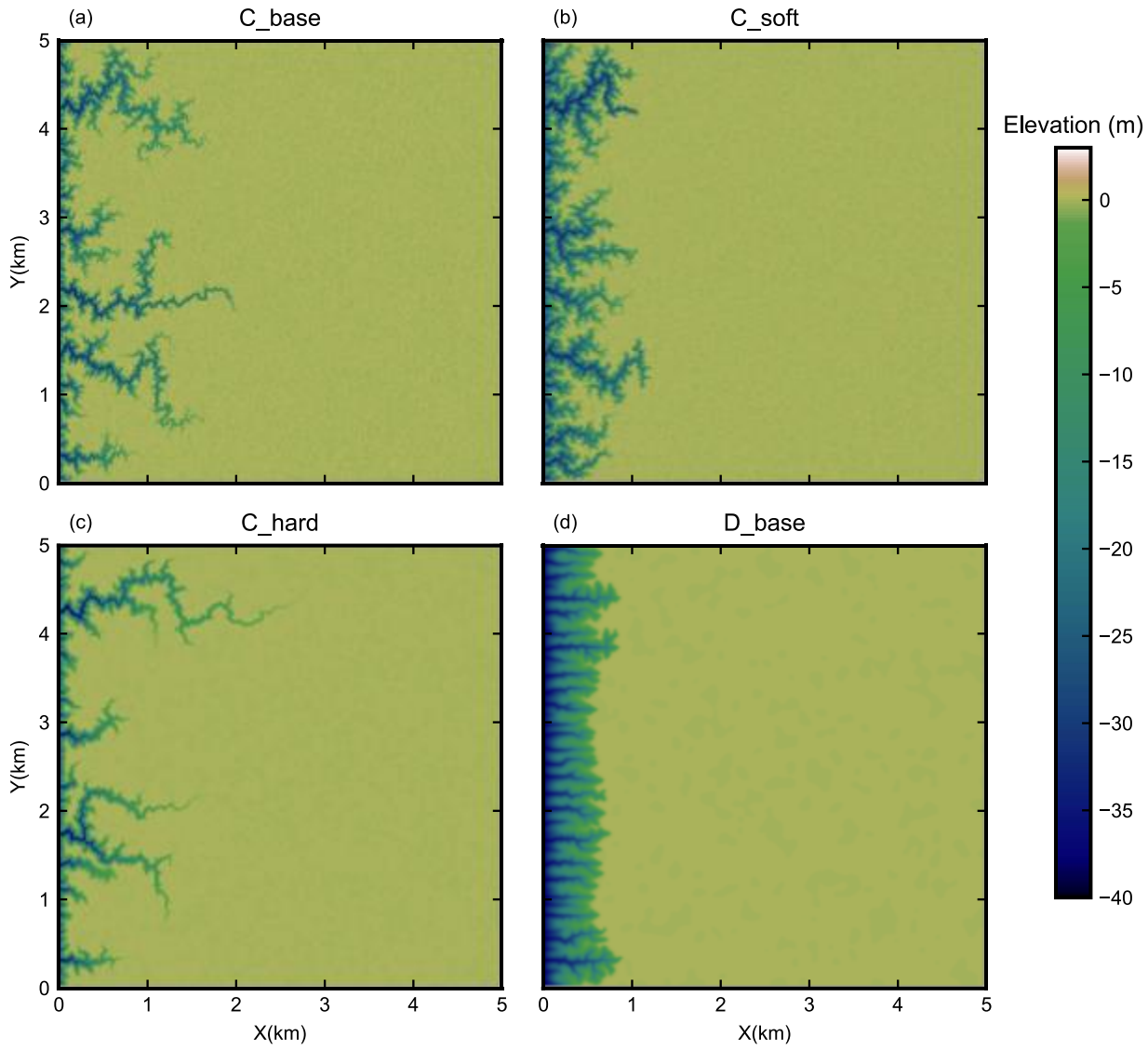

Figure 2.6 The modeled landscapes when 15% of the upland is integrated. (a), (b) and (c) are results of connected case with different fluvial erosion coefficient values. (d) is the result of the disconnected case. The diffusivity value is 0.001 in all four simulations.

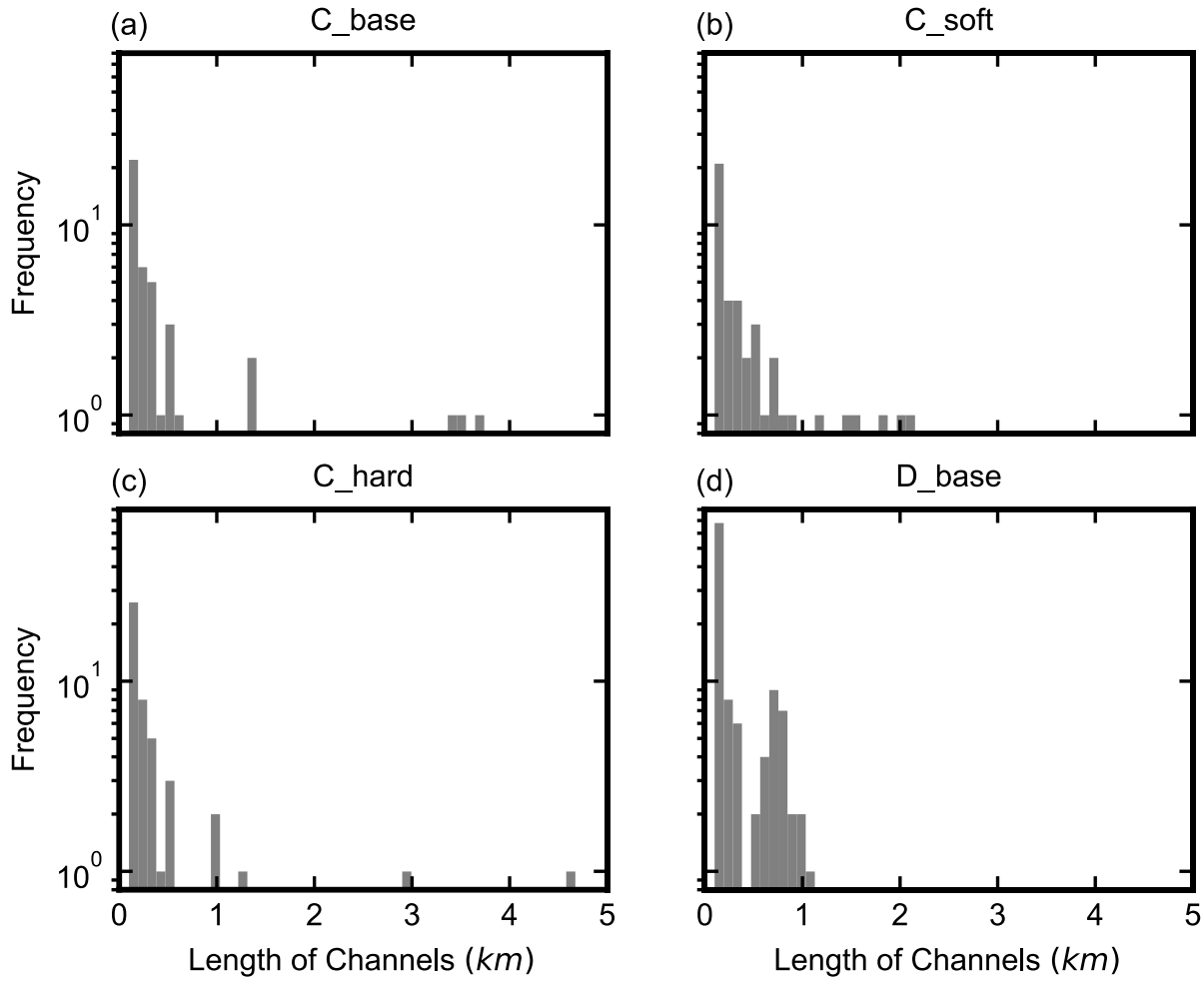

Figure 2.7 Histograms of channel lengths for channels above 100m in length when 15% of the upland is integrated. (a), (b) and (c) are results of connected case with different fluvial erosion coefficient values. (d) is the result of the disconnected case. The diffusivity value is 0.001 in all four simulations. Note that the vertical axis is in log scale.

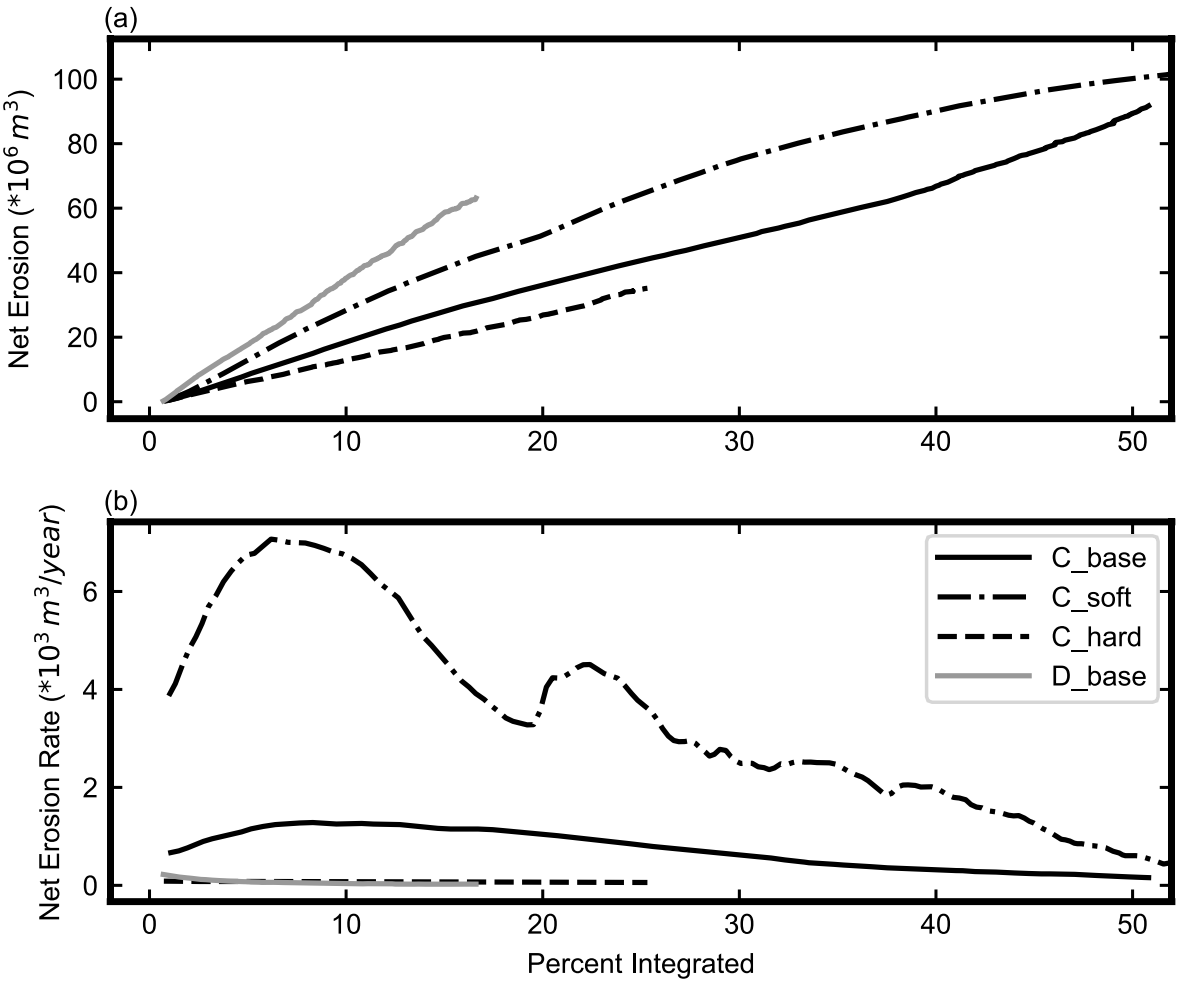

Figure 2.8 The evolution of net erosion (a) and its rate (b) as a function of percent integrated. Black lines are results of connected cases with different fluvial erosion coefficient values, and the result of the disconnected case is shown as gray line. The diffusivity value is 0.001 in all four simulations.

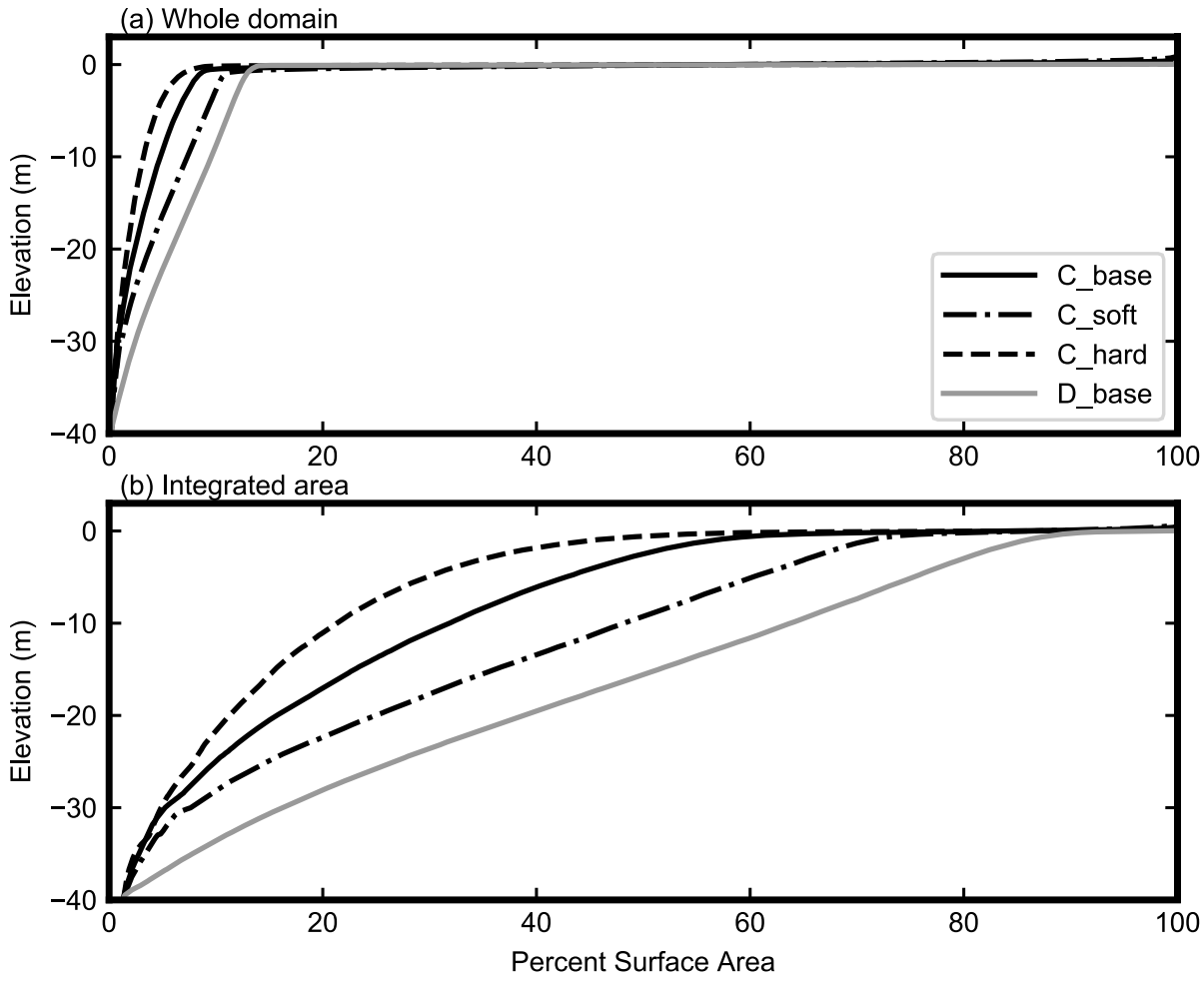

Figure 2.9 The hypsometric curves of the whole domain (a) and only the integrated area (b) when 15% of the upland becomes integrated. Black lines are results of connected cases with different fluvial erosion coefficient values, and the result of the disconnected case is shown as gray line.

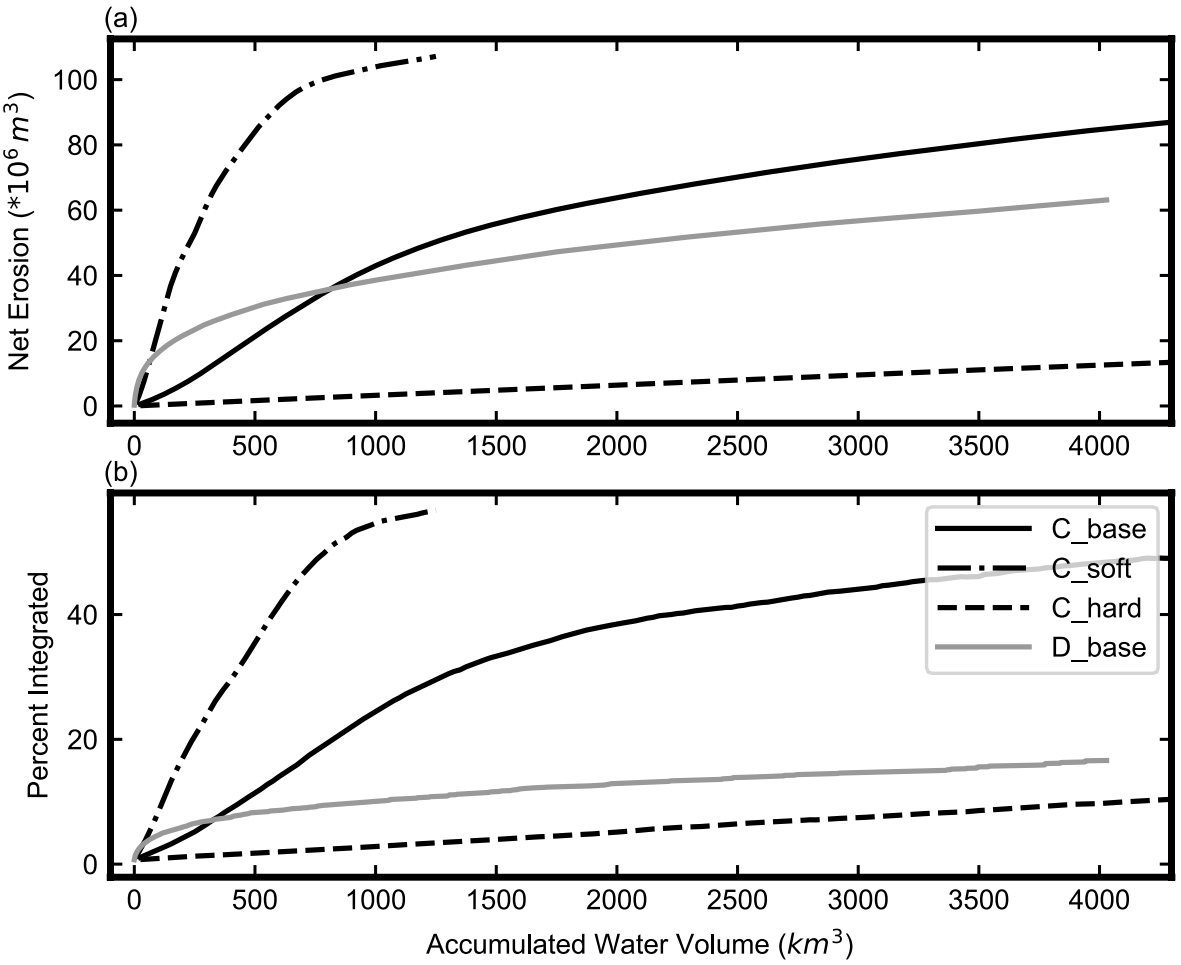

Figure 2.10 The evolution of net erosion (a) and percent integrated (b) as a function of accumulated water volume. The precipitation rate is assumed to be 1 m/year. Black lines are results of connected cases with different fluvial erosion coefficient values, and the result of the disconnected case is shown as gray line.

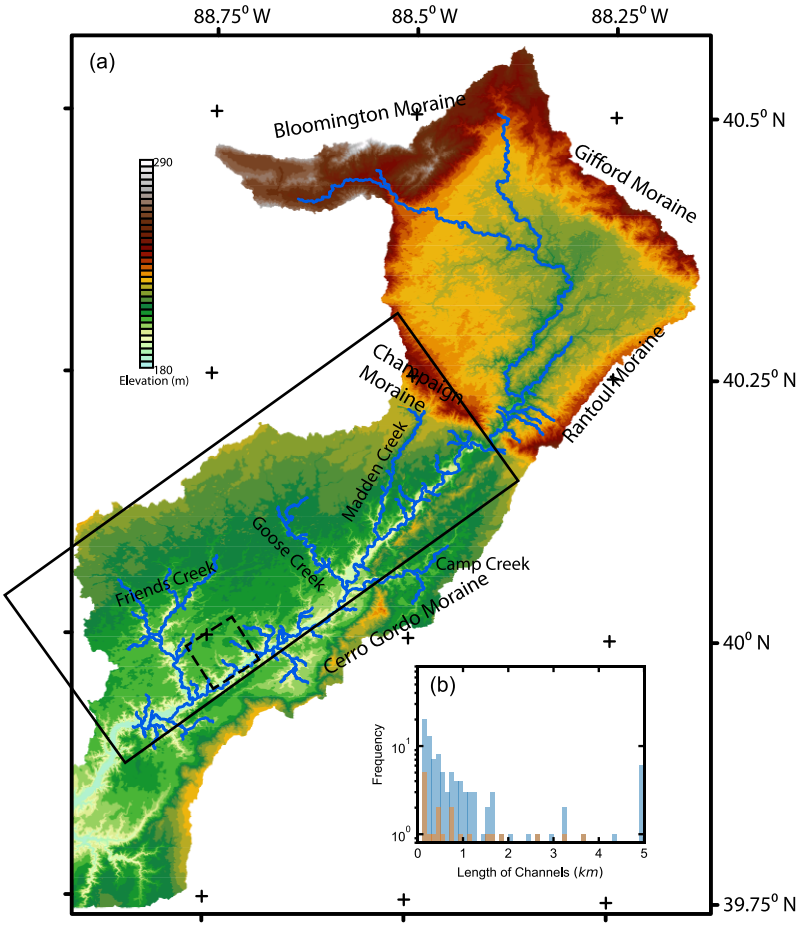

Figure 2.11 Digital elevation map of the Upper Sangamon River basin in east-central Illinois (a). The pre-settlement channel network as estimated by Rhoads et al. (2016) is shown as the blue lines. In the area defined by the black rectangle we measure the lengths of channels extending from the north-east side of the Sangamon Valley and show the distribution of these lengths as blue color in the inset histogram (b) which can be compared to Fig. 2.7. The area shown in Fig. 2.2 is indicated by the dashed-line box and the distribution of channel lengths in this area is shown as light orange color in the histogram (b).

Table 2.1 Description of numerical experiments. The value of D is 0.001 in all experiments.

Experiment	Drainage regime	K
C_base	Connected	0.0001
C_soft	Connected	0.001
C_hard	Connected	0.00001
D_base	Disconnected	0.0001

CHAPTER 3: TECTONIC CONTROLS ON RATES AND SPATIAL PATTERNS OF GLACIAL EROSION THROUGH GEOTHERMAL HEAT FLUX

Abstract[2]

Glacial erosion has shaped many mountain belts during the cold periods of the Late Cenozoic. The rate of glacial erosion is sensitive to the subglacial environment, including both the subglacial hydrology and the basal thermal regime. Geothermal heat from underlying bedrock is a major contributor to glacier energy budgets, controlling ice dynamics at the ice-bed interface by changing the basal temperature and the supply of meltwater. Despite the known influence of geothermal heat on the subglacial environment, its impact on glacial erosion has received little study. The geothermal heat flux in glaciated mountain ranges varies widely as a function of the tectonic setting. Therefore, if glacial erosion is sensitive to geothermal heat flux, the evolution of glaciated landscapes may depend upon tectonically-controlled geothermal gradients. We explore the impact of geothermal heat flux on the rates and spatial patterns of glacial erosion in mountain ranges using numerical models. We couple a sliding-dependent glacial erosion model with the Parallel Ice Sheet Model (PISM) to simulate the evolution of a synthetic glacial landscape. We find a robust tendency for increasing glacial erosion with increasing geothermal heat flux. The spatial pattern of erosion also varies with the magnitude of geothermal heat flux. At low geothermal heat flux, glacial erosion is consistently focused in major valleys. As geothermal heat flux increases, the area of significant glacial erosion expands into higher elevations and the rate of erosion increases. The location of maximum erosion migrates up-valley as geothermal heat flux increases, suggesting that glacial erosion tends to produce distinct landscapes as a function of geothermal heat flux. Our finding suggests that active mountain belts with high geothermal heat flux will express the glacial buzzsaw effect, in which high elevation topography is preferentially removed by glacial erosion. Glaciers at passive margins with low geothermal heat flux, in contrast, will tend to incise deep valleys at relatively

[2] This chapter is published as Lai, J. and Anders, A. M.: Tectonic controls on rates and spatial patterns of glacial erosion through geothermal heat flux, Earth and Planetary Science Letters, 543, 116348, doi:10.1016/j.epsl.2020.116348, 2020.

low elevations. Previous work on the interaction between tectonics and landscape evolution has focused on relief generation and fracturing of rocks. Our results introduce a novel potential linkage between tectonics and erosion based on the sensitivity of glacial erosion to geothermal heat.

Keywords

Landscape evolution, glacial erosion, numerical modeling, geothermal heat

3.1 Introduction

Glacial erosion has shaped the majority of high mountain ranges on Earth including both mountains at active convergent boundaries, such as the Andes, and those formed on passive continental margins, such as the Scandinavian Mountains. Tectonics have a clear impact on the landscapes of these glaciated mountains through relief generation and fracturing of rocks. The thermal effects of tectonic activity could also be an important control on glacial landscapes by providing additional heat for the glacier system. Tectonic activity tends to increase geothermal heat flow such that the geothermal heat flux in tectonically active regions can reach values up to five times greater than the typical continental background value of 44 mW/m^2 (Davies, 2013; Hamza et al., 2005; Sclater et al., 1980). The geothermal heat flux in currently glaciated mountains varies widely from 30 mW/m^2 in passive continental margins to over 150 mW/m^2 in active subduction zones (Table 3.1; Davies, 2013; Goutorbe et al., 2011). Geothermal heat is a major heat source to glaciers. High geothermal heat flow increases the temperature at the base of glaciers and promotes basal meltwater production. Observations from Iceland (Magnússon et al., 2007), Central Greenland (Fahnestock et al., 2001), and the West Antarctic ice sheet (Schroeder et al., 2014) suggest that elevated geothermal heat flow strongly affects the temperature and water content at the base of glaciers, resulting in fast ice streams. Despite the known influence of geothermal heat on the subglacial environment and its wide spatial variation in glaciated regions, the potential impact of geothermal heat on glacial erosion has not been well studied.

The basal thermal regime of glaciers is a first-order control on patterns of glacial erosion. Cold-based ice that is frozen to the bed causes negligible erosion due to extremely slow sliding and limited ice-bed separation (Kleman and Stroeven, 1997; Thomson et al., 2010). Glacial

landscape evolution models usually assume that glacial erosion occurs exclusively under warm-based ice where the ice is at the pressure melting point (e.g., Tomkin and Braun, 2002). Dissected plateaus on glaciated continental margins with deeply incised fjords and low-relief plateaus have been attributed to selective erosion by polythermal ice sheets in Fennoscandia (Kleman and Stroeven, 1997) and Canada (Staiger et al., 2005). In those regions, warm-based ice streams carved deep fjords while cold-based ice patches preserved upland topography. Numerical modeling studies of mountain glaciers eroding actively uplifting mountains suggest that cold-based ice can exist at high elevations and protect the peaks from erosion (Tomkin and Braun, 2002; Yanites and Ehlers, 2012).

Under warm-based ice, geothermal heat flow could also control glacial erosion because rates of glacial abrasion and quarrying are both sensitive to subglacial hydrology. Models of glacial erosion usually link the rate of erosion to the effective pressure (the difference between ice overburden pressure and subglacial water pressure) at the bed. Theoretical models for abrasion identify basal sliding velocity as the primary control on abrasion (Hallet, 1979). Low effective pressure accelerates basal sliding (Iken, 1981) and, therefore, increases abrasion. Models for quarrying suggest that the rate of quarrying depends on the effective pressure directly (Hallet, 1996; Iverson, 2012). High geothermal heat flow from the bedrock has the potential to increase the amount of meltwater in the subglacial environment and consequently control the rates of both glacial abrasion and quarrying.

Based on our understanding of the dominant processes of glacial erosion and the influence of geothermal heat on ice dynamics, we predict that increased geothermal heat flux will enhance glacial erosion by accelerating basal sliding and expanding the area of warm-based ice, changing both rates and spatial patterns of erosion. To test this prediction, we build a landscape evolution model using a thermodynamically coupled ice sheet model and a sliding-based glacial erosion rule and examine the rates and patterns of glacial erosion across a range of geothermal heat fluxes.

3.2 Model description

We build a glacial landscape evolution model using the Parallel Ice Sheet Model (PISM, stable version 1.0; the PISM authors, 2015) to simulate the temperature and movement of

glaciers. We couple PISM with a glacial erosion rule to model the evolution of topography due to glacial erosion.

3.2.1 Ice flow model - Parallel Ice Sheet Model

PISM is an open-source, parallel, thermodynamically coupled ice sheet model. Given bedrock topography, geothermal heat flux, and climate forcing, PISM computes the evolution of the thermal and dynamic states of the glacier over time. PISM has effectively approximated the complex ice dynamics over mountainous regions (e.g., Golledge et al., 2012; Seguinot et al., 2018; Ziemen et al., 2016).

Ice flow in PISM is governed by the Glen-Nye flow law, and ice softness is controlled by ice temperature, pressure, and water content through an enthalpy-based scheme (Aschwanden et al., 2012). PISM uses a hybrid stress balance scheme that combines the Shallow Ice Approximation (SIA; Hutter, 1983) for internal deformation and the Shallow Shelf Approximation (SSA; Morland, 1987) for membrane stress (also known as longitudinal stress). The membrane stress represents the longitudinal stretching within the ice and in alpine glaciers it is an important component in balancing the driving stress (Hindmarsh, 2006; Bueler and Brown, 2009). The basal sliding velocity is determined by the balance of membrane stress, driving stress, and basal shear stress. The basal shear stress is related to the sliding velocity through a Weertman-style sliding rule:

$$\boldsymbol{u}_s = \frac{C_s}{N} |\boldsymbol{\tau}_b|^{m-1} \boldsymbol{\tau}_b, \tag{3.1}$$

where $\boldsymbol{u}_s$ is the sliding velocity, C_s is a sliding coefficient, N is effective water pressure, and $\boldsymbol{\tau}_b$ is basal shear stress. The effective water pressure is assumed to be a function of the ice overburden pressure and the modeled amount of subglacial water, based on laboratory experiments with till from the base of Ice Stream B in West Antarctica (Bueler and van Pelt, 2015; Tulaczyk et al., 2000):

$$N = \min\left\{P_0, N_0 \left(\frac{\delta P_0}{N_0}\right)^{\frac{W}{W_0}} 10^{\frac{e_0}{C_c}\left(1-\frac{W}{W_0}\right)}\right\}. \tag{3.2}$$

Here P_0 is the ice overburden pressure, which is determined by the ice thickness and density, N_0 is a reference effective pressure, δ is the lower limit of the effective pressure, expressed as a fraction of the ice overburden pressure, e_0 is the void ratio at the reference effective pressure, C_c

is the compressibility coefficient of the till, W is the effective thickness of subglacial water, and W_0 is the upper limit of W. The amount of subglacial water is modeled by a non-conservative hydrology model. Any meltwater generated at the base is stored in place and is removed at a fixed rate:

$$\frac{\partial W}{\partial t} = \frac{S}{\rho_w} - C_w, \tag{3.3}$$

where S is the basal melting rate, ρ_w is the density of water, and C_w is the fixed decay rate that removes the water. W is limited at least zero and at most 2 meters. Using these simple models of basal motion and subglacial hydrology, PISM has successfully captured the complex flow patterns of Greenland outlet glaciers (Aschwanden et al., 2016).

At the base of the ice, conserving energy across the ice-bedrock interface determines the rate of basal melting. PISM solves the conservation of energy using an enthalpy-based scheme (Aschwanden et al., 2012) that accounts for the latent heat of liquid water in temperate ice. The basal melt rate is a linear function of the geothermal heat flux from the bedrock, frictional heating and the diffusive and advective heat flux with the ice. Water drained within the ice is also added to basal melting. For a detailed description of the thermodynamic model, we refer the readers to Aschwanden et al. (2012).

3.2.2 Glacial erosion model

We employ a simple, widely-used erosion model (e.g., Braun et al., 1999; Egholm et al., 2009; Herman and Braun, 2008; MacGregor et al., 2000; Tomkin, 2003). The rate of glacial erosion E_g is assumed to be proportional to the sliding velocity raised to a power:

$$E_g = K_g |\boldsymbol{u}_s|^l, \tag{3.4}$$

where K_g is an erodibility coefficient and l is a constant. This erosion model is a reasonable approximation when abrasion dominates glacial erosion (Hallet, 1979), and it also reproduces the qualitative patterns of glacial quarrying in numerical glacial erosion models (Hallet, 1996; Iverson, 2012; Ugelvig et al., 2016). Available field measurements suggest that l is 1 or 2 and K_g varies from 10^{-4} to 10^{-7}, depending on the choice of l (Herman et al., 2015; Humphrey and Raymond, 1994; Koppes et al., 2015). In this study, we assume that l is 1 and K_g is 5×10^{-5}. In our modified version of PISM (available at https://github.com/laijingtao/pism/tree/jlai-EPSL-2020), the bedrock topography is updated at each time step according to Eq. 3.4.

3.2.3 Bedrock topography

We create a synthetic fluvial landscape using the Landlab model platform (Hobley et al., 2017). The fluvial landscape is a 100-km by 100-km mountain belt with a relief of 2500 m (Fig. 3.1). Each side of the ridge has 5 major valleys. This bedrock topography represents a mountain landscape before glaciation. The grid resolution is 1 km and it is a reasonable value for PISM to capture the flow pattern of large valley glaciers (Aschwanden et al., 2016). A topography with a spatial resolution of 250 m is also used to test the influence of grid resolution on model results.

3.2.4 Climate forcing

Climate is represented by the mean annual temperature and annual precipitation rate in our model. The mean annual temperature decreases as the elevation rises with a lapse rate of 6.5 °C km^{-1}. The seasonal variation in temperature is modeled by a fixed sinusoidal function with the summer maximum temperature assumed to be 5 °C higher than the mean annual temperature. The precipitation rate is uniform across the model domain, and there is no seasonal variation in precipitation.

Ice surface mass balance is computed from the near-surface air temperature and precipitation. The rate of accumulation is equal to the precipitation rate when air temperatures are below 0 °C and decreases to 0 linearly as temperatures rise from 0 to 2 °C. Ablation is computed using the Positive Degree Day (PDD) model, in which the rate of ablation is approximated as a function of the number of positive degree days in a year (Calov and Greve, 2005).

3.2.5 Experiment design

We consider two climate scenarios in our experiments: a constant climate and a glacial-interglacial cycle. In the constant climate, both the mean annual temperature at the lowest elevation and the precipitation rate are fixed. In the glacial-interglacial cycle, we assume an asymmetrical 100,000-year cycle. The mean annual temperature at the lowest elevation decreases linearly for 80,000 years and then increases linearly over 20,000 years. The precipitation rate changes as a function of the mean annual temperature, increasing by 7.2% for every one degree Celsius of air temperature increase (Huybrechts, 2002).

We conduct four groups of experiments (Table 3.3). In each set of experiments, we use a range of values for the geothermal heat flux from 20 mW/m^2 to 200 mW/m^2 to represent the possible range of heat flux in glaciated mountains (Table 3.1). In Ex. 1 and 2, we use a specific constant climate to demonstrate the impact of geothermal heat flux on glacial erosion. In Ex. 1, we model the glaciation in a constant climate without glacial erosion. The mean annual temperature at sea level is 2 °C and the mean annual precipitation is 400 mm/year. The simulations start from an ice-free topography and end when the ice flow reaches a steady state. In Ex. 2, we model the glacial erosion in a constant climate for 20,000 years. The climatic conditions in Ex. 2 are the same as Ex. 1 and the results from Ex. 1 are used as initial states for Ex. 2. In Ex. 3a-c, we model the glacial erosion over a glacial-interglacial cycle, starting from an ice-free topography. In Ex. 3a, the temperature drops 8 °C from interglacial to glacial. At the glacial maximum, the mean annual temperature at sea-level and mean annual precipitation are also 2 °C and 400 mm/year, respectively, which are the same as Ex. 1 and 2. In Ex. 3b and 3c, we use Ex. 3a as a base case and change the climatic conditions to investigate whether the impact of geothermal heat flux is observable in a wide range of climate settings. In Ex. 3b, the glacial to interglacial temperature difference varies from 4 to 12 degrees, while the climate at the glacial maximum is the same as the climate at the glacial maximum in Ex. 3a. In Ex 3c, similarly, we change the mean annual temperature and mean annual precipitation at the glacial maximum, while glacial to interglacial temperature difference remains fixed at 8 °C, which is the same value used in Ex. 3a. In Ex. 4, we explore the model sensitivity to the meltwater decay rate in the subglacial hydrology model using the constant climate forcing of Ex. 2.

3.3 Model results

3.3.1 Constant climate without erosion

In Ex. 1, we model glaciation in a constant climate without erosion. The resulting glaciers differ in both thickness and extent as a function of geothermal heat flux. In general, glaciers are smaller and thinner as the geothermal heat flux increases. In the case with a geothermal heat flux of 40 mW/m^2, which is a typical value of continental interiors, glaciers in major valleys are over 800 m thick (Fig. 3.2a). In contrast, when the geothermal heat flux is 160 mW/m^2, valley glaciers are less than 600 m thick and they are 5-10 km shorter than the glaciers in the case with 40

mW/m^2 geothermal heat (Fig. 3.2b). We quantify the change in glacier size by calculating the total volume of ice. As the geothermal heat flux increases, ice volume decreases linearly (Fig. 3.3a). The total volume of ice in the case with 20 mW/m^2 geothermal heat flux is twice as large as in the case with a heat flux of 200 mW/m^2.

More basal meltwater is produced in the high geothermal heat flux cases than in the low geothermal heat flux cases. Most of the basal meltwater is generated in major valleys where the melting point of ice is lowered by the pressure of thick ice (Fig. 3.2c and 3.2d). The basal meltwater production rate increases from less than 10 mm/year to 40 mm/year in major valleys, as the geothermal heat flux increases from 40 to 160 mW/m^2 (Fig. 3.2c and 3.2d). The extent of basal melting varies with geothermal heat flux; basal melting is limited to lower parts of major valleys when the geothermal heat flux is low (Fig. 3.2c), while in the case with higher geothermal heat flux, basal melting occurs in a broader area, expanding to higher elevations (Fig. 3.2d).

The spatial patterns of basal meltwater production control the patterns of basal effective pressure and, therefore, the patterns of sliding. Both sliding and low effective pressure occur in major valleys (Fig. 3.2e-h). In the case with low geothermal heat flux, low effective pressure is limited to narrow belts near the center of valleys (Fig. 3.2e). In contrast, when the geothermal heat flux is 160 mW/m^2, the zone of low effective pressure expands to higher elevations (Fig. 3.2f). Glacier sliding generally requires low effective pressure, thus, the spatial patterns of sliding are similar to the patterns of effective pressure. When the geothermal heat flux is low, basal sliding is limited to lower parts of major valleys (Fig. 3.2g), and as the geothermal heat increases, the sliding occurs higher in the landscape (Fig. 3.2h). Furthermore, the rates of sliding are also controlled by geothermal heat flux. Glaciers in the case with low geothermal heat flux slide only ~25 m per year (Fig. 3.2g), while glaciers with higher geothermal input can slide over 100 m per year (Fig. 3.2h).

To evaluate the importance of grid resolution we compare the results of this group of experiments to experiments run on a higher-resolution bedrock topography with a grid size of 250m. Although glacier size differs slightly as a function of grid resolution, the impact of geothermal heat flux is still robust. The rates and spatial footprint of glacial erosion increase as geothermal heat flux increases.

3.3.2 Constant climate with erosion

In Ex. 2, we simulate glacial erosion in a constant climate for 20,000 years. Rates and patterns of erosion are influenced by geothermal heat. The total glacial erosion is generally less than 50 m in major valleys when the geothermal heat flux is 40 mW/m^2 (Fig. 3.4a), while in the case with high geothermal heat flux, the total erosion in valleys is over 200 m in some valleys (Fig. 3.4d). The spatial patterns of glacial erosion are similar to patterns of sliding. Most of the erosion occurs in major valleys (Fig. 3.4). When the geothermal heat flux is low, glacial erosion only occurs in lower parts of the valley, while upper parts of the landscape remain unchanged (Fig. 3.4a). As the geothermal heat flux increases, glacial erosion expands into upper parts of the landscape (Fig. 3.4b and 3.4c), and most of the valley network is influenced by glacial erosion when the geothermal heat flux is high (Fig. 3.4d). Although the total ice volume decreases as the geothermal heat flux increases, the total erosion volume increases by a factor of 10 when the geothermal heat flux increases from 20 mW/m^2 to 200 mW/m^2 (triangles in Fig. 3.3b).

3.3.3 Glacial-interglacial cycle

In Ex. 3a, we model the glacial erosion over a glacial-interglacial cycle. Similar to the cases with constant climate, glacial erosion is focused in major valleys in these experiments (Fig. 3.5). However, in these cyclic climates, the ridge tops are also influenced by glacial erosion (Fig. 3.5) because they are perennially covered by ice. The impact of geothermal heat flux is similar to that observed under constant climates. Higher values of geothermal heat flux result in more total erosion in a glacial-interglacial cycle and glacial erosion expands into higher elevations as the geothermal heat flux increases (Fig 3.5). The total volume of erosion increases by a factor of 5 as the geothermal heat flux increases from 20 mW/m^2 to 200 mW/m^2 (square dots in Fig. 3.3b).

The impact of geothermal heat flux on erosion is apparent in valley long profiles. When the geothermal heat flux is 40 mW/m^2, most of the erosion occurs in lower parts of the valley whereas areas with elevation >1000 m remain unchanged (Fig. 3.6a). As geothermal heat flux increases, erosion gradually expands into upper parts of the valley and the amount of erosion increases (Fig. 3.6). When the geothermal heat flux is 160 mW/m^2, most of the glaciated part of the valley is modified by glacial erosion (Fig. 3.6d). The location of the maximum erosion also migrates upward as the geothermal heat flux increases (Fig. 3.6). Maximum erosion occurs low in major valleys when the geothermal heat flux is low (Fig. 3.6a). In contrast, when the

geothermal heat flux is high, the greatest erosion occurs toward the upper end of the valleys (Fig. 3.6d).

In Ex. 3b, we conduct a group of experiments with different glacial to interglacial temperature changes. The climate at the glacial maximum remains fixed and the interglacial climates are changed such that the temperature difference between glacial and interglacial periods varies from 4 to 12 °C. In all simulations, model results show a trend of increased erosion with increasing geothermal heat flow (Fig. 3.7a). The total amount of erosion is influenced by the glacial/interglacial temperature difference significantly. In a cycle with a small temperature change, the climate is generally colder and yields more erosion than a cycle with a large temperature change (Fig. 3.7a). Despite the variations in the total amount of erosion between different cases, the impact of increasing geothermal heat flow on glacial erosion is robust across all simulations. We quantify the change of glacial erosion as a result of increased geothermal heat flow by calculating the ratio of the amount of erosion between the case with 160 mW/m^2 heat flow and the case with 40 mW/m^2 heat flow. Increasing the geothermal heat flux from 40 mW/m^2 to 160 mW/m^2 results in an increase of glacial erosion by a factor of 4 to 5 in all cases (Fig. 3.7b).

In Ex. 3c, we keep exploring the influence of geothermal heat flow on glacial erosion in a wide range of climate by changing the climatic conditions at the glacial maximum. The mean annual temperature at sea level at the glacial maximum ranges from 0 to 4 °C and the mean annual precipitation ranges from 200 to 800 mm/year. The glacial/interglacial temperature difference remains constant at 8 °C across different cases. Changes in climatic conditions lead to different equilibrium line altitudes (ELAs) and changes in of glacier extent, which logically will greatly impact glacial erosion. We avoid comparing simulations with very different glacier extents in order to focus on the potential impacts of geothermal heat flux. We accomplish this by changing temperature and precipitation simultaneously to create a set of cases with similar ELA and ice cover but different climates. In all climate conditions, the total volume of eroded material increases as the geothermal heat flux increases (Fig 3.7c). In a warm and wet climate, the amount of erosion is generally higher than the case with a cold and dry climate. Although the amount of glacial erosion is significantly controlled by the climatic conditions at the glacial maximum, increasing the geothermal heat flow from 40 mW/m^2 to 160 mW/m^2 consistently increases the eroded volume by a factor 3 to 5 (Fig. 3.7d).

3.4 Discussion

3.4.1 Model limitation - Importance of subglacial hydrology

Our model uses a highly idealized model for subglacial hydrology. We assume all the meltwater is stored locally with a limit of water thickness, and the water is removed at a constant rate. This simple hydrology model reduces the computational cost significantly and allows for long-term experiments. More realistic models of the subglacial hydrologic system are much more complicated and our ability to constrain the parameters controlling the formation and evolution of subglacial drainage networks is extremely limited by a lack of data and difficulty of observation of the subglacial environment. The dynamism of the subglacial environment may make it unreasonable to model detailed subglacial hydrologic processes over geomorphically relevant timescales. We identify two specific limitations of our hydrology model which may limit its predictive power for glacial erosion: surface meltwater inputs to the glacier bed and evolution of the basal drainage network.

Meltwater from the surface provides the largest source of subglacial water in many glaciers. Input from surface melt may diminish the impact of geothermal heat flux because annual surface melt is typically 1 or 2 orders of magnitude larger than annual basal melt caused by geothermal heat flux and frictional heat. However, the impact of the surface melt is mostly limited to the lower parts of glaciers because the melting rate is highest in the ablation zone. Surface water in the accumulation zone seldom reaches the bed because it refreezes during englacial transport. In our simulations, the subglacial water thickness in the ablation zone is already at its maximum, resulting in very low effective pressures and fast sliding rates. Adding more water in the ablation zone will not change the patterns of sliding and erosion. Therefore, we suggest that our simple hydrology model still successfully captures the first-order sliding patterns.

The second limitation of our model is the simplicity of the model of removal of water from the subglacial environment. Glaciologists often characterize subglacial hydrologic systems into two groups: slow, inefficient and distributed drainage versus fast, efficient and channelized drainage (Flowers, 2015). The hydrology model in our experiments uses a constant subglacial water decay rate to represent the efficiency of the subglacial drainage. In Ex. 4 we examine the sensitivity of our model to a range of meltwater decay rates. Although different values of meltwater decay rate have a significant impact on the rates and patterns of erosion, the tendency

for increased erosion with increasing geothermal heat flux is robust when the meltwater decay rate is lower than typical meltwater production rate (20-40 mm/year, see Fig. 3.2c and 3.2d). Increasing geothermal heat flux increases the rate of erosion and causes a broader area of erosion (Fig. 3.8), and the total volume of erosion is positively correlated to the value of geothermal heat flux (Fig. 3.9). When the meltwater decay rate is higher than typical meltwater production rate, the amount of erosion is limited and changing the value of geothermal heat flux has little impact on erosion (upside down triangles in Fig. 3.9). In these cases, the high meltwater decay rate can remove water from the subglacial hydrology system efficiently, and therefore, the effective pressure remains high. The sliding velocities and, therefore, the erosion rates are low as a result of high effective pressure. Even in major valleys, the high meltwater decay rate predicts very slow sliding and erosion rates throughout the glacier. In conclusion, glacial erosion rates and patterns are sensitive to geothermal heat flux in glaciers that are erosive, and the lack of sensitivity is limited to cases with very little erosion.

In summary, although the lack of data and difficulty of observation of the subglacial environment limit our ability to model the complex subglacial hydrology system accurately, the idealized subglacial hydrology model used in our study successfully captures the qualitative spatial patterns of glacial erosion and the tendency for increased erosion with increasing geothermal heat flux.

3.4.2 Comparison with actual glacial landscape

The distinct patterns of glacial erosion predicted by our numerical model suggest that glaciers will produce divergent landscapes in regions with different geothermal heat fluxes and similar climates. When the geothermal heat flux is high the fastest erosion occurs at high elevations near valley heads. This pattern of erosion will selectively remove area at high elevation. In contrast, when the geothermal heat flux is low most of the erosion occurs at low elevations toward the valley mouths, and mountain peaks are protected by non-sliding ice that is frozen to the bed. As a result, the valley profile tends to have a large area at high elevation. In this section, we select example basins from Iceland and Scandinavia that illustrate how these glacial landscapes are consistent with the tendencies suggested by our model.

Both Iceland and Scandinavia were extensively glaciated during the Last Glacial Maximum, and their landscapes are dominated by glacial erosional features such as U-shaped

valleys and deep fjords. The geothermal heat flow in Iceland is high due to the magmatism and volcanism in Mid-Atlantic Ridge. In contrast, the Scandes has a low geothermal heat flux. We plot the normalized valley long profile of an example basin in Iceland and an example basin in the Scandes. The valley long profile in Iceland has a typical concave shape with a gentle lower reach and a steep upper reach (Fig. 3.10a). In contrast, the valley long profile in the Scandes has a steeper lower reach than observed in Iceland, and the valley profile has a larger portion at high elevation than the valley in Iceland (Fig. 3.10a). This is suggestive of more efficient glacial erosion at high elevation in Iceland than in the Scandes, which is consistent with our model predictions.

We calculate the geophysical relief for the two basins. The geophysical relief is the difference between the real topography and a surface interpolated from basin boundaries. If we assume the ridges on the basin boundaries represent the original surface, the geophysical relief provides an estimation of the amount of erosion within the basin. Although we do not suggest that the basin boundaries in Iceland and the Scandes are remnants of paleo surfaces, we can still compare the geophysical relief patterns of the two basins to infer the differences in erosion patterns. Following the method of Brocklehurst and Whipple (2002), we first extract the elevations of the basin borders and fit an interpolate surface between the them. Next, we identify the outliers that are higher than the interpolated surface and repeat the interpolation with the interpolated surface also passing over these high outliers until all the basin is lower than the interpolated surface. The difference between the interpolated surface and the real topography is the geophysical relief. Brocklehurst and Whipple (2002) suggest that cubic interpolation is better than linear interpolation because it can produce a smooth surface, but we find that cubic interpolation results in unrealistically low elevations at some locations. A simple linear interpolation is, therefore, used in our calculation.

The two basins show distinct patterns of geophysical relief. In Iceland, the geophysical relief is high in mid- to upper parts of the valley, while in the Scandes, the geophysical relief is greatest in lower parts of the valley (Fig. 3.10b). The distinct patterns of relief suggest that the spatial patterns of glacial erosion are different in these two valleys. In Iceland, glacial erosion appears to be focused at high elevations, while in the Scandes, glacial erosion seems to be concentrated at low elevations.

The pattern in geophysical relief mirrors our modeled erosion pattern (Fig. 3.10c). We plot the normalized amount of erosion along a valley profile from a case with 40 mW/m^2 geothermal heat flux and a case with 120 mW/m^2. In order to compare the modeled results with real world data, we remove the low-elevation area beyond the modeled glaciers, noting that in both Iceland and the Scandes, the basins were completely covered by ice during glaciation. Modeled glacial erosion is concentrated in high elevations when the geothermal heat flux is high, while in low geothermal heat case, modeled erosion is focused in lower reaches.

The close correlation between the patterns of geophysical relief and our modeled erosion suggests that Iceland and the Scandes may represent examples of glacial landscapes controlled by geothermal heat. We have no specific constraint on the pre-glacial topography in these regions and cannot assert that the geophysical relief pattern is a precise estimate of glacial erosion. However, our preliminary analysis suggests that the imprint of geothermal heat in glacial landscapes may be observable and should receive further study.

3.4.3 The role of geothermal heat flux in different climatic settings

Glacial erosion is controlled by climate and the impact of climatic settings on erosion has been a focus of previous research (e.g., Yanites and Ehlers, 2012). Climate controls glacial erosion primarily by altering the basal thermal regime of glaciers (Thomson et al., 2010; Yanites and Ehlers, 2012). In this study, numerical modeling results show that changing geothermal heat flow could lead to a significant change in the basal thermal regime and consequently the rates and patterns of glacial erosion without any modification of climatic conditions. In Ex. 3, we investigate the impact of geothermal heat flow on glacial erosion in a wide range of climate, and the results indicate a tendency for increased erosion with increasing geothermal heat flow in all simulations. Furthermore, increasing geothermal heat flow from 40 mW/m^2 to 160 mW/m^2 consistently increases the total volume of erosion by a factor of 3-5 despite the climate varies in a wide range (Fig. 3.7). This finding suggests that geothermal heat flow may act as a control on glacial erosion that is independent of climate. However, increasing geothermal heat flow could lead to a reduction in glacier size (Fig. 3.3a), suggesting that high geothermal heat flux could eventually prevent the glacier from maintaining a size that is big enough to erode the landscape effectively. Especially in regions with warm climates, where the glacier size is already limited by the climate, increasing geothermal heat flux may eventually lead to a decrease in glacial erosion.

Geothermal heat flow controls glacial erosion through a way that is similar to climate, thus the impact of geothermal heat flow is comparable to the impact of climate. Increasing geothermal heat flow at the bed of a glacier is similar to increasing the atmospheric temperature from the surface in the context of modifying the basal thermal regime. Increasing geothermal heat flow and atmospheric temperature could both result in larger areas of warm-based ice, making their impact on glacial erosion not easily distinguishable. For instance, both warm climate and high geothermal heat flow will favor the glacial buzzsaw effect. We will discuss this topic in detail in the next section.

3.4.4 Implications for the glacial buzzsaw hypothesis

The glacial buzzsaw hypothesis suggests that glaciers can limit the height of mountains through intensive erosion at high elevations (Brozović et al., 1997; Egholm et al., 2009; Mitchell and Montgomery, 2006). The geomorphic evidence that supports this hypothesis is mainly from mid-latitude glaciated mountains, while in some high-latitude regions peaks attain high elevations. For example, mountain peaks in the southernmost of Patagonia Andes have high elevations well above the ELA and low glacial erosion efficiency (Thomson et al., 2010). A few mountains in the Alaska Range reach heights of over 4000 m, suggesting that the topography in this area is not limited by glacial erosion (Ward et al., 2012). These exceptions to the glacial buzzsaw model provide support for the idea that glaciers with frozen bases can protect mountain peaks from erosion (Thomson et al., 2010; Tomkin and Braun, 2002). Yanites and Ehlers (2012) show that only some climates generate high erosion rates at high elevations that are able to produce a glacial buzzsaw effect, and a cold climate leads to a large area of cold-based ice at high elevations. Our results show that the basal thermal state of ice at high elevations is sensitive to the geothermal heat flux. By increasing the geothermal heat flux alone, the ice at high elevations can change from cold-based to warm-based without changing the climatic conditions. The erosion at high elevation, therefore, is also sensitive to the geothermal heat flux. High geothermal heat flux will favor the glacial buzzsaw effect, in which high elevation topography is removed by glacial erosion. Low geothermal heat flux, in contrast, should tend to protect mountain peaks while incising deep valleys at relatively low elevations.

3.4.5 Implication for the interaction between tectonics and landscape evolution

Tectonic forcing is often considered a primary control on the landscape evolution in orogenic settings. Previous studies have mainly focused on landscape evolution in response to different rates and patterns of rock uplift (e.g., Tomkin, 2003) and fracture of rocks due to tectonic activities (e.g., Dühnforth et al., 2010). This research provides an alternative view of how tectonics influences surface processes through the sensitivity of glacial erosion to geothermal heat flux.

Geothermal heat flux is primarily controlled by tectonic processes. In subduction zones, volcanic arc and backarc regions usually have higher geothermal heat flow than the forearc. The subduction of cool oceanic crust leads to a cooling of the forearc, resulting in low surface heat flow. In the central Andes, for instance, the geothermal heat flux is as low as 20 mW/m^2 in the forearcs (Springer and Förster, 1998). Volcanic arcs are associated with high geothermal heat flux due to the rising of hot magma and efficient heat conduction caused by high temperatures in the mantle. High geothermal flux is not restricted to the arc but usually extends into the backarc as a result of thermal convection in the backarc mantle (Currie and Hyndman, 2006). In northern Cascadia subduction zone, geothermal heat flux is high in both arc and backarc regions. The value of heat flux in backarc is ~75 mW/m^2 and over 100 mW/m^2 in some area (Currie and Hyndman, 2006). When the subducting slab is flat, backarc regions have low geothermal heat flux due to limited mantle convection between the slab and the overriding plate (Currie and Hyndman, 2006). The subduction of the Nazca plate, for example, results in a relatively low geothermal heat flux of 50 mW/m^2 in Peru (Hamza et al., 2005).

High geothermal heat flux is also associated with continental rift systems. Beneath the West Antarctic Ice Sheet, measurements show that the geothermal heat flux is high and it is interpreted as a result of the crustal thinning and magmatism associated with West Antarctic Rift System (Schroeder et al., 2014).

In addition to tectonic processes, surface erosion itself may also influence geothermal heat flux. Exhumation causes the advection of rocks towards Earth's surface, resulting in a change in the vertical temperature gradient within the crust. Rapid erosion can increase the geothermal gradient and raise the geothermal heat flux (Braun, 2003). Modeled surface heat fluxes of the Olympic Mountains show an increased heat flux near the exhumed high topography (Batt et al., 2001). If we assume that an orogeny has reached an equilibrium between tectonic

uplift and erosion, resulting in a constant exhumation rate, and this equilibrium is maintained long enough to develop a thermal steady state, the geothermal heat flow will be

$$q = \frac{kET_L}{\kappa\left(1 - e^{-\frac{EL}{\kappa}}\right)}, \tag{3.5}$$

where k is the thermal conductivity, E is the exhumation rate, T_L is the temperature at some depth L in the Earth and κ is the thermal diffusivity (Braun et al., 2006). This simple model suggests that the geothermal heat flux is a non-linear function of the exhumation rate, but their relationship is close to a linear form. Our glacial erosion model suggests that the total erosion varies by an order of magnitude as the geothermal heat flux changes. Taken together, we suggest that a positive feedback between rapid glacial erosion and high geothermal heat flux is possible in orogenic belts.

3.5 Conclusion

The numerical experiments in this study explore the impact of geothermal heat fluxes on rates and patterns of glacial erosion. The predicted glacial erosion is found to strongly depend on the geothermal heat flux when the climatic conditions are the same. Increased geothermal heat flux leads to fast glacial erosion rates and expands the area of significant erosion up-valley to high elevations. When the geothermal heat flux is low, glacial erosion is slow and limited to low elevations within major valleys. In contrast, glacial erosion is fast and expands into upper parts of the topography when the geothermal heat flux is high. The location of the maximum erosion migrates from lower areas in the valleys to areas near valley heads as the geothermal heat flux increases, suggesting that the different geothermal heat flux values will lead to distinct glacially-eroded landscapes. The dependency of glacial erosion on geothermal heat suggests that tectonically induced change of geothermal heat flux may provide a potential linkage between tectonics and erosion.

3.6 Figures and tables

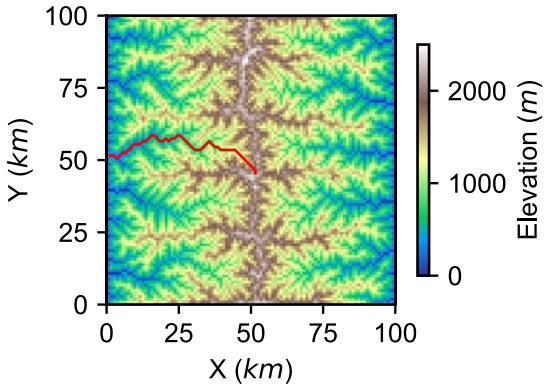

Figure 3.1 Initial bedrock topography. The red line is the valley profile shown in Figure 3.6.

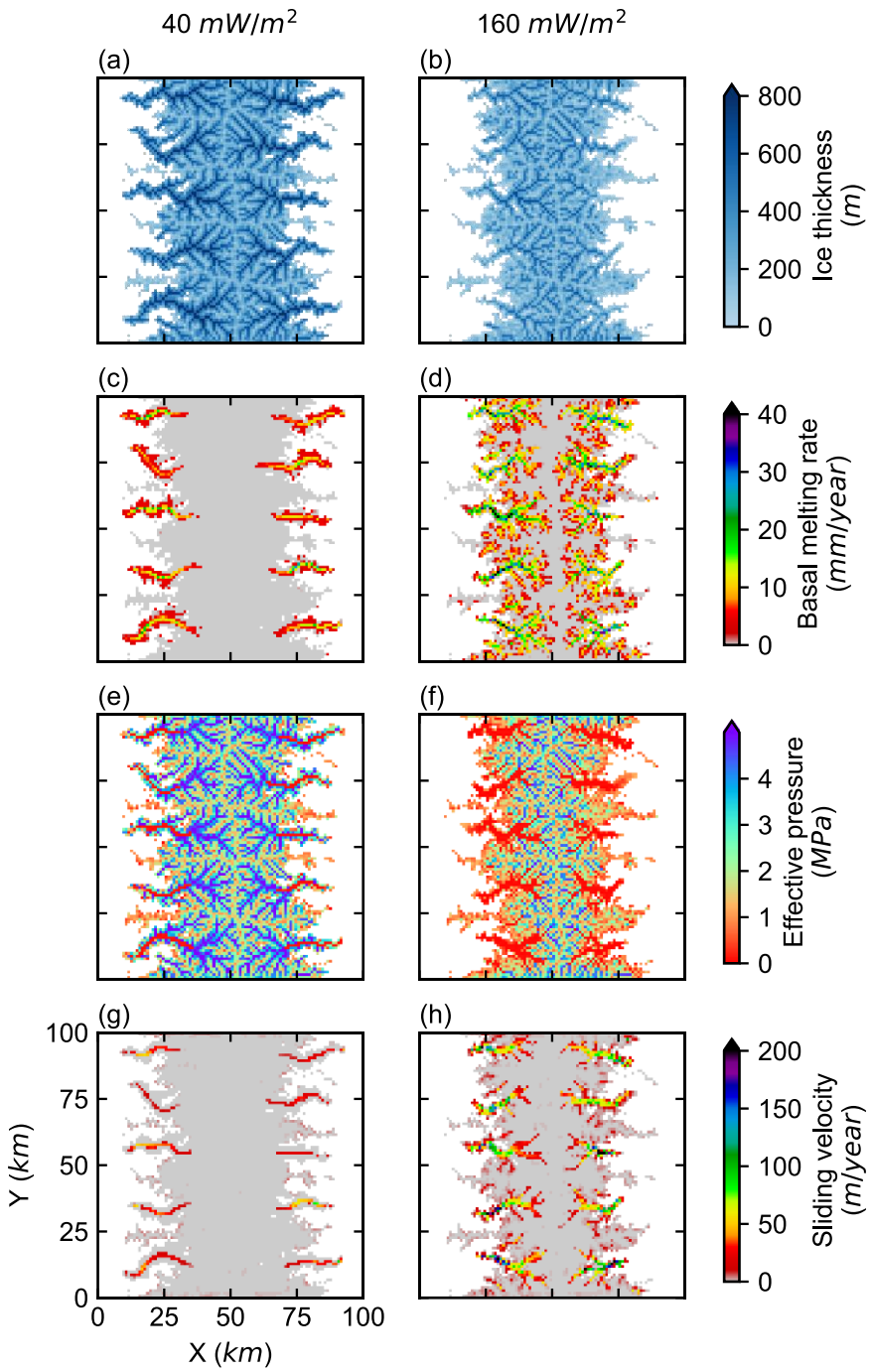

Figure 3.2 Ice thickness (a and b), basal meltwater production rate (c and d), effective pressure (e and f) and basal sliding velocity (g and h) of glaciers in a constant climate (Ex. 1). The left column is the result of a case with 40 mW/m^2 geothermal heat flux, and the right column is a case with 160 mW/m^2 geothermal heat flux.

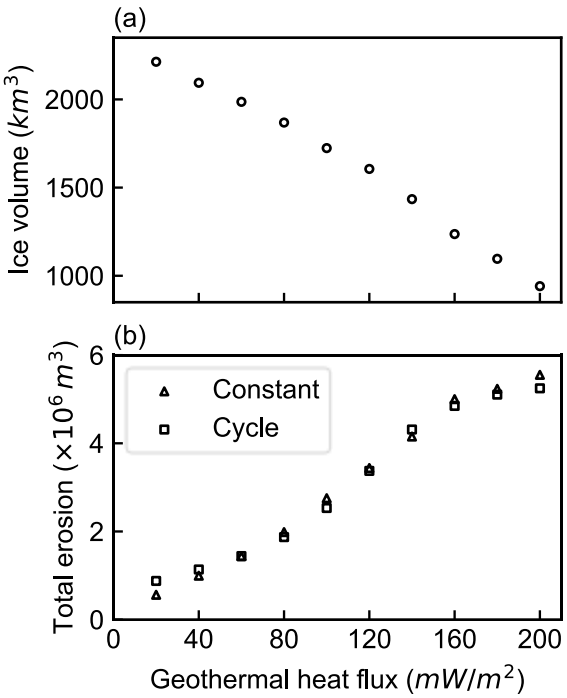

Figure 3.3 In Ex. 1, the total ice volume (a) decreases as the geothermal heat flux increases. Both constant (Ex. 2) and cyclic (Ex. 3a) climates predict increased total erosion as a function of the geothermal heat flux (b).

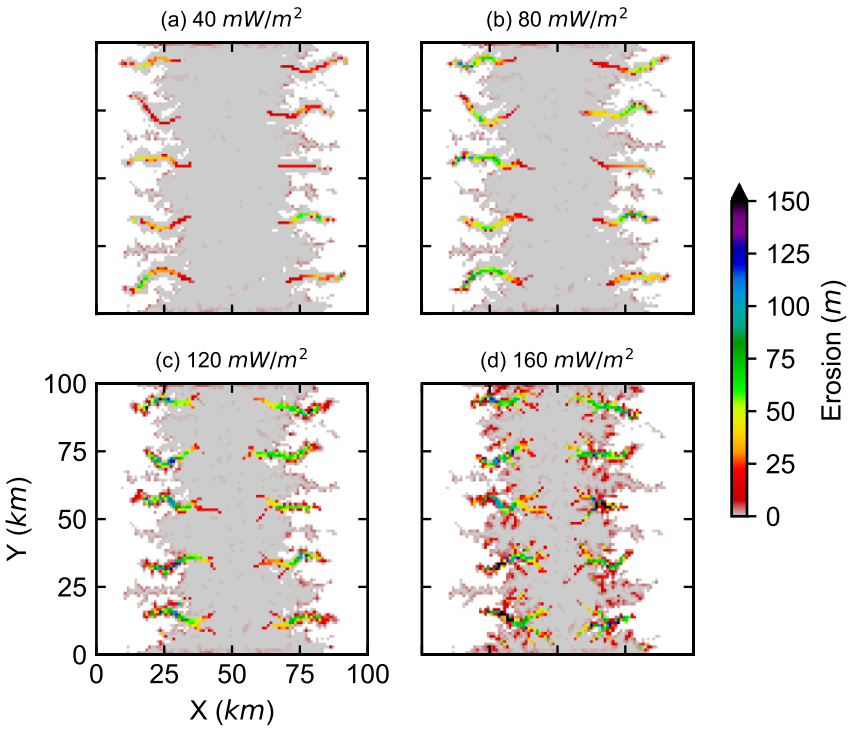

Figure 3.4 Total erosion after 20,000 years of evolution in a constant climate (Ex. 2).

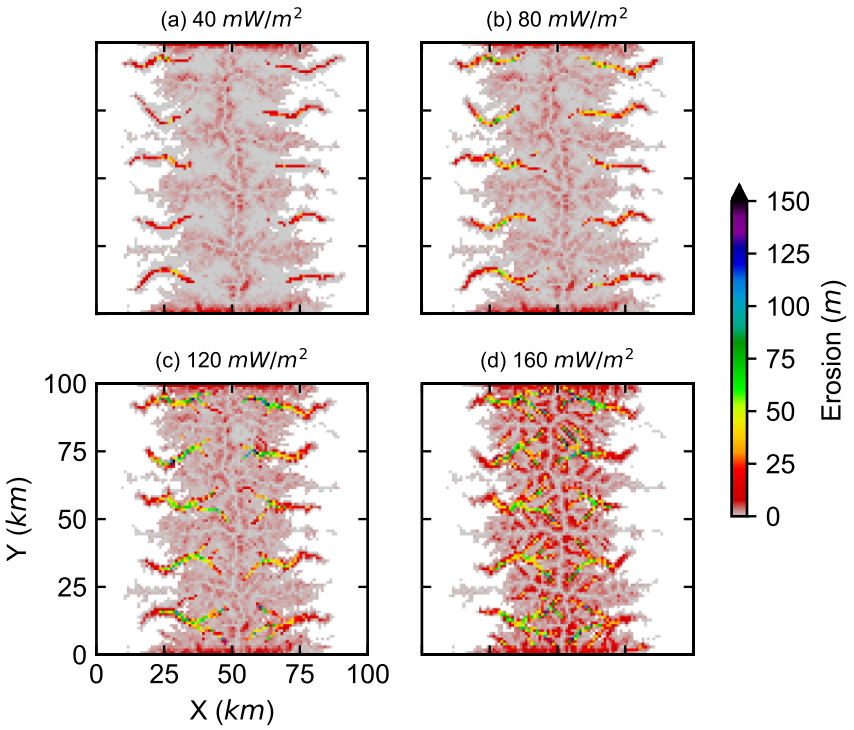

Figure 3.5 Total erosion during a 100,000-year glacial-interglacial cycle (Ex. 3a).

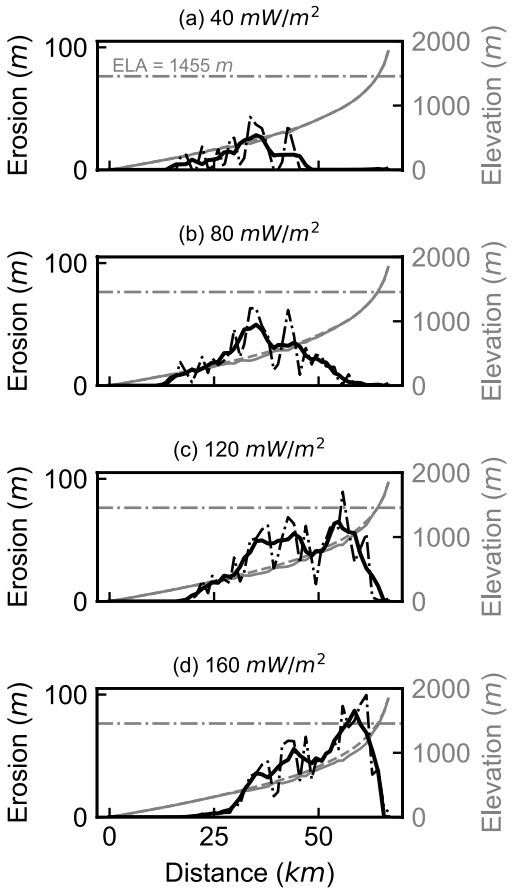

Figure 3.6 Total erosion (black dot-dash lines) and its 5-pixel moving average (black solid lines) during a glacial-interglacial cycle (Ex. 3a) along a valley long profile. The gray lines are bedrock topography before (dashed lines) and after (solid lines) erosion.

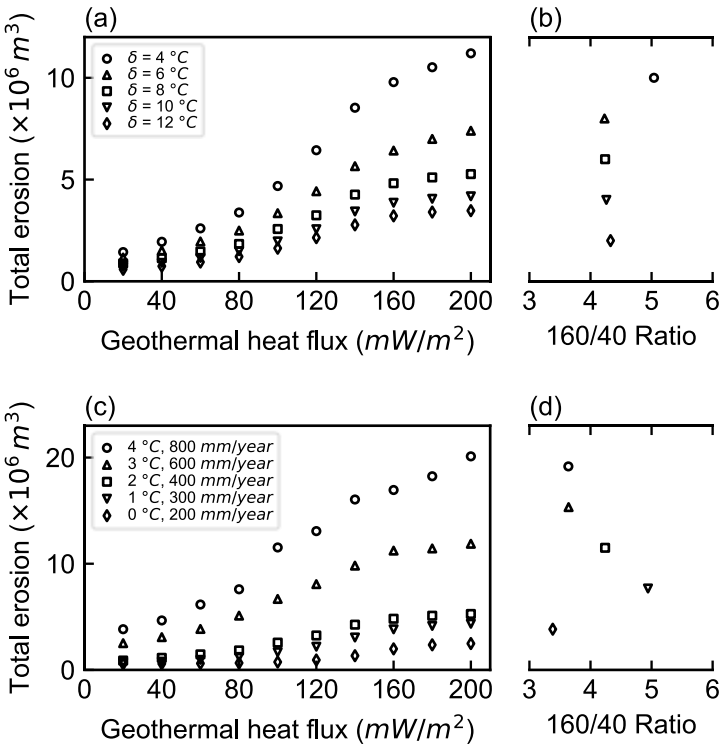

Figure 3.7 Total volume of erosion (a and c) and the ratio of total volume erosion between the case with 160 mW/m^2 geothermal heat flow and the case with 40 mW/m^2 geothermal heat flow (b and d) in Ex. 3b (upper panel) and Ex. 3c (lower panel).

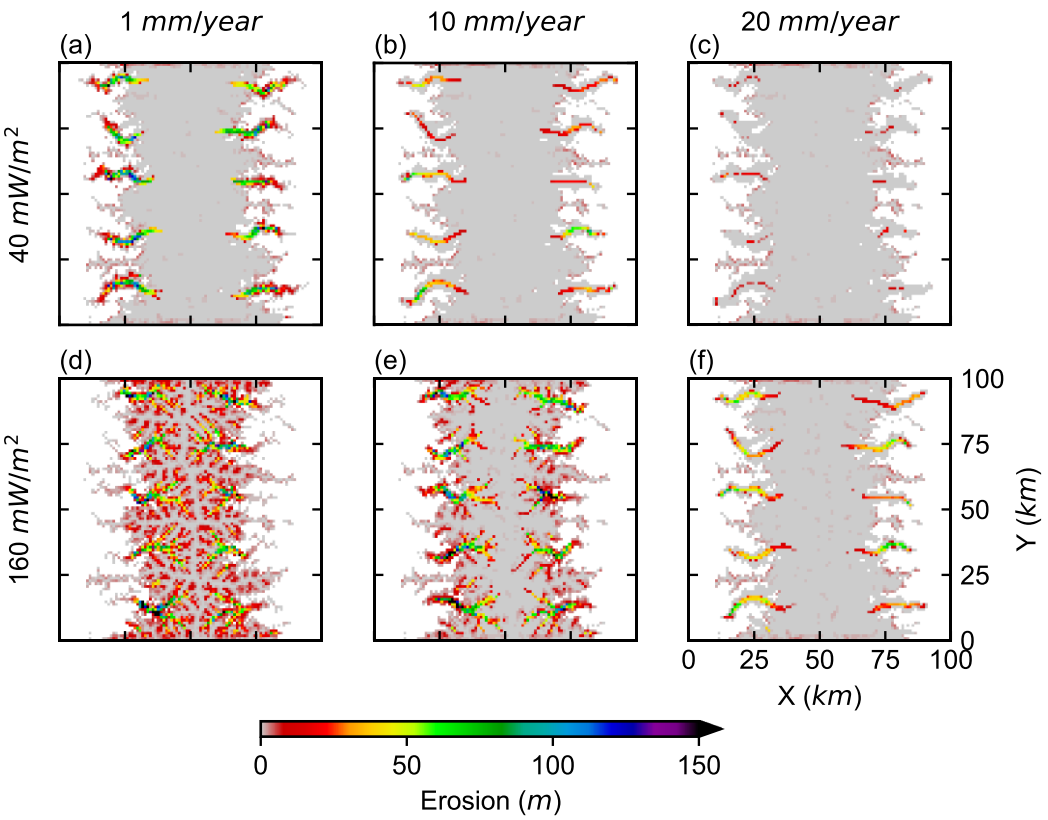

Figure 3.8 Total erosion after 20,000 years of evolution in a constant climate with different meltwater decay rate (Ex. 4). The left panel shows the results of cases with 1 mm/year meltwater decay rate. Middle and right panels are the results of cases 10 mm/year and 20 mm/year meltwater decay rates respectively.

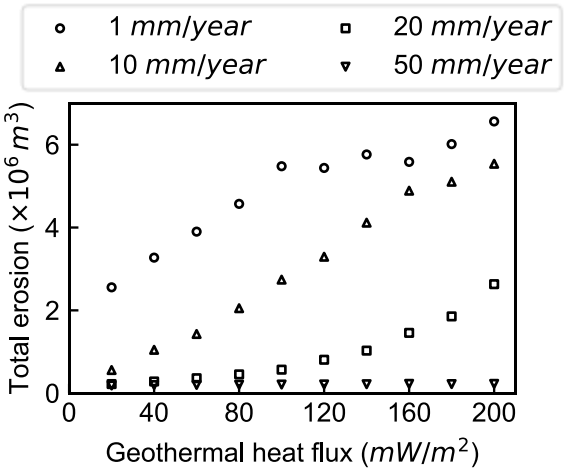

Figure 3.9 Total volume of erosion as a function of the geothermal heat flux (Ex. 4). Different symbols represent different values of meltwater decay rate.

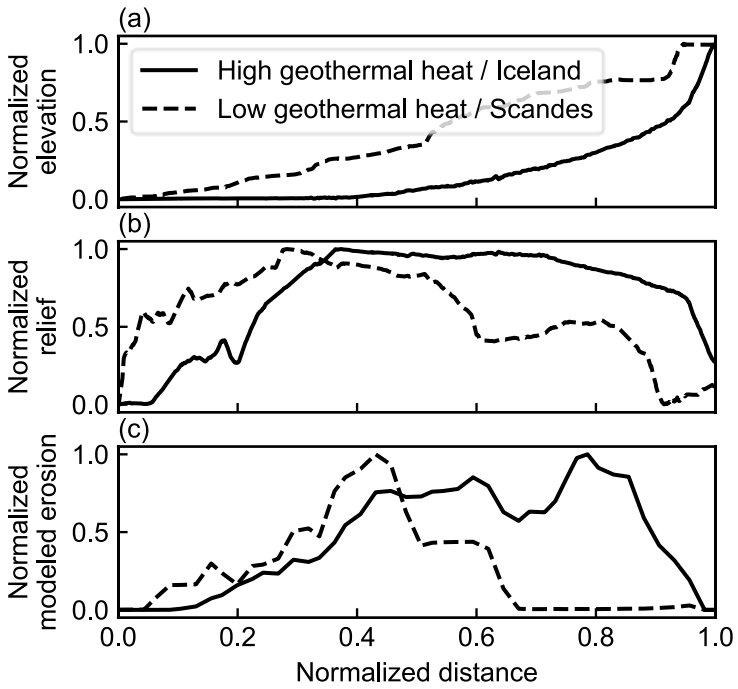

Figure 3.10 The channel long profiles (a) and geophysical relief along channels (b) of a basin from Iceland (solid lines) and a basin from the Scandes (dashed lines). The modeled glacial erosion along a channel in our synthetic landscape is shown in (c). The solid line in (c) represents the case with 120 mW/m^2 geothermal heat flux, and the dashed line is the case with 40 mW/m^2 geothermal heat flux. The data shown in (c) are the same as black solid lines in Fig. 6a and 6c. For comparison, however, the first 10-km of the profile at low elevations is not shown in (c).

Table 3.1 Approximate values of geothermal heat flow for glaciated mountain ranges in various tectonic environments. The data are from global compilations of heat flow by Davies (2013) and Goutorbe et al. (2011).

Locations	Geothermal heat flow (mW/m^2)
Active mountain ranges	
Alps	60-85
Washington Cascades	60-90
Southern Andes	70-150
SE Alaska	70
Hotspot/Spreading center	
Iceland	120-200
Passive continental margins	
Scandinavian Mountains	35
East Greenland	35

Table 3.2 Parameter values

Variable	Description	Unit	Value
C_s	Sliding constant in Weertman-style sliding law	$Pa^{-m} year^{-1} m^{-2}$	4.39
m	Exponent in Weertman-style sliding law		3
N_0	Reference effective pressure	Pa	1000
ρ_w	Density of water	$kg\ m^{-3}$	1000
δ	Lower limit of the effective pressure		0.02
e_0	void ratio at the reference effective pressure		0.69
C_c	Compressibility coefficient		0.12
W_0	Maximum thickness of subglacial water	m	2
C_w	Subglacial water decay rate	$m/year$	0.01
K_g	Erosion coefficient		0.00005
l	Exponent in erosion law		1

Table 3.3 Experiments
T represents mean annual temperature at sea level, and P is mean annual precipitation.

Experiments	Description
Ex. 1	Constant climate without glacial erosion T = 2 °C, P = 400 mm/year
Ex. 2	Constant climate with glacial erosion for 20,000 years T = 2 °C, P = 400 mm/year
Ex. 3a-c	Cyclic climate with glacial erosion for 100,000 years
Ex. 3a	At glacial maximum, T = 2 °C, P = 400 mm/year Glacial/interglacial temperature difference = 8 °C
Ex. 3b	At glacial maximum, T = 2 °C, P = 400 mm/year Glacial/interglacial temperature difference = 4 - 12 °C
Ex. 3c	At glacial maximum, T = 0 - 4 °C, P = 200 - 800 mm/year Glacial/interglacial temperature difference = 8 °C
Ex. 4	Constant climate with glacial erosion for 20,000 years T = 2 °C, P = 400 mm/year Subglacial water decay rate varies

CHAPTER 4: CLIMATIC CONTROLS ON MOUNTAIN GLACIER BASAL THERMAL REGIMES DICTATE SPATIAL PATTERNS OF GLACIAL EROSION

Abstract

The basal thermal regime of glaciers is a first-order control on the spatial patterns of glacial erosion. Polythermal glaciers contain both cold-based portions that protect bedrock from erosion and warm-based portions that actively erode bedrock. Climatic controls on the thermal structures of mountain glaciers and the spatial patterns of glacial erosion has received little study. In this study, we aim to fill this gap by modeling the impact of various climatic conditions on glacier basal thermal regimes and patterns of glacial erosion in mountainous regions. We couple a sliding-dependent glacial erosion model with the Parallel Ice Sheet Model (PISM) to simulate the evolution of the glacier basal thermal regime and glacial erosion in a synthetic landscape. We find that glacial erosion patterns follow the patterns of the basal thermal regime. Cold temperature leads to limited glacial erosion at high elevations due to cold-based conditions. Increasing precipitation could overcome the impact of cold temperature on the basal thermal regime by accumulating thick ice and lowering the melting point of ice at the base of glaciers. High precipitation rates, therefore, tend to cause warm-based conditions at high elevations, resulting in intensive erosion near the peak of the mountain range. Previous studies often assess the impact of climate on the spatial patterns of glacial erosion by integrating climatic conditions into the equilibrium line altitudes (ELAs) of glaciers, and glacial erosion is suggested to be maximal around the ELAs. However, our results show that different climatic conditions could produce glaciers with similar ELAs but different patterns of basal thermal regime and glacial erosion, suggesting that there might not be any direct correlation between ELAs and glacial erosion patterns.

4.1 Introduction

Earth's past climate has left an imprint on the topography of mountain ranges worldwide. During the late Cenozoic, global cooling induced widespread glaciation and glacial erosion

created unique landforms in mountainous regions including cirques, hanging valleys, and overdeepenings. Climate is a primary control on the pace and spatial variability of glacial erosion. Better constraint on this control is required to improve understanding of the development of topography worldwide during the climate perturbations of the late Cenozoic. However, a process-based model of how climatic conditions influence the rates and patterns of glacial erosion remains elusive.

Previous studies have suggested that glacial erosion is most effective at the equilibrium line altitude (ELA) of a glacier (e.g., Anderson et al., 2006; MacGregor et al., 2000). Numerical landscape evolution models that approximate the erosion rate as a function of sliding velocity also produce focused erosion near the ELA (e.g., Herman et al., 2011; MacGregor et al., 2000). In addition, the strong correlation between the mean or peak elevation of mountains and the ELAs of modern or past glaciers in some mid-latitude mountain ranges suggests that glacial erosion is concentrated near or above the ELA (Anders et al., 2010; Brozović et al., 1997; Egholm et al., 2009; Mitchell and Montgomery, 2006). Therefore, the impact of climate on glacial erosion is frequently assessed by integrating climatic conditions to locate the ELA. However, the correlation between ELAs and mountain heights breaks down in high-latitude mountain ranges because the frozen-based ice at high elevations causes limited erosion, resulting in high mountain peaks that sit above the ELAs (Thomson et al., 2010). Additionally, measurements of sediment production by modern glaciers reveal that the rates of glacial erosion vary as a function of the basal thermal regime (Koppes et al., 2015). These observations suggest that the basal thermal regime is a fundamental control on the rates and spatial patterns of glacial erosion and motivate us to consider the influence of climate on the basal thermal regime, rather than the ELA, as a primary control on glacial erosion.

The basal thermal regime is expected to exert first-order control on the spatial variability in glacial erosion. Basal sliding speed and meltwater pressure both strongly modulate the rate of glacial abrasion and quarrying (Hallet, 1979, 1996; Iverson, 2012) and are both controlled by the basal thermal regime. Below cold-based glaciers, basal ice is frozen to the bedrock and limited basal sliding and meltwater supply cause minimal glacial erosion. In contrast, warm-based glaciers erode their beds via abrasion and quarrying due to active basal sliding and meltwater production. Under large continental ice sheets, the contrast in erosive power between cold-based and warm-based portions of the ice sheets has been suggested to have caused selective linear

erosion of deep valleys and fjords along glaciated continental margins (Hall et al., 2013; Kleman and Glasser, 2007). Climate influences a glacier's basal thermal regime in two distinct ways. Atmospheric temperature controls the surface temperature of glaciers, and consequently influences the basal temperature via heat diffusion and advection. A colder climate, therefore, has greater potential for creating a cold basal layer that is frozen to the bedrock than a warmer climate. Glacier surface mass balance, which is driven by both precipitation and temperature, influences the basal thermal regime indirectly by controlling the ice thickness. Thick ice can result in a warm basal layer without changing basal temperature because of the pressure dependence of the melting point of ice. Warm-based glaciers are more likely occur when high ice accumulation rates and/or low ablation rates create thick glacial ice. Therefore, a wet climate is expected to yield glaciers with larger warm-based portions than a dry climate. We explore the influence of precipitation and temperature on the spatial pattern of glacial erosion that arises through modulation of the basal thermal regime.

While polythermal glaciers that contain both warm-based and cold-based portions are common in mountainous regions, the influence of the basal thermal regime on the erosion of alpine glaciers has received little study. Previous glacial landscape evolution models often neglect the basal thermal regime by assuming the glacier is entirely warm-based (e.g., MacGregor et al., 2000; Prasicek et al., 2018). A few studies have examined polythermal mountain glaciers and demonstrated that a cold climate may produce cold-based ice at high elevations (Tomkin and Braun, 2002; Yanites and Ehlers, 2012). However, the thermodynamics of ice in these early glacial landscape evolution models is oversimplified. The basal temperature is approximated by using a one-dimensional column model that accounts for the vertical heat transportation and neglects the longitudinal component (Tomkin and Braun, 2002). In our previous work (Lai and Anders, 2020), we built a landscape evolution model that includes a more sophisticated representation of thermodynamics (Aschwanden et al., 2012). Our previous focus was on how geothermal heat fluxes influence the basal thermal regime and glacial erosion. In this study, we use our glacial landscape evolution model with a thermodynamically coupled ice dynamics model to investigate the climatic control on the rates and patterns of glacial erosion through the basal thermal regime. We present a series of numerical simulations that allow us to assess the correlation between the basal thermal regimes of glaciers and the rates and patterns of sliding-driven glacial erosion under a range of climatic settings.

4.2 Methods

We build a landscape evolution model with the Parallel Ice Sheet Model (PISM, http://www.pism-docs.org) to simulate the evolution of glacial landscapes. The approach we use in this study is similar to that presented in Lai and Anders (2020) where we first added glacial erosion to PISM. In this study, we extend that model by adding fluvial incision and bedrock uplift to the landscape evolution model. In this section, we briefly summarize the different components of our model.

4.2.1 Ice flow model – Parallel Ice Sheet Model

To solve for ice flow, PISM uses a hybrid stress balance scheme that combines the Shallow Ice Approximation (SIA; Hutter, 1983) for internal deformation and the Shallow Shelf Approximation (SSA; Morland, 1987) for membrane stress (also known as longitudinal stress). The membrane stress is an important component in balancing the driving stress in alpine glaciers (Bueler and Brown, 2009; Hindmarsh, 2006). Basal sliding velocity is related to the basal shear stress through a Weertman-style sliding rule and it is controlled by the balance between basal shear stress, membrane stress, and driving stress. Basal sliding velocity is also controlled by the amount of subglacial meltwater through a simple subglacial hydrology model. The conservation of energy is solved using an enthalpy-based scheme in PISM (Aschwanden et al., 2012). The governing equations of PISM are presented in Bueler and Brown (2009) and Winkelmann et al. (2011) and we refer readers to these work for a detailed description of the model.

PISM has been used to simulate the contemporary Greenland Ice Sheet and the result shows a good correlation between modeled and observed ice surface velocity (Aschwanden et al., 2016). PISM has also been used to reconstruct the complex history of glaciation in mountainous regions (e.g., Golledge et al., 2012; Seguinot et al., 2018).

4.2.2 Landscape evolution model

The evolution of bedrock topography is controlled by glacial erosion, fluvial incision, and uplift. At each time step, bedrock topography is uplifted at a uniform and constant rate across the model domain. In areas where the thickness of ice is greater than 10 m, only glacial erosion can change the topography, and in other areas, only fluvial incision is allowed to occur. We assume

that all eroded materials are transported out of the model domain efficiently so that there is no deposition in the system.

4.2.2.1 Glacial erosion model

The rate of glacial erosion, E_g, is modeled as a linear function of the sliding velocity, $\boldsymbol{u}_s$:

$$E_g = K_g|\boldsymbol{u}_s|, \tag{4.1}$$

where K_g is an erodibility coefficient. In this study, the value of K_g is 0.0001 in all simulations. This erosion model has been widely used in glacial landscape evolution models (e.g., Egholm et al., 2011; Herman et al., 2011; MacGregor et al., 2000; Tomkin and Braun, 2002; Yanites and Ehlers, 2012). This model is supported by theoretical studies of glacial abrasion (Hallet, 1979) and it is a reasonable approximation of glacial erosion when abrasion dominates glacial erosion (Humphrey and Raymond, 1994). Although glacial erosion by quarrying is complicated by the subglacial hydrological conditions (Hallet, 1996; Iverson, 2012), this basal-sliding model still reproduces the qualitative patterns of glacial erosion from a numerical model driven by a quarrying law (Ugelvig et al., 2016). A common shortcoming of this model is that steep bedrock slopes can produce unrealistic high erosion rates and trigger runaway effects (Herman et al., 2011). To avoid this, we do not allow bedrock slopes to exceed a threshold value of 45°. If the slope of bedrock topography reaches the threshold value, glacial erosion is prohibited.

4.2.2.2 Fluvial incision model

Fluvial incision is modeled using the stream power incision model (Whipple and Tucker, 1999). The rate of fluvial incision, E_f, is a function of drainage area, A, and bedrock slope, S:

$$E_f = K_f A^m S^n, \tag{4.2}$$

where K_f is an erodibility coefficient and m and n are constants. The value of K_f is independent of climate and it is uniform and constant in all simulations. In this study, the value of K_f is 0.00001 in all simulations, and m and n are 0.5 and 1, respectively. Flow direction is approximated using the D8 algorithm and the drainage area is calculated using the Fastscape algorithm (Braun and Willett, 2013). In our implementation, the drainage area includes upstream areas occupied by glaciers. In glaciated areas, the direction of water flow is determined based on ice surface elevation rather than bedrock elevation. Fluvial incision only applies to the areas outside of the glacial realm, and in glaciated areas, the rate of fluvial incision is set to zero.

Ideally, the fluvial incision model should reflect the influence of glacier meltwater and precipitation on fluvial incision. However, the goal of this study is to investigate the climatic controls on glacial erosion through basal thermal regime, and incorporating a sophisticated fluvial incision model could make it difficult to isolate the impact of climatic conditions on glacial erosion. Therefore, we simply model fluvial incision using the stream power incision law.

4.2.3 Initial bedrock topography

The initial bedrock topography is a synthetic fluvial landscape created in the Landlab model platform (Hobley et al., 2017). The fluvial landscape is a 100-km by 100-km mountain range with 20-km wide piedmont plains on each side (Fig. 4.1). The piedmont plains are removed in all figures for a clear illustration of the mountain range. The fluvial incision model used for creating the initial topography is the same as the model described in 4.2.2. and the value of the fluvial erodibility coefficient is also 0.00001. The rate of uplift is 0.0035 m $year^{-1}$. The uplift rate and fluvial erodibility coefficient used for creating the initial topography are maintained in the subsequent glacial erosion simulations. Fluvial incision and rock uplift are in equilibrium in the initial topography such that the fluvial incision rate equals the rock uplift rate. The initial topography has a relief of ~3000 m and the mountain range have 5 major valleys on each side. The grid resolution is 1 km. This resolution is chosen because it provides a reasonable balance between accuracy and efficiency in PISM (Aschwanden et al., 2016).

4.2.4 Climate forcing

Climate forcing is represented by the mean annual temperature at sea-level and mean annual precipitation, and PISM takes these two parameters as input values to calculate the ice surface mass balance. Spatially, the mean annual temperature decreases as the elevation rises with a lapse rate of 6.5 °C km^{-1}, and the mean annual precipitation is uniform across the model domain. Temporally, the seasonal variation of temperature is modeled by a sinusoidal function with the summer temperature is assumed to be 5 °C higher than the mean annual temperature. There is no seasonal variation in precipitation. A positive degree day (PDD; Calov and Greve, 2005) model then calculates the ice surface mass balance based on temperature and precipitation.

In all simulations, we use a 100,000-year glacial-interglacial cycle with a “saw-tooth” variation of temperature. The mean annual temperature at sea-level decreases by 8 °C linearly for

80,000 years and then increases linearly for 20,000 years. The mean annual precipitation increases by 7.2% for every one degree Celsius of increase in temperature (Huybrechts, 2002).

4.2.5 Experiment design

We explore the impact of climatic conditions on glacial erosion by varying the mean annual temperature at sea-level and mean annual precipitation at the glacial maximum. The glacial mean annual temperature at sea-level ranges from 1 to 5 °C and the mean annual precipitation at glacial maximum ranges from 200 to 3000 mm $year^{-1}$. All the parameters in the landscape evolution models including the glacial erosion coefficient, the stream power erosion coefficient, and the bedrock uplift rate are held constant in all the simulations.

4.3 Results

In order to highlight the climatic controls on the basal thermal regime of glaciers and spatial patterns of glacial erosion, we first compare a set of models in which different climate conditions produce similar ELAs at the glacial maximum. For these climate conditions, we examine not only the output of our landscape evolution model, but also consider the output from PISM over an unchanging topography. These glaciation-only cases isolate the impact of climate on the basal thermal regime because they avoid any feedbacks between evolving topography and the basal thermal regime. We then implement our landscape evolution model and evaluate the diverse morphology of the landscapes that result from different climates with similar ELAs. Next, we compare the results of groups of simulations with different mean annual sea-level temperatures and the same mean annual precipitation rate at the glacial maximum to explore the sensitivity of the spatial pattern of glacial erosion to temperature. Finally, we compare the results of cases with different mean annual precipitation rates and the same mean annual sea-level temperature at the glacial maximum to investigate the influence of precipitation.

4.3.1 Climatic controls on the basal thermal regime

We begin by exploring the sensitivity of basal thermal regimes to climatic conditions by comparing results of glaciation-only cases in which landscape evolution models are not enabled. In order to highlight that the basal thermal regime is not coupled with the ELA, we compare the results of three simulations with similar ELAs at the glacial maximum but different climatic

conditions. Unsurprisingly, the basal thermal regimes of simulated glaciers are distinct in each case and strongly controlled by climatic conditions, despite the similarity in ELA and ice extent across all the cases (Fig. 4.2). Different climatic conditions in the three simulations produce similar ELAs around 1300m at glacial maximum. As a result, the modeled extent and thickness of ice at the glacial maximum is also similar in different cases (Fig. 4.2a-c). The basal thermal regimes at glacial maximum, however, vary significantly as a function of climate despite the similar ice extent and thickness (Fig. 4.2d-f). In a cold and dry climate (1 °C, 400 mm $year^{-1}$), warm basal ice only occurs in major valleys because the thick ice lowers the melting point of ice, while glaciers at high elevations are mostly cold-based due to the cold temperature (Fig. 4.2d). As the climate transitions into warmer conditions, glaciers near the center of the range shift to warm-based condition, and areas with warm basal ice extend into higher elevations (Fig. 4.2e). In the warmest climate (5 °C, 1600 mm $year^{-1}$) most of the glaciers are warm-based (Fig. 4.2f). The different basal thermal regimes have the potential for producing distinct glacial erosion patterns, as we will show in the next section.

4.3.2 Spatial patterns of erosion controlled by basal thermal regime

Having demonstrated that climate strongly influences the distribution of warm ice in the absence of erosion, we now implement glacial and fluvial erosion and rock uplift to compare the modeled glacial erosion in three cases with different climates but similar ELAs. We quantify the average basal thermal regimes over a glacial-interglacial cycle by calculating the percentage of time with warm-based conditions during a cycle. In all simulations, glacial erosion tends to focus in areas where the basal ice is mostly warm throughout the whole cycle (Figs. 4.3 and 4.4). In the case with a cold and dry climate (1 °C, 400 mm $year^{-1}$), glaciers are perennially cold-based at high elevations (Figs. 4.3g and 4d), leading to limited glacial erosion at high elevations near the center of the range (Figs. 4.3d and 4.4a). Warm-based areas are mostly found in major valleys (Figs. 4.3g and 4.4d). During a glacial-interglacial cycle, middle parts of the valleys are influenced by warm-based glaciers for a longer period than lower parts of the valley (Figs. 4.3g and 4.4d) because the lower parts are only covered by glacial ice for a limited period during the coldest intervals. Consequently, most glacial erosion occurs in the middle parts of major valleys (Figs. 4.3d and 4.4a). In contrast, in a warm and wet climate (5 °C, 1600 mm $year^{-1}$), warm-based areas extend into higher elevations than in a cold and dry climate and glaciers are

constantly warm-based at high elevations (Figs. 4.3i and 4.4f). The area with significant glacial erosion also migrates towards the center of the range at high elevations in a warm and wet climate (Figs. 4.3f and 4.4c).

The different spatial patterns of glacial erosion lead to distinct landforms in different climates. In a cold and dry climate, the glacial erosion rate exceeds the bedrock uplift rate in major valleys, producing overdeepenings and increasing local relief, while at high elevations, pre-glacial landforms are preserved under cold-based glaciers and a limited amount of erosion allows for an increase of the elevation of some peaks (Figs. 4.3a and 4.5a). In contrast, in a warm and wet climate, significant erosion at high elevations lowers the peaks and efficiently reshapes the topography near the center of the range, creating cirque-like landforms and overdeepenings near the peaks (Figs. 4.3c and 4.5c). Distinct landscapes caused by variation in basal thermal regimes are also reflected by changes in the hypsometry of the topography (Fig. 4.6). In a cold and dry climate, the relief of the mountain range is increased after a glacial-interglacial cycle, while the relief is decreased in a warm and wet climate, even when the ELAs at the glacial maximum are similar.

4.3.3 Sensitivity to temperature

Air temperature is one of the primary controls on the glacier basal thermal regime. We compare cases with different mean annual sea-level temperature and the same precipitation rate at the glacial maximum. In general, lowering the air temperature causes increases in glacial erosion rates (Fig. 4.9). Unsurprisingly, the extent of glaciation is strongly controlled by the air temperature. In a warm climate, glaciers are restricted to the upper part of the mountain range due to the relatively high ELA, while in cooler climates the majority of the mountain range is influenced by glaciation (Fig. 4.7). Glaciers in a warm climate are mostly warm-based throughout the cycle and most glacial erosion occurs at high elevations because high elevation regions are influenced by warm basal ice for a longer period than lower elevations (Figs. 4.7 and 4.9). As the climate transitions into a cold one, it is commonly expected that the basal thermal regime at high elevations will shift from warm-based to cold-based. As we showed in the previous section, a cold and dry climate could result in cold-based conditions at high elevations (Figs. 4.3 and 4.4). In relatively dry climates, the distribution of glaciers is restricted within high elevation regions, causing a small amount of glacial erosion primarily focusing on the center of

the range (Fig. 4.7b and 4.7c). As temperature rises in dry climates, glacial ice near the center of the range transitions into warm-based conditions, and glacial erosion starts to occur at high elevations (Fig. 4.6). Warm temperature in dry climates also produces small glaciers that are restricted to high elevation regions, causing a small amount of glacial erosion primarily focusing on the center of the range (Fig. 4.7b and 7c). However, in relatively wet climates, the basal thermal regime at high elevations remains warm-based as the temperature decreases (Fig. 4.7d-f). In a cold but relatively wet climate, high elevation regions are perennially coved by warm-based rather than cold-based glaciers, allowing for a great amount of erosion at high elevations (Fig. 4.7d). This indicates that the sensitivities of glacier basal thermal regimes and consequently the spatial pattern of glacial erosion to air temperature are dependent on the precipitation rates. A relatively wet climate could allow for warm-based areas at high elevations even in a cold climate. In the next section, we will further investigate the influence of precipitation on basal thermal regimes and glacial erosion.

4.3.4 Sensitivity to precipitation

We compare cases with different mean annual precipitation rates but the same air temperature at the glacial maximum. Increasing precipitation lowers the ELA by expanding the accumulation zone of glaciers. As expected, glaciers are smaller in a dry climate than in a wet climate, resulting in less glacial erosion (Fig. 4.9). There is a potential for a larger warm-based area in a wet climate than a dry climate because the thick ice in a wet climate lowers the melting point of ice and works to prevent the dissipation of heat accumulated at the base of ice. Increasing precipitation in cold climates allows warm-based ice to occur at increasingly high elevations. As a result, in cold climates, the area with significant erosion migrates into high elevations toward the center of the range as the climate becomes wetter (Figs. 4.8a-c and 4.9) despite that the ELAs are lowered by high precipitation rates. In contrast, increasing precipitation in warm climates has little impact on the basal thermal regime because the glaciers are mostly warm-based already. In warm climates, glacial erosion constantly focuses at high elevations as the precipitation increases (Figs. 4.8d-f and 4.9), although the glaciers become larger in a wetter climate.

4.4 Discussion

4.4.1 ELA, basal thermal regime, and the location of maximum glacial erosion

Previous studies of glacial erosion and glacial landscapes have emphasized the role of ELA in controlling the spatial patterns of erosion. The correlation between ELA and the spatial patterns of erosion partially arises from a simple framework: if we assume the rate of glacial erosion to a first-order scales with ice discharge (Anderson et al., 2006), then glacial erosion tends to focus around the ELA because ice discharge peaks at the ELA. Although ice discharge is a convenient proxy for erosion, many studies have shown that glacial erosion is controlled by sliding velocity (Hallet, 1979; Herman et al., 2015), subglacial hydrology (Beaud et al., 2014; Herman et al., 2011), and basal thermal regime (Koppes et al., 2015). In temperature glaciers with mostly warm basal ice, basal sliding occurs throughout the whole glacier and therefore, basal sliding velocity scales, to first order, with ice discharge. Subglacial meltwater, however, tends to focus in the ablation zone and promotes sliding and erosion in low elevation areas (Herman et al., 2011). The basal thermal regime is not correlated with ice discharge or ELA. Our previous work (Lai and Anders, 2020) showed that geothermal heat from the underlying bedrock can significantly change the basal thermal regime of glaciers without any changes in surface conditions, including the ELA. In this study, our numerical simulations show that the trade-off between temperature and precipitation could results in glaciers with similar ELAs but different basal thermal regimes (Fig. 4.2) as well as distinct patterns of glacial erosion (Figs. 4.3 and 4.4). Our results indicate that the patterns of glacial erosion are closely tied with the basal thermal regime rather than the ELA. Overall, based on our results and previous studies, we suggest that there might not be any direct spatial correlation between the ELA and the location of maximum erosion.

The observed agreement between mountain peak elevations and reconstructed past ELAs, i.e., the glacial buzzsaw hypothesis (Brozović et al., 1997; Egholm et al., 2009; Mitchell and Montgomery, 2006), suggests glaciers might focus their erosion at or above the ELAs. However, the past ELAs are often reconstructed using the cirque floor elevations (Mitchell and Montgomery, 2006; Porter, 1989, 2000), and they might represent the average glacial conditions rather than the actual ELA determined by a specific climate (Barr and Spagnolo, 2015; Porter, 1989). Cirques are formed over multiple glacial/interglacial cycles and the development of a cirque is thought to primarily occur during periods with modest climate when the glacier is

restricted within the cirque and is mostly warm-based (Barr and Spagnolo, 2015). The cirque floor elevations, therefore, are determined by the average intermediate conditions over multiple glacial/interglacial cycles. As the cooling climate leads to more extensive glaciations, cirque enlargement might cease because the cirque is covered by cold-based ice, and the climatic conditions during these more extensive glaciation periods are not recorded cirques. Our model results show that, although periods with extensive glaciation only occupy a short time interval of the whole glacial/interglacial cycle, the warm-based valley glaciers produce large amounts of erosion in major valleys during periods with extensive glaciation (Fig. 4.5). This observation from numerical simulations is also supported by the presence of widespread overdeepenings in glaciated mountain ranges (Magrani et al., 2020). For this reason, we suggest that cirque-based ELA estimates might not be an appropriate proxy for assessing the influence of past climate on glacial erosion, and their correlation with mountain peak elevations cannot support the idea that climate controls the spatial patterns of glacial erosion via changing ELAs. Observations of cirque floor elevation and cirque headwall relief suggest that cirques may set the base level for the hillslope processes that potentially limit the mountain peak elevations (Anders et al., 2010; Mitchell and Montgomery, 2006), and therefore, we speculate that the observed trend is the correlation between peak elevations and planes defined by cirque floors.

4.4.2 Glacial erosion controlled by precipitation

Precipitation is the primary driver of fluvial incision (e.g., Ferrier et al., 2013) and hillslope erosion (e.g., Moon et al., 2011). In this study, we observe a wide range of glacial erosion rates as a function of precipitation. The rate of glacial erosion increases by 2 orders of magnitude as the precipitation rate rises by a factor of 8 (Fig. 4.9). In cold conditions, increases in precipitation also change the basal thermal regime and cause a large amount of erosion at high elevations (Fig. 4.8). This finding suggests that in addition to past temperature, past precipitation is also an important component when assessing past glacial erosion history. Most previous studies focusing on the impact of climate on glacial erosion have put an emphasis on the role of temperature in lowering the ELAs and in controlling basal thermal regime (e.g., Thomson et al., 2010; Yanites and Ehlers, 2012). It is often suggested that glacial erosion is lower cold high-latitude regions because the cold temperature implies more frequent cold-based conditions. However, our results show that high precipitation rates could overcome the influence of cold

temperature on the basal thermal regime by accumulating thick ice and lowering the melting point of ice. Our simulations also show that increasing precipitation could result in a drop in ELA, and this finding is consistent with field observations (Oien et al., 2020). Therefore, we suggest that precipitation should be viewed as equally important as temperature when assessing the influence of climate on glacial erosion. In most previous glacial landscape evolution models, precipitation is often integrated into the mass balance term or changes as a function of temperature (e.g., Herman et al., 2011; Yanites and Ehlers, 2012). We suggest that precipitation should be viewed as an independent component in glacial landscape evolution models.

4.5 Conclusions

In this study, we investigate the impact of climatic conditions on the basal thermal regime of glaciers and glacial erosion patterns, using a landscape evolution model coupled with an ice sheet model. Our results indicate that the spatial patterns of glacial erosion follow the patterns of the basal thermal regime. Cold temperatures create cold-based glacier areas at high elevations, while high precipitation rates tend to cause warm-based conditions by increasing the thickness of glaciers and lowering the melting point of ice. Glaciers in a cold and dry climate have limited erosion at high elevations due to cold-based conditions, and most glacial erosion focuses at low elevations in major valleys. On the contrary, a warm and wet climate causes a large amount of erosion at high elevations. Our results do not support the direct correlation between the ELA and the patterns of glacial erosion, because different temperature and precipitation combinations could produce glaciers with similar ELAs but distinct basal thermal regimes.

4.6 Figures

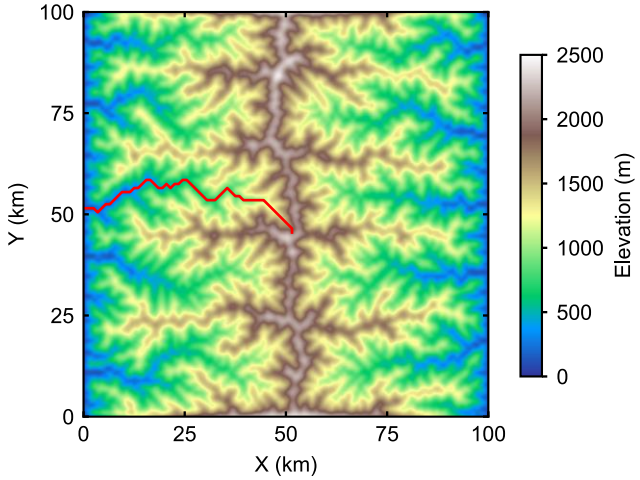

Figure 4.1 The initial bedrock topography is a synthetic fluvial landscape, representing a typical pre-glacial setting. The piedmont plains are not shown in the figure for clear illustration. The red curve indicates the valley profile shown in Fig. 4.4.

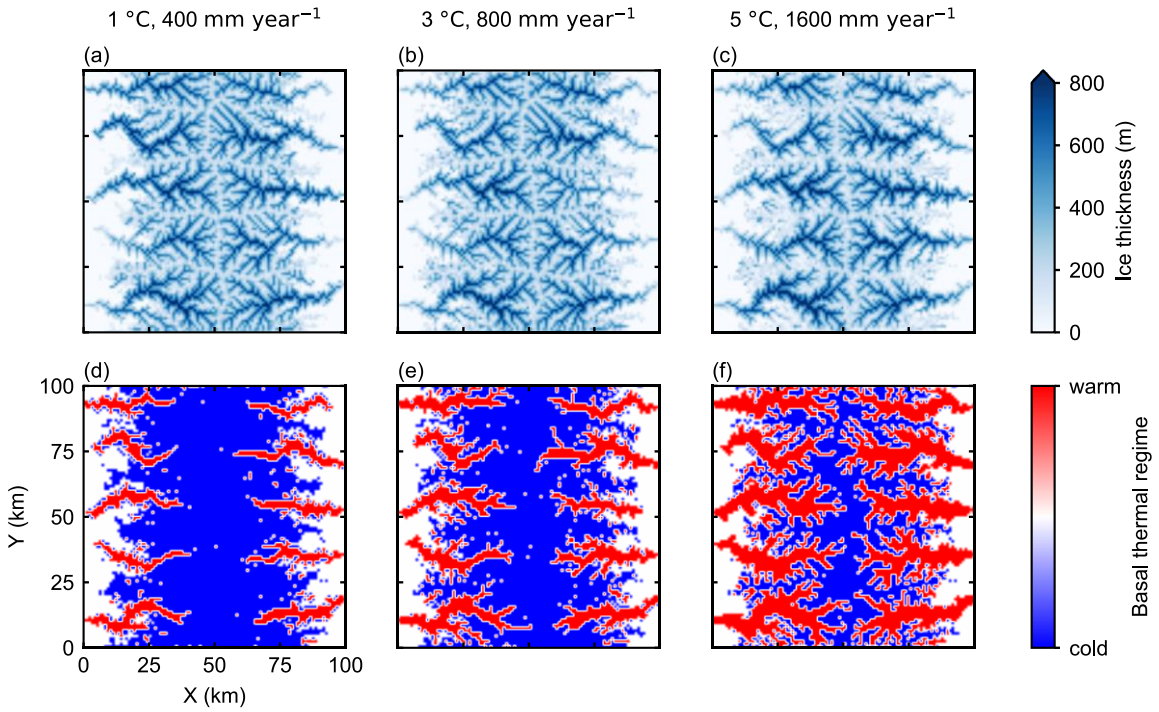

Figure 4.2 2-D mapview of modeled ice thickness (a-c) and basal thermal regime (d-f) at glacial maximum. The left column (a and d) is the case with a mean annual temperature of 1 °C at sea-level and a mean annual precipitation of 400 mm year^{-1} at the glacial maximum, corresponding to a glacial ELA of 1300m. The middle column (b and e, glacial mean annual temperature at sea-level = 3 °C, glacial mean annual precipitation = 800 mm year^{-1}) and right column (c and f, glacial mean annual temperature at sea-level = 5 °C, glacial mean annual precipitation = 1600 mm year^{-1}) are cases with warmer and wetter climate than the left column, but the glacial ELAs are roughly the same as the left column.

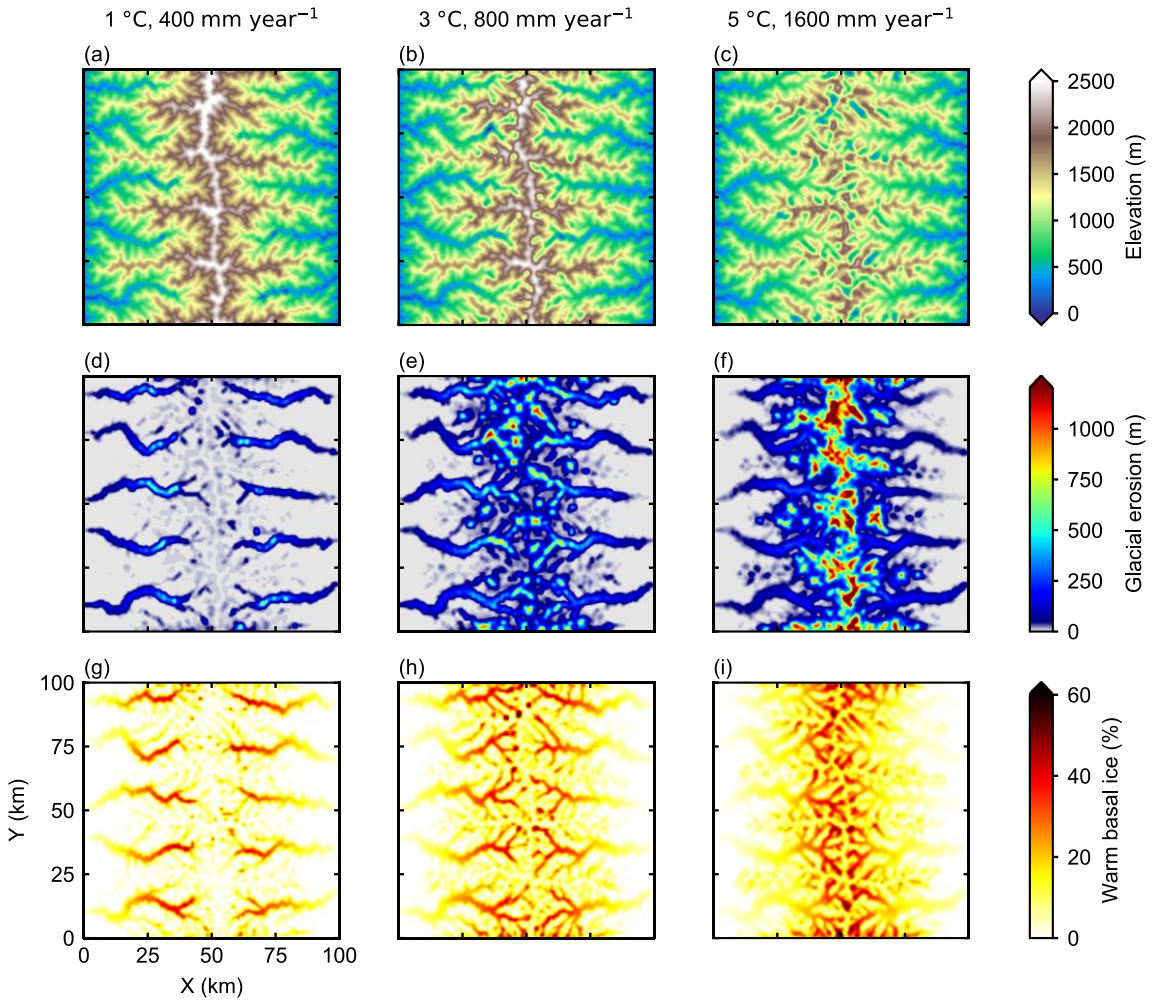

Figure 4.3 2-D mapview of the modeled topography after a glacial-interglacial cycle (a-c), amount of glacial erosion (d-f) and percentage of time with warm basal ice (g-i). Each column represents model results for a specific climate. The three climatic settings produce similar ELAs around 1300m.

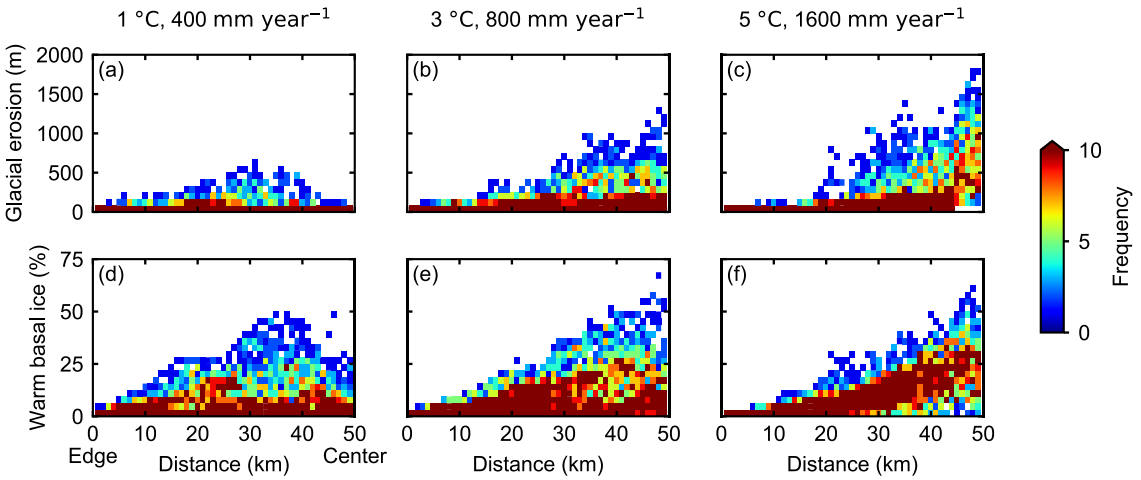

Figure 4.4 Spatial variability in glacial erosion (a-c) and percentage of time with warm basal ice (d-f). The x-axes are the distance from the left or right edge of the domain. The color scheme represents the frequency of pixels for a given combination of glacial erosion/percentage of time with warm basal ice and distance. Each column represents model results for a specific climate. The three climatic settings produce similar ELAs around 1300m.

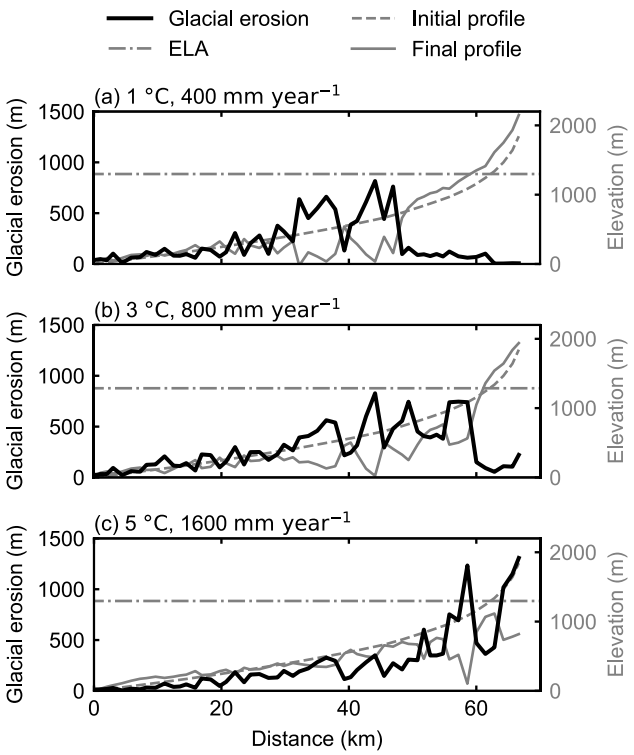

Figure 4.5 Glacial erosion (black lines), initial elevation (gray dashed lines) and finial elevation (gray solid lines) along a valley long profile. The location of the valley profile is shown as a red curve in Fig. 4.1. Horizontal gray dash-dotted lines represent glacial ELAs. Although the glacial ELAs are similar in three cases, the spatial patterns of glacial erosion are different.

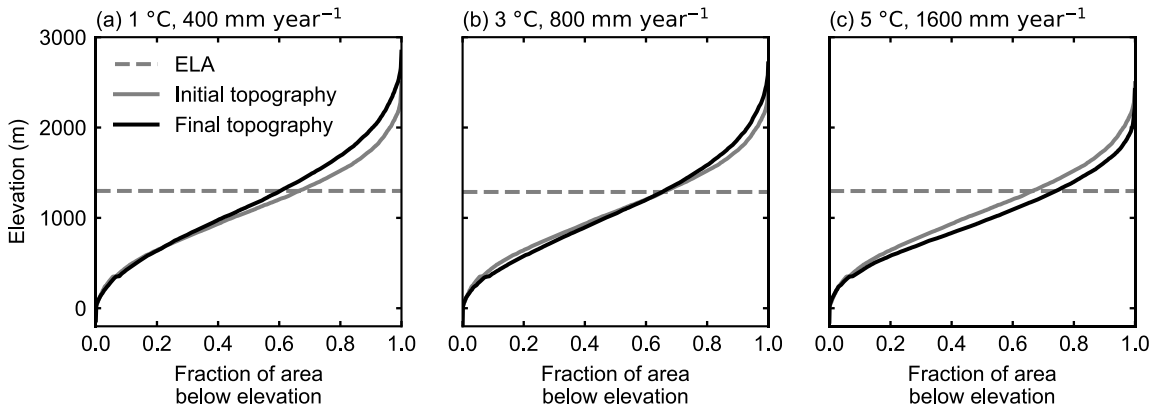

Figure 4.6 Hypsometric evolution of modeled landscapes in different climates. Initial topography is shown in gray solid lines and final topography is shown in black. Horizontal gray dashed lines indicate the ELAs.

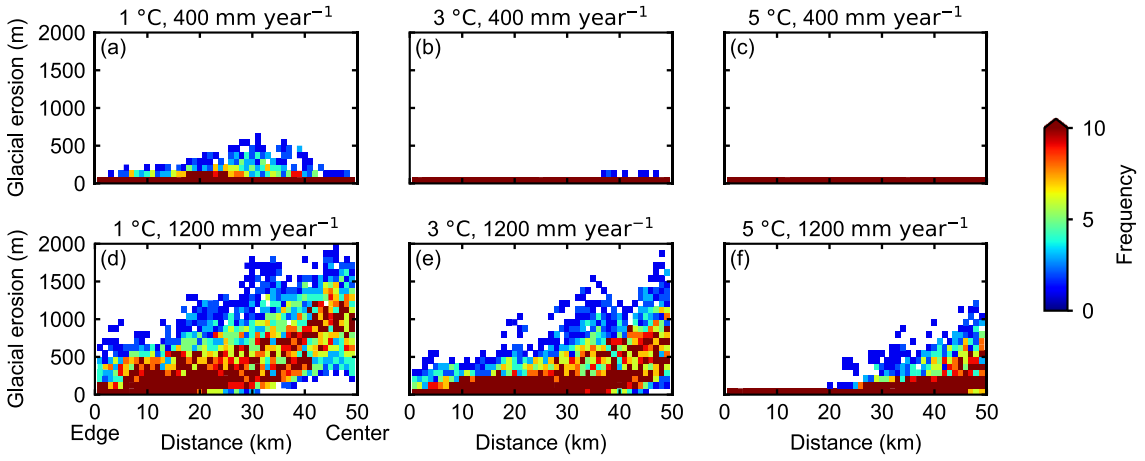

Figure 4.7 Influence of temperature on the spatial variability in glacial erosion. Each panel represents the result for a specific climate. (a-c): The mean annual precipitation rate is 600 mm year^{-1} at glacial maximum in all three cases and the mean annual temperatures are 1, 3, and 5 °C, respectively. (d-e): The mean annual precipitation rate is 1400 mm year^{-1} at glacial maximum in all three cases and the mean annual temperatures are 1, 3, and 5 °C, respectively.

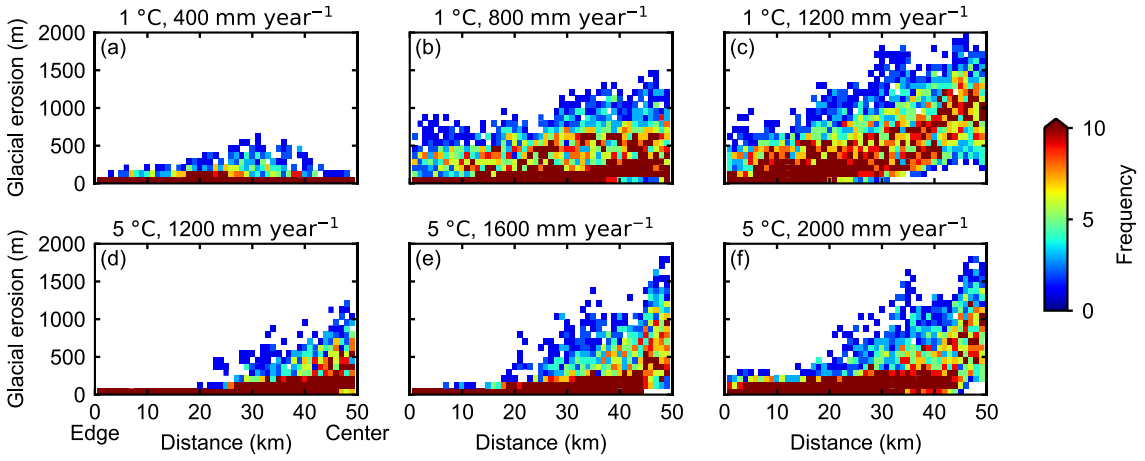

Figure 4.8 Influence of precipitation on the spatial variability in glacial erosion. Each panel represents the result for a specific climate. (a-c): The mean annual temperature at sea-level is 1 °C at glacial maximum in all three cases and the mean annual precipitation rates at glacial maximum are 400, 800, and 1200 mm year^{-1}, respectively. (d-e): The mean annual temperature at sea-level is 5 °C at glacial maximum in all three cases and the mean annual precipitation rates at glacial maximum are 1200, 1600, and 2000 mm year^{-1}, respectively.

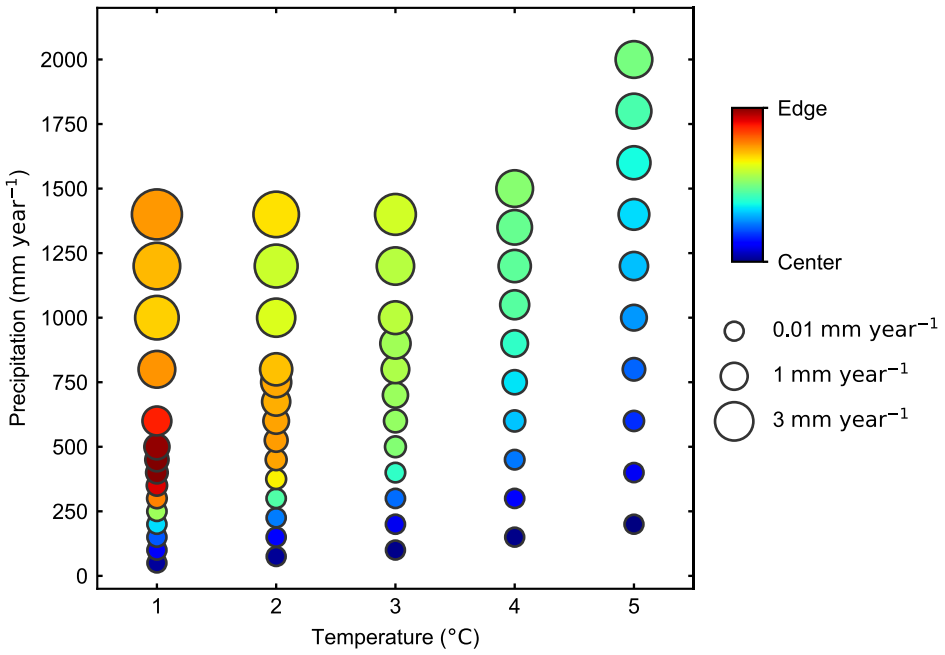

Figure 4.9 The rates and patterns of glacial erosion in different climatic settings. Horizontal and vertical axes indicate the mean annual temperature at sea-level and mean precipitation during the glacial maximum, respectively. The size of the cirque represents the mean erosion rates in glaciated region. The color scheme indicates the spatial patterns of glacial erosion. Red colors mean most erosion occurs near the edge of the mountains, and blue colors represent that glacial erosion focuses near the center of the mountain. The spatial patterns of glacial erosion are quantified by calculating the average values of glacial erosion weighted by the distance from the edge of the domain.

CHAPTER 5: GLACIATION INCREASES THE RELIEF OF MOUNTAIN RANGES: EVIDENCE FROM SPATIAL VARIATION IN GEOPHYSICAL RELIEF

Abstract

The topography of high mountain ranges is a result of the interactions between tectonics, climate, and surface processes. It has been proposed that repeated glaciations since the Late Cenozoic caused the uplift of mountain ranges by the isostatic response to glacial erosion. This hypothesis relies on glaciation increasing the relief of mountain belts. In this study, we compare the geophysical relief of 10 mountain ranges worldwide to assess the likelihood that glaciation causes increased relief. Mean normalized geophysical relief in glaciated mountain ranges is higher than the relief in non-glaciated mountain ranges by a factor of 2 to 4. We also calculate the geophysical relief for the whole Andes and document a trend of increasing normalized geophysical relief with latitude, and therefore, glaciation, in the southern Andes. Our analysis confirms a strong glacial imprint on the relief of mountain ranges. By assuming Airy isostasy, our estimation of relief increase yields an isostatic rebound of ~260 m for a mountain range with 4000-m orogen-scale relief. We suggest that this value is too small to have significant impact on mountain topography.

5.1 Introduction

The nature and strength of feedbacks between tectonics, climate, and surface processes are long-standing yet controversial questions in Earth science. It has been proposed that cold climate throughout the Late Cenozoic caused the uplift of mountain ranges through the isostatic response to increased valley incision by glacial erosion (Champagnac et al., 2007; Molnar and England, 1990). This hypothesis depends on glaciation causing increased relief in mountain ranges. However, there is debate as to whether glaciation has caused relief production or reduction in mountain ranges (van der Beek and Bourbon, 2008; Brocklehurst and Whipple, 2002; Valla et al., 2011; Whipple et al., 1999). Whether glaciation has caused an increase or decrease in relief depends on the relative efficiency of the relief-production and relief-reduction mechanisms. Glaciation increases relief by creating deep U-shaped valleys, and in extreme cases,

the bottoms of these valleys reach elevations below the sea-level, as evidenced by deep fjords along continental margins in high-latitude regions. However, glacial and periglacial processes can also reduce relief by focusing their erosion at high elevations and, therefore, lowering the summits of mountain ranges, i.e., the glacial buzzsaw hypothesis (Brozović et al., 1997; Egholm et al., 2009; Mitchell and Montgomery, 2006). Under this hypothesis, past glaciation caused relief reduction by removing high mountain peaks that protruded above the equilibrium line altitude (ELA) of glaciers. Whether glaciation has caused relief reduction or production during the Quaternary glaciations is still unclear. In this study, we quantify the relief structures in mountain ranges from a global perspective to address this question.

One way to quantify the relief structure of mountain ranges is to calculate the geophysical relief (Brocklehurst and Whipple, 2002; Small and Anderson, 1998). Geophysical relief is defined as the difference between the current topography and a reference surface that is related to the peaks and ridges in the mountain range. Previous studies have used geophysical relief or similar concepts to quantify the impact of glaciation on relief development in mountain ranges as well as the isostatic response to relief change (van der Beek and Bourbon, 2008; Brocklehurst et al., 2008; Champagnac et al., 2007, 2009). These studies, however, suggest contrasting influences of glaciation on relief. Observations of the European Alps suggest that glacial erosion might have increased the ridge-valley relief (van der Beek and Bourbon, 2008; Champagnac et al., 2007), and this finding is consistent with thermochronological data (Valla et al., 2011). On the contrary, Brocklehurst et al. (2008) suggest that measured relief is little affected by the degree of glacial modification in the western US.

As an attempt to provide a comprehensive quantification of the glacial impact on relief development, we calculate the geophysical relief for 10 selected mountain ranges worldwide using digital elevation models (DEMs). Our results reveal that the geophysical relief in glaciated mountain ranges is higher than non-glaciated mountain ranges. We also observe a significant increase in relief with latitude in the southern Andes. Our findings suggest that glacial processes increased the relief of mountain ranges at mid to high latitudes.

5.2 Methods

5.2.1 Geophysical relief

Geophysical relief is defined as the difference between the current topography and a smooth surface that connects the highest points in the landscape (Small and Anderson, 1998). If the landscape contains remnants of a previous topography at high elevations, then the smooth surfaces may approximate the former topography. Geophysical relief is, in this case, an estimation of the erosion in the landscape (Brocklehurst and Whipple, 2002; Steer et al., 2012). Although geophysical relief is not necessarily an estimation of erosion if the bounding surface does not represent the reconstruction of a past landscape, it is still a measure of the "missing mass" between summits and ridges within a mountain range that is responsible for the isostatic uplift of mountain peaks. There are two common methods for constructing the smooth surface that connects the high points. Brocklehurst and Whipple (2002) extract the ridgelines that outline a specific drainage basin and then interpolate a smooth surface between the ridgelines. They also test whether peaks and ridges within the basin sit above the interpolated surface and repeat the interpolation process to obtain a surface that also passes over these high points. This process is conducted iteratively until all points in the basin are below the interpolated surface. This method provides a reasonable surface that connects the high points in small drainage basins. In large drainage basins, however, this method will overestimate the geophysical relief because the interpolated surface neglects elevation variations within the basin. A more feasible approach for large drainage basins or landscapes is to record the highest point within a moving window that sliding across the whole landscape, and then to interpolate a surface connecting these highest points (Champagnac et al., 2007, 2012; Steer et al., 2012). Similarly, high points that protrude above this surface are also detected and the interpolation process is repeated to include these outliers.

In this study, we employ the second approach as it is better suited to the variable sizes of our study areas. The choice of the moving window size affects the resulting geophysical relief greatly. In general, a larger moving window results in a higher smooth surface and, therefore, larger geophysical relief values (Champagnac et al., 2012; Steer et al., 2012). Previous studies have suggested that a proper length scale of the moving window ranges from several kilometers to around 20 km (Champagnac et al., 2007; Steer et al., 2012). In this study, we use a circular moving window with a radius of 5 km. This value is comparable to typical spacings between

major valleys in most mountain ranges, and therefore, the measured geophysical relief represents the ridge-valley relief in mountain ranges.

We perform the calculation of geophysical relief for a group of 10 mountain ranges with a range of tectonic environments, climatic conditions, and properties of rock exposed at the surface (Table 5.1). We also calculate the geophysical relief for the Andes as a whole mountain belt to illustrate the variation of geophysical relief as a function of latitude. Furthermore, we also normalize the measured geophysical relief using the orogen-scale relief, defined as the difference between the 5^{th} percentile and the 95^{th} percentile of elevations, because mountain ranges with higher orogen-scale relief have the potential to create higher relief between ridges and valleys than mountains with lower orogen-scale relief. All the calculations are made using the ETOPO1 DEM (https://www.ngdc.noaa.gov/mgg/global/) with a resolution of 1′ (~1.8 km at the equator). ETOPO1 contains both land topography and ocean bathymetry.

5.2.2 Study areas

We select 10 mountain ranges spanning from low to high latitudes with various glaciation history (Table 5.1). We separate the 10 mountain ranges into two groups: glaciated mountain ranges and non-glaciated mountain ranges based on the degree to which the range was influenced by glaciation during the Quaternary (Ehlers et al., 2018). Among the 10 study areas, 4 of them are non-glaciated mountain ranges and the other 6 are glaciated mountain ranges (Table 5.1). In addition to these 10 study areas, we also calculate the geophysical relief for the whole Andes to investigate the latitudinal variation of geophysical relief.

5.3 Results

5.3.1 Glaciate vs. non-glaciated mountain ranges

We observe no noticeable difference in non-normalized geophysical relief between glaciated and non-glaciated landscapes (Fig. 5.1b). However, the normalized geophysical relief shows distinctive characteristics between non-glaciated and glaciated landscapes (Table 5.1; Figs. 5.1c, 5.2, and 5.3). The mean normalized geophysical relief is higher by a factor of 2 to 4 in glaciated mountain ranges than non-glaciated mountain ranges (Table 5.1), suggesting that glaciated landscapes have higher ridge/valley elevation variation than non-glaciated landscapes. In non-glaciated landscapes, the maximum values of normalized geophysical relief are less than

0.5 (Figs. 5.1c), indicating that the largest ridge-valley relief is about half of the orogen-scale relief in non-glaciated landscapes. In contrast, in glaciated landscapes, the highest normalized geophysical relief reaches values close to 1 (Figs. 5.1c), indicating that the depth of the deepest valleys is in the same order of magnitude as the orogen-scale relief in glaciated landscapes.

In addition to higher mean normalized geophysical relief, glaciated mountain ranges also feature different relief structures than non-glaciated mountain ranges. We calculate the mean elevations in a 5-km-radius moving window and then normalized them using the orogen-scale relief. By plotting this normalized mean elevation against the normalized geophysical relief, our results reveal distinct elevation-relief relationships between glaciated and non-glaciated landscapes. In non-glaciated mountain ranges, the normalized geophysical relief decreases gradually toward high elevations, and in the high elevation area with normalized elevations around 1, the normalized geophysical relief is low (Fig. 5.4a-d). In contrast, in glaciated mountain ranges, although the normalized geophysical relief also decreases slightly with increasing normalized elevation, the normalized geophysical relief at high elevation regions with normalized elevations around 1 still remains high (Fig. 5.4e-j).

5.3.2 Latitudinal variation in relief

We further analyze the topography of the Andes and investigate the latitudinal variation in geophysical relief. We perform the calculation of geophysical relief for the whole Andes (Fig. 5.5) and then analyze the topographic data for 2° latitude bins (Fig. 5.6). The non-normalized geophysical relief shows little variation across the Andes. In contrast, the normalized geophysical relief varies by a factor of 4 as a function of latitude in the Andes. The northern Andes have moderate values of normalized geophysical relief, while the lowest normalized relief is found in the central Andes (Fig. 5.6c and 5.6d). In the southern Andes, the normalized geophysical relief shows a strong increasing trend with latitude (Fig. 5.6c and 5.6d). Both the maximum and mean normalized geophysical relief start to increase at 34°S and reach the highest values at the southern tip of the Andes (Fig. 5.6c and 5.6d).

5.4 Discussion

5.4.1 Increased relief in glaciated mountain ranges

The elevation and relief of mountain ranges are strongly affected by tectonic environments. In active mountain ranges, rapid bedrock uplift creates high mountain ranges with great potential for creating high ridge-valley relief. By normalizing the measured geophysical relief using the orogen-scale relief of mountain ranges, we partially eliminate the influence of tectonics on relief. In our analysis, we observed higher values of normalized geophysical relief in glaciated mountain ranges than non-glaciated mountain ranges, suggesting that glacial processes are able to maintain higher ridge-valley relief than fluvial processes. If we assume that the pre-glacial topography of glaciated mountain ranges is similar to the present-day topography of non-glaciated mountain ranges, then our results suggest that glaciation could increase relief in mountain ranges. Furthermore, the increasing trend of normalized geophysical relief with latitude observed in the southern Andes also confirms a strong glacial impact on the relief of mountains, because presumably, the latitude is a first-order control on the intensity of glaciation (coverage, duration).

The mean normalized geophysical relief in non-glaciated landscapes varies from 0.036 to 0.080. If we assume a median value of 0.060, for a mountain range with orogen-scale relief of 4000 m, this is equivalent to a mean geophysical relief of 240 m (Table 5.2). Assuming Airy isostasy, the “missing mass” in valleys estimated based on the geophysical relief could cause 194 m isostatic uplift. For glaciated mountain ranges, the mean normalized geophysical relief is 0.119-0.166. Similar, taking the median value of 0.140 and assuming Airy isostasy, the expected isostatic uplift is 453 m in a mountain range with orogen-scale relief of 4000 m. If we assume that glaciated mountain ranges have similar relief structures with non-glaciated mountain ranges before the onset of glaciation, then our finding implies that glaciation leads to an isostatic uplift of 260 m for a mountain range with orogen-scale relief of 4000 m. This value is consistent with the estimated isostatic rebound due to Quaternary erosion in the western Alps using similar methods (van der Beek and Bourbon, 2008; Champagnac et al., 2007). If we assume that the increase in relief occurs gradually through the Quaternary, then the 260-meter isostatic rebound corresponds to an uplift rate of ~0.1 mm/year. This value is far less than typical uplift rates caused by tectonic activities. Furturemore, the isostatic uplift estimated by Airy isostaty is the upper limit of possible isostatic uplift induced by glaciation. Therefore, we suggest that the

contribution of glaciation-induced isostatic rebound to uplift is negligible in tectonically active mountain ranges.

5.4.2 Implication for erosion at high elevations

Changes in geophysical relief reflect the relative erosion efficiency at the bottom of valleys and along the ridges. Increased geophysical relief in glacial landscapes could result from enhanced erosion in valleys and/or reduced erosion along ridges. While the relative efficacy of glacial and fluvial erosion in shaping the topography of mountain ranges is still a controversial question (Koppes and Montgomery, 2009), it is commonly assumed that glacial erosion is more efficient in carving deep valleys than fluvial incision. Therefore, the key to interpreting the observed increase in geophysical relief is the erosion rate in high-altitude regions.

The glacial buzzsaw hypothesis suggests that glacial erosion and periglacial processes tend to remove preferential high elevation areas above the snowline, potentially limiting relief development in mountain ranges (Whipple et al., 1999). The lower summit elevations in the southern Andes than the northern and central Andes have been suggested to result from the glacial buzzsaw effect because of the correlation between peak elevations and ELAs in the southern Andes (Montgomery et al., 2001). Our analysis shows that glaciated mountain ranges have higher normalized geophysical relief than non-glaciated mountain ranges. This observation implies that, if a glacial buzzsaw exists, the lowering of valley bottoms must at least keep pace with the buzzsaw. The glacial buzzsaw hypothesis suggests that the erosion rates at high elevations must be higher than the bedrock uplift rate and consequently the erosion rates in valley bottoms must also be as high or even higher than the uplift rate. In this case, glacial erosion must be rapid across the entire topography, resulting in increased erosion rates in comparison with pre-glacial erosion rates.

An alternative view is that glaciers tend to protect ridges and peaks from erosion through cold-based conditions (Stern et al., 2005; Thomson et al., 2010). Cold-based glaciers are frozen to their beds and cause little erosion due to limited basal sliding and meltwater supply. Numerical simulations suggest that cold-based conditions are common in high elevations in cold climates (Lai and Anders, 2020; Yanites and Ehlers, 2012). Such glacial protection of ridges could lead to increased relief in glacial landscapes. Stern et al. (2005) suggest that the differential erosion efficiency between cold-based ice caps at high elevations and warm-based valley glaciers

might have caused the high relief observed in the Transantarctic Mountains. In the southern Andes, low exhumation rates observed in the region south of 50°S suggests that southernmost of the Andes might have been protected by cold-based ice from erosion (Thomson et al., 2010). This mechanism does not require that glacial erosion operates at very high rates in the valleys, which could lead to similar erosion rates to pre-glacial erosion rates in the mountain range.

In summary, our analysis of geophysical relief suggests that glaciation increases the ridge-valley relief in mountain ranges. If the erosion rates of summits and ridges are rapid, as suggested by the glacial buzzsaw hypothesis, the average erosion rate of the mountain range will be higher than the pre-glacial erosion rate. On the other hand, if the high topography is protected from erosion by cold-based ice during glaciation, then the increased normalized geophysical relief is a result of the slow erosion of ridges and the rapid incision of valleys, and the increasing volume of "missing mass" between ridges does not represent an increase in the average erosion rates. Whether average erosion rates of mountain ranges have increased due to climate change or have been relatively constant during the past several million years is still in debate (Ganti et al., 2016; Herman et al., 2013; Koppes and Montgomery, 2009; Schildgen et al., 2018; Willenbring and von Blanckenburg, 2010; Zhang et al., 2001). Our results provide an additional piece of evidence for this important yet controversial question.

5.4.3 Limitations and future directions

One major limitation of our analysis arises from the resolution of the digital elevation model. Our analysis is made using the ETOPO1 DEM with a resolution of 1′. We choose to use this DEM because it has a small data size allowing for quick processing and it contains the bathymetry along glaciated continental margins, which is necessary for calculating the geophysical relief in fjords. However, the low-resolution DEM contains less topographic information than DEMs with higher resolutions. Therefore, the estimation of geophysical relief using ETOPO1 is unable to resolve the detailed spatial patterns of geophysical relief. Furthermore, the size of the moving window also influences the measured geophysical relief. The geophysical relief calculated using a larger window reflects the relief on a larger length scale than a smaller window (Champagnac et al., 2012). Our choice of window size is limited by the resolution of the DEM. For future work, we will estimate the geophysical relief using a DEM with higher resolution. We will compare the geophysical relief between glaciated and non-

glaciated landscapes using a wide range of moving window size. This will provide a more comprehensive understanding of the difference in relief structure at various scales between glaciated and non-glaciated mountain ranges.

Another limitation of our analysis is that the ETOPO1 DEM shows the ice surface elevation ratier than bedrock elevation where glaciers still exist. Therefore, the geophysical relief is underestimated because the DEM shows the elvation of ice surface rather than bedrock in glaciated valleys. For example, in southern parts of the Patagonia Andes, our estimation of geophysical relief is lower than acutal values because of the Southern Pataginian Ice Field. For future work, we will investigate the influence of modern glaciers on our estimation of geophysical relief.

5.5 Conclusion

We show that the normalized geophysical relief in glaciated mountain ranges is higher than non-glaciated mountain ranges by a factor of 2 to 4, which suggests that glaciation increases the relief of mountain ranges. If we assume that in glaciated mountain ranges, the pre-glacial relief is similar to the relief in non-glaciated mountains, then the isostatic response to increased relief reaches values up to ~400 m in a mountain range with orogen-scale relief of 4000 m. Furthermore, we observe a trend of increasing normalized geophysical relief with latitude in the southern Andes. This finding also suggests that glaciation enhanced relief in mountain ranges.

5.6 Figures and tables

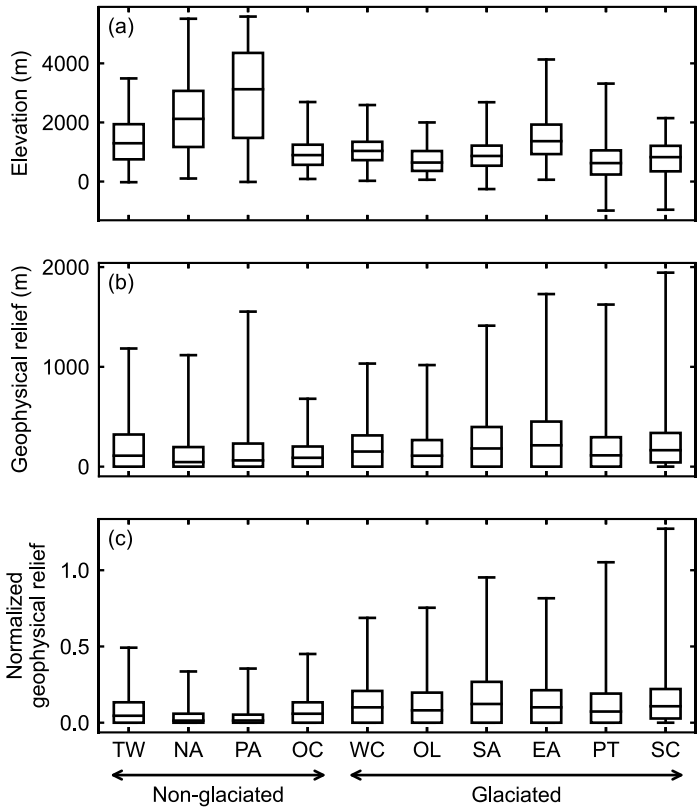

Figure 5.1 Box plots of elevation (a), geophysical relief (b), and normalized geophysical relief (c) of 10 selected mountain ranges. The abbreviations of mountain ranges are listed in Table 5.1. The box extends from the lower to the upper quartile values of the data, with a horizontal line at the median. The whiskers represent the full range of the data.

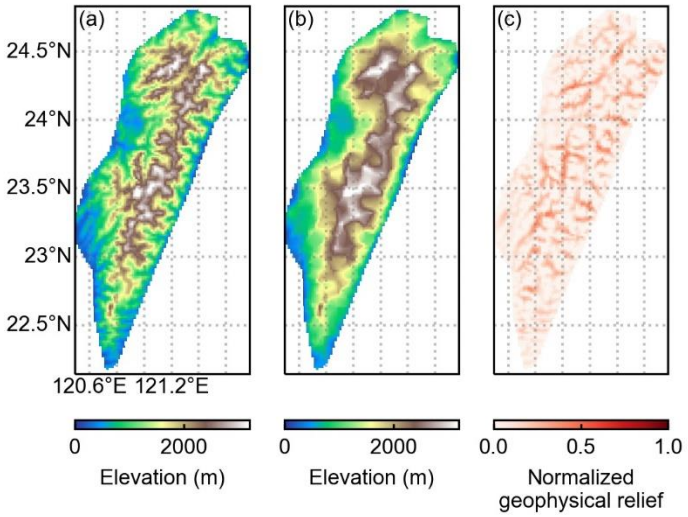

Figure 5.2 Topography (a), the surface that connects high points (b), and normalized geophysical relief (c) of Taiwan.

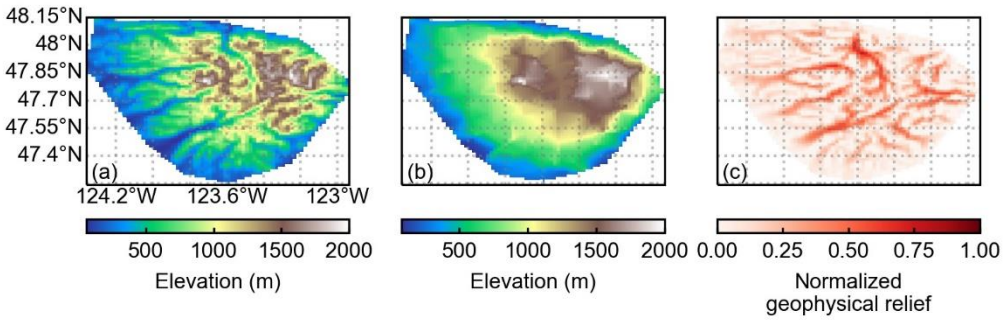

Figure 5.3 Topography (a), the surface that connects high points (b), and normalized geophysical relief (c) of the Olympics.

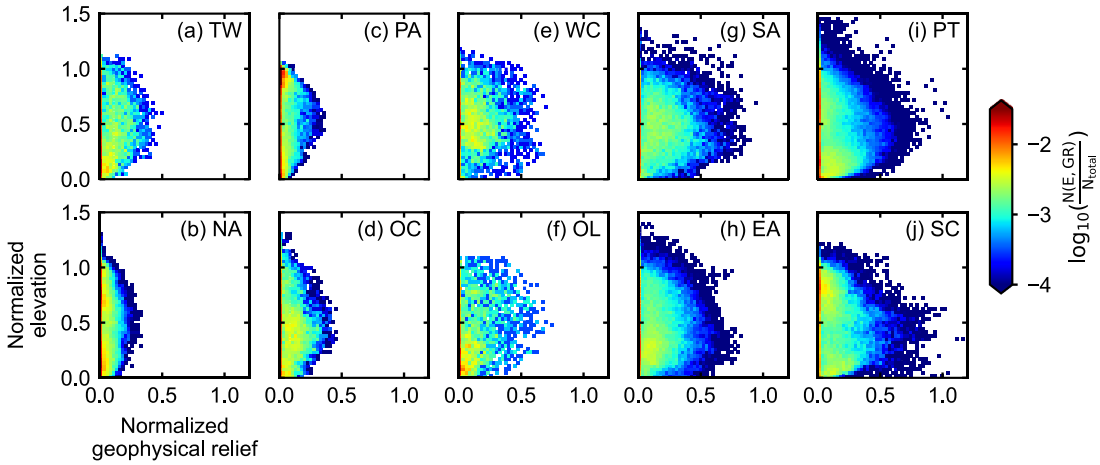

Figure 5.4 Relief structures in mountain ranges. Vertical axes are mean elevations in 5-km-radius moving windows normalized by the the orogen-scale relief. Horizontal axes are normalized geophysical relief. Color scheme represents the fraction of pixels at a given elevation and relief. Note the logarithmic color scale.

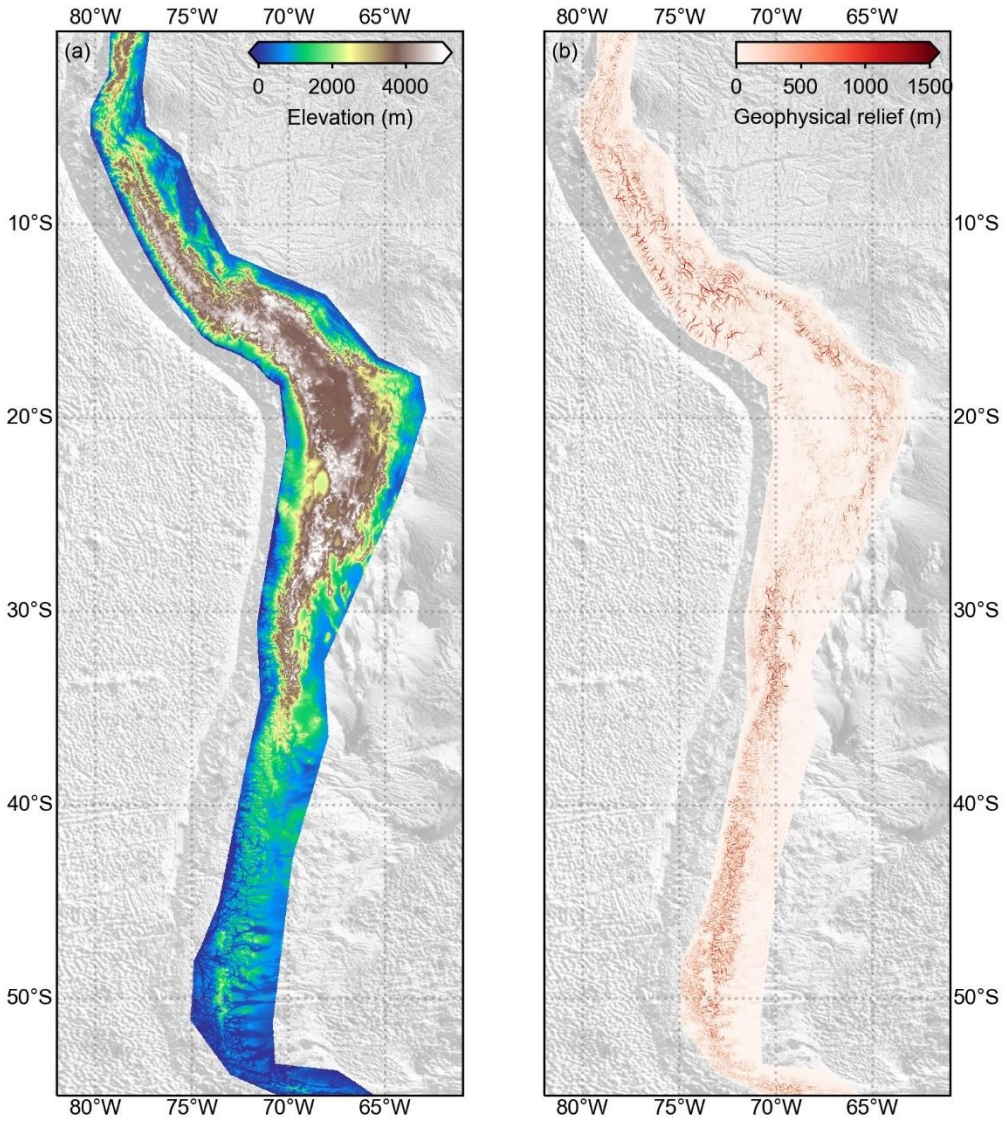

Figure 5.5 Topography (a) and geophysical relief (b) of the Andes.

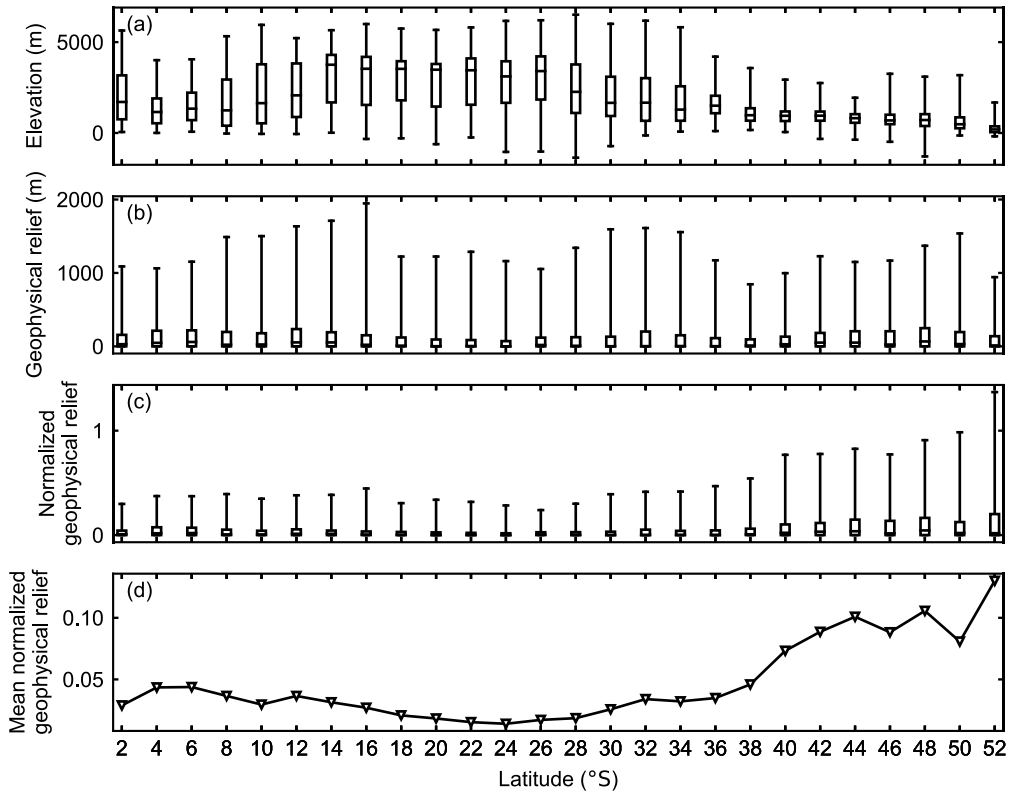

Figure 5.6 Box plots of elevation (a), geophysical relief (b), and normalized geophysical relief (c) for 2° latitude bins. The normalized geophysical relief is normalized using the orogen-scale relief in each bin. Panel (d) is the mean normalized geophysical relief in 2° latitude bins.

Table 5.1 Mean geophysical relief (GR_{mean}), max geophysical relief (GR_{max}), and mean normalized geophysical relief (NGR_{mean}) of 10 mountain ranges.

Mountain ranges	Abbreviation	GR_{mean} (m)	GR_{max} (m)	NGR_{mean}
Non-glaciated				
Taiwan	TW	191	3490	0.079
Northern Andes	NA	121	5510	0.036
Peruvian Andes	PA	162	5583	0.037
Oregon Cascades	OC	122	2691	0.080
Glaciated				
Washington Cascades	WC	201	2589	0.134
Olympics	OL	170	2000	0.127
Southern Alps	SA	245	2684	0.166
European Alps	EA	286	4131	0.135
Patagonia Andes	PT	184	3315	0.119
Scandinavia	SC	228	2146	0.149

Table 5.2 Geophysical relief and isostatic uplift for a mountain range with 4000-m orogen-scale relief. For calculation of isostatic uplift, we assume that the density of crust is 2700 kg m^{-3} and the density of mantle is 3300 kg m^{-3}.

	NGR_{mean}	GR_{mean} (m)	Isostatic uplift (m)
Non-glaciated	0.06	240	194
Glaciated	0.14	560	453

CHAPTER 6: CONCLUSIONS AND FUTURE DIRECTIONS

6.1 Conclusions

My research provides constraints on the interactions between tectonics, climate, and surface processes in glacial and postglacial landscapes. My primary method is developing numerical models to simulate the evolution of topography with different surface processes and the response of surface topography to tectonic and climatic forcing. I develop modeling components based on the Landlab modeling framework to simulate the hydrological connections in low-relief postglacial landscapes. I also build a glacial landscape evolution model by combining a sliding-based glacial erosion model with a thermodynamically coupled ice sheet model. In addition to numerical modeling, I use digital elevation models to quantify the impact of glaciation on topography. The main conclusions of my research are summarized as follows.

(1) In low-relief postglacial landscapes with local depressions that are isolated from the drainage network, numerical simulations show that the hydrological connections between these isolated depressions and external drainage networks via filling and spilling could accelerate the expansion of fluvial networks and produce distinctive channel morphology in comparison with cases in which the depressions remain hydrologically isolated. Comparison between modeled landscapes and the topography of glaciated US Midwest suggesting the hydrological connection between depressions and drainage networks have been an important control on the development of topography in postglacial US Midwest.

(2) In alpine glacial landscapes, numerical simulations reveal a strong trend of increasing glacial erosion with increasing geothermal heat flux. High values of geothermal heat flux could lead to large areas with warm-based conditions in alpine glaciers and expand the warm-based areas into high elevations. As a result, glaciers with higher geothermal heat flux contain a larger area of significant erosion than glaciers with lower geothermal heat flux. Meanwhile, high geothermal heat flux could promote basal sliding by increasing the production of meltwater and therefore, increase the rate of erosion. This finding suggests a novel linkage between tectonics and surface processes via the dependency of glacial erosion on geothermal heat flux.

(3) Climate controls the spatial patterns of glacial erosion in mountain ranges by modulating the basal thermal regimes of mountain glaciers. Cold temperature leads to small warm-based areas confined in major valleys, while a warm climate expands the warm-based area into high elevations. As a result, glacial erosion tends to focus on lower elevations in a cold climate than in a warm climate. Increasing precipitation has the potential to increase the warm-based area because high precipitation rates favor thick ice, lowering the melting point of ice at the base of glaciers. High precipitation rates, therefore, tend to expand the warm-based area into high elevations, resulting in intensive erosion near the peak of the mountain range. Importantly, there might not be any direct spatial correlation between glacial erosion patterns and the equilibrium line altitudes (ELA) of glaciers, because different climatic conditions could produce glaciers with similar ELAs but distinctive patterns of glacial erosion.

(4) Measuring the geophysical relief of mountain ranges provides an opportunity to quantify the impact of glaciation on the relief of mountain ranges. Comparison of geophysical relief normalized by orogen-scale relief in 10 mountain ranges worldwide shows that the normalized geophysical relief in glaciated mountain ranges is higher than the normalized relief in non-glaciated mountain ranges by a factor of 2 to 4. Furthermore, the results show a trend of increasing normalized geophysical relief with latitude (hence glaciation) in the southern Andes. These observations suggest that glaciation might have increased the relief in mountain ranges.

6.2 Future directions

6.2.1 Improving glacial landscape evolution modeling framework

Although my work has greatly improved glacial landscape evolution models by incorporating state-of-the-art ice dynamics models into landscape evolution modeling, fundamental shortcomings still exist in the current modeling framework and limit our understanding of glacial landscape evolution. In particular, current models lack proper approximation of deposition below glacial ice. Subglacial sediments may act as tools for glacial abrasion (Ugelvig and Egholm, 2018), and may also trigger stabilizing feedbacks that protect bedrock from erosion (Alley et al., 2003). Therefore, a proper representation of subglacial

sedimentation is necessary for a better understanding of the interactions between subglacial sediments and glacial erosion as well as their impacts on landscape evolution.

The ice dynamics models in most glacial landscape evolution modeling frameworks are adopted from ice sheet models. Therefore, they often neglect the influence of steep topography. Specifically, the snow avalanche process is commonly neglected in glacial landscape evolution models, resulting in that steep mountain peaks and ridges are perennially covered by ice. However, in actual glacial topography, these peaks and ridges are only covered by thin layers of snow due to frequent avalanches. As a result, the dominant erosional process for these steep landforms is paraglacial hillslope processes rather than glacial erosion (Scherler and Egholm, 2020). The lack of representation for snow avalanching and paraglacial hillslope processes could lead to unreasonably high elevations in glacial landscape evolution models if the steep summits and ridges are covered by cold-based ice. In order to provide better constraints on the evolution of steep topography in glaciated mountainous regions, the landscape evolution models must include approximation for snow avalanche and paraglacial hillslope processes.

6.2.2 Response timescales in glacial and postglacial landscapes

The feedbacks between surface processes and topography drive the landscapes toward a steady-state configuration in which the rate of erosion equals the rate of uplift. Therefore, in steady-state landscapes, long-term erosion rates are ultimately controlled by tectonics. However, over short timescales, climate perturbations could induce a transient response in steady-state landscapes. The timescale over which these transient conditions persist is a crucial control on the response of landscapes to climatic perturbations. For instance, the repeated glacial/interglacial cycles have caused frequent climate perturbations since the Late Cenozoic. If the response time of surface landscapes to glaciations is longer than the periods of glacial/interglacial cycles, then glaciations may have a significant and prolonged impact on landscape evolution. My research on the evolution of low-relief postglacial landscape (Chapter 2) shows that continental glaciation may have a prolonged impact on postglacial landscapes for tens of thousands of years, a timescale that is comparable with typical glacial/interglacial cycles. Furthermore, my work on glacial erosion in mountain ranges suggests that the rate of erosion varies by two orders of magnitude depending on tectonic and climatic conditions (Chapters 3 and 4). The highly variable erosion rates of alpine glaciers imply that the response timescale of glacial erosion is also highly

variable and dependent on specific tectonic and climatic settings. Specifically, the dependency of response timescales on climate suggests that some climatic perturbations may have a more profound impact on landscape evolution than others. Therefore, a full understanding of the influence of climate on topography requires knowledge of how the response timescales in glacial and postglacial landscapes depend on climatic conditions.

REFERENCES

Alley, R. B., Lawson, D. E., Larson, G. J., Evenson, E. B. and Baker, G. S.: Stabilizing feedbacks in glacier-bed erosion, Nature, 424(6950), 758–760, doi:10.1038/nature01839, 2003.

Anders, A. M., Roe, G. H., Montgomery, D. R. and Hallet, B.: Influence of precipitation phase on the form of mountain ranges, Geology, 36(6), 479, doi:10.1130/G24821A.1, 2008.

Anders, A. M., Mitchell, S. G. and Tomkin, J. H.: Cirques, peaks, and precipitation patterns in the Swiss Alps: Connections among climate, glacial erosion, and topography, Geology, 38(3), 239–242, doi:10.1130/G30691.1, 2010.

Anderson, R. S., Molnar, P. and Kessler, M. A.: Features of glacial valley profiles simply explained, Journal of Geophysical Research, 111(F1), F01004, doi:10.1029/2005JF000344, 2006.

Aschwanden, A., Bueler, E., Khroulev, C. and Blatter, H.: An enthalpy formulation for glaciers and ice sheets, Journal of Glaciology, 58(209), 441–457, doi:10.3189/2012JoG11J088, 2012.

Aschwanden, A., Fahnestock, M. A. and Truffer, M.: Complex Greenland outlet glacier flow captured, Nature Communications, 7(May 2015), 1–8, doi:10.1038/ncomms10524, 2016.

Atkinson, L. A., Ross, M. and Stumpf, A. J.: Three-dimensional hydrofacies assemblages in ice-contact/proximal sediments forming a heterogeneous ‘hybrid’ hydrostratigraphic unit in central Illinois, USA, Hydrogeology Journal, 22(7), 1605–1624, doi:10.1007/s10040-014-1156-7, 2014.

Barnes, R., Lehman, C. and Mulla, D.: An efficient assignment of drainage direction over flat surfaces in raster digital elevation models, Computers and Geosciences, 62, 128–135, doi:10.1016/j.cageo.2013.01.009, 2014a.

Barnes, R., Lehman, C. and Mulla, D.: Priority-flood: An optimal depression-filling and watershed-labeling algorithm for digital elevation models, Computers and Geosciences, 62, 117–127, doi:10.1016/j.cageo.2013.04.024, 2014b.

Barr, I. D. and Spagnolo, M.: Glacial cirques as palaeoenvironmental indicators: Their potential and limitations, Earth-Science Reviews, 151, 48–78, doi:10.1016/j.earscirev.2015.10.004, 2015.

Bartlein, P. J., Webb, T. and Fleri, E.: Holocene Climatic Change in the Northern Midwest: Pollen-Derived Estimates, Quaternary Research, 22(03), 361–374, doi:10.1016/0033-5894(84)90029-2, 1984.

Batt, G. E., Brandon, M. T., Farley, K. A. and Roden-Tice, M.: Tectonic synthesis of the Olympic Mountains segment of the Cascadia wedge, using two-dimensional thermal and kinematic modeling of thermochronological ages, Journal of Geophysical Research: Solid Earth, 106(B11), 26731–26746, doi:10.1029/2001JB000288, 2001.

Beaud, F., Flowers, G. E. and Pimentel, S.: Seasonal-scale abrasion and quarrying patterns from a two-dimensional ice-flow model coupled to distributed and channelized subglacial drainage, Geomorphology, 219, 176–191, doi:10.1016/j.geomorph.2014.04.036, 2014.

Beaud, F., Flowers, G. E. and Venditti, J. G.: Efficacy of bedrock erosion by subglacial water flow, Earth Surface Dynamics, 4(1), 125–145, doi:10.5194/esurf-4-125-2016, 2016.

van der Beek, P. and Bourbon, P.: A quantification of the glacial imprint on relief development in the French western Alps, Geomorphology, 97(1–2), 52–72, doi:10.1016/j.geomorph.2007.02.038, 2008.

Belmont, P., Gran, K. B., Schottler, S. P., Wilcock, P. R., Day, S. S., Jennings, C., Lauer, J. W., Viparelli, E., Willenbring, J. K., Engstrom, D. R. and Parker, G.: Large Shift in Source of Fine Sediment in the Upper Mississippi River, Environmental Science & Technology, 45(20), 8804–8810, doi:10.1021/es2019109, 2011.

Bettis, E. A., Muhs, D. R., Roberts, H. M. and Ann G: Last Glacial loess in the conterminous USA, Quaternary Science Reviews, 22(18–19), 1907–1946, doi:10.1016/S0277-3791(03)00169-0, 2003.

Boulton, G. S. and Paul, M. A.: The influence of genetic processes on some geotechnical properties of glacial tills, Quarterly Journal of Engineering Geology and Hydrogeology, 9(3), 159–194, doi:10.1144/GSL.QJEG.1976.009.03.03, 1976.

Braun, J.: Pecube: a new finite-element code to solve the 3D heat transport equation including the effects of a time-varying, finite amplitude surface topography, Computers & Geosciences, 29(6), 787–794, doi:10.1016/S0098-3004(03)00052-9, 2003.

Braun, J. and Willett, S. D.: A very efficient O(n), implicit and parallel method to solve the stream power equation governing fluvial incision and landscape evolution, Geomorphology, 180–181, 170–179, doi:10.1016/j.geomorph.2012.10.008, 2013.

Braun, J., Zwartz, D. and Tomkin, J. H.: A new surface-processes model combining glacial and fluvial erosion, Annals of Glaciology, 28, 282–290, doi:10.3189/172756499781821797, 1999.

Braun, J., van der Beek, P. and Batt, G.: Quantitative Thermochronology, Cambridge University Press, Cambridge., 2006.

Brocklehurst, S. H. and Whipple, K. X.: Glacial erosion and relief production in the Eastern Sierra Nevada, California, Geomorphology, 42(1–2), 1–24, doi:10.1016/S0169-555X(01)00069-1, 2002.

Brocklehurst, S. H., Whipple, K. X. and Foster, D.: Ice thickness and topographic relief in glaciated landscapes of the western USA, Geomorphology, 97(1–2), 35–51, doi:10.1016/j.geomorph.2007.02.037, 2008.

Brown, D. G., Lusch, D. P. and Duda, K. a.: Supervised classification of types of glaciated landscapes using digital elevation data, Geomorphology, 21(3–4), 233–250, doi:10.1016/S0169-555X(97)00063-9, 1998.

Brown, R. W., Summerfield, M. A. and Gleadow, A. J. W.: Denudational history along a transect across the Drakensberg Escarpment of southern Africa derived from apatite fission track thermochronology, Journal of Geophysical Research: Solid Earth, 107(B12), ETG 10-1-ETG 10-18, doi:10.1029/2001JB000745, 2002.

Brozović, N., Burbank, D. W. and Meigs, A. J.: Climatic limits on landscape development in the Northwestern Himalaya, Science, 276(5312), 571–574, doi:10.1126/science.276.5312.571, 1997.

Bueler, E. and Brown, J.: Shallow shelf approximation as a “sliding law” in a thermomechanically coupled ice sheet model, Journal of Geophysical Research: Solid Earth, 114(3), 1–21, doi:10.1029/2008JF001179, 2009.

Bueler, E. and van Pelt, W.: Mass-conserving subglacial hydrology in the Parallel Ice Sheet Model version 0.6, Geoscientific Model Development, 8(6), 1613–1635, doi:10.5194/gmd-8-1613-2015, 2015.

Calov, R. and Greve, R.: A semi-analytical solution for the positive degree-day model with stochastic temperature variations, Journal of Glaciology, 51(172), 173–175, doi:10.3189/172756505781829601, 2005.

Champagnac, J. D., Molnar, P., Anderson, R. S., Sue, C. and Delacou, B.: Quaternary erosion-induced isostatic rebound in the western Alps, Geology, 35(3), 195, doi:10.1130/G23053A.1, 2007.

Champagnac, J. D., Schlunegger, F., Norton, K., von Blanckenburg, F., Abbühl, L. M. and Schwab, M.: Erosion-driven uplift of the modern Central Alps, Tectonophysics, 474(1–2), 236–249, doi:10.1016/j.tecto.2009.02.024, 2009.

Champagnac, J. D., Molnar, P., Sue, C. and Herman, F.: Tectonics, climate, and mountain topography, Journal of Geophysical Research: Solid Earth, 117(2), doi:10.1029/2011JB008348, 2012.

Chow, T. L., Rees, H. W. and Daigle, J. L.: Effectiveness of terraces/grassed waterway systems for soil and water conservation: A field evaluation, Journal of Soil and Water conservation, 54(3), 577–583, 1999.

Colberg, J. S. and Anders, A. M.: Numerical modeling of spatially-variable precipitation and passive margin escarpment evolution, Geomorphology, 207, 203–212, doi:10.1016/j.geomorph.2013.11.006, 2014.

Colgan, P. M., Mickelson, D. M. and Cutler, P. M.: Ice-marginal terrestrial landsystems: southern Laurentide Ice Sheet margin, in Glacial landsystems. London: Arnold, pp. 111–142., 2003.

Currie, C. A. and Hyndman, R. D.: The thermal structure of subduction zone back arcs, Journal of Geophysical Research, 111(B8), B08404, doi:10.1029/2005JB004024, 2006.

Curry, B. B., Grimley, D. A. and McKay, E. D.: Quaternary Glaciations in Illinois, in Developments in Quaternary Sciences, vol. Volume 15, pp. 467–487, Elsevier Amsterdam, The Netherlands., 2011.

D'Alpaos, A., Lanzoni, S., Marani, M., Fagherazzi, S. and Rinaldo, A.: Tidal network ontogeny: Channel initiation and early development, Journal of Geophysical Research: Earth Surface, 110(2), 1–14, doi:10.1029/2004JF000182, 2005.

Dadson, S. J. and Church, M.: Postglacial topographic evolution of glaciated valleys: A stochastic landscape evolution model, Earth Surface Processes and Landforms, 30(11), 1387–1403, doi:10.1002/esp.1199, 2005.

Dadson, S. J., Hovius, N., Chen, H., Dade, W. B., Hsieh, M.-L., Willett, S. D., Hu, J.-C., Horng, M.-J., Chen, M.-C., Stark, C. P., Lague, D. and Lin, J.-C.: Links between erosion, runoff variability and seismicity in the Taiwan orogen, Nature, 426(6967), 648–651, doi:10.1038/nature02150, 2003.

Davies, J. H.: Global map of solid Earth surface heat flow, Geochemistry, Geophysics, Geosystems, 14(10), 4608–4622, doi:10.1002/ggge.20271, 2013.

Dickinson, W. T. and Whiteley, H.: Watershed areas contributing to runoff, IAHS publ, 96, 12–26, 1970.

Dühnforth, M., Anderson, R. S., Ward, D. and Stock, G. M.: Bedrock fracture control of glacial erosion processes and rates, Geology, 38(5), 423–426, doi:10.1130/G30576.1, 2010.

Dunne, T.: Formation and controls of channel networks, Progress in Physical Geography, 4(2), 211–239, doi:10.1177/030913338000400204, 1980.

Egholm, D. L., Nielsen, S. B., Pedersen, V. K. and Lesemann, J.-E.: Glacial effects limiting mountain height, Nature, 460(13), 884–887, doi:10.1038/nature08263, 2009.

Egholm, D. L., Knudsen, M. F., Clark, C. D. and Lesemann, J. E.: Modeling the flow of glaciers in steep terrains: The integrated second-order shallow ice approximation (iSOSIA), Journal of Geophysical Research: Earth Surface, 116(2), 1–16, doi:10.1029/2010JF001900, 2011.

Ehlers, J., Gibbard, P. L. and Hughes, P. D.: Quaternary Glaciations and Chronology, in Past Glacial Environments, pp. 77–101, Elsevier., 2018.

Fahnestock, M., Abdalati, W., Joughin, I., Brozena, J. and Gogineni, P.: High Geothermal Heat Flow, Basal Melt, and the Origin of Rapid Ice Flow in Central Greenland, Science, 294(5550), 2338–2342, doi:10.1126/science.1065370, 2001.

Fenneman, N. M. and Johnson, D. W.: Physiographic divisions of the conterminous US, 1946.

Ferrier, K. L., Huppert, K. L. and Perron, J. T.: Climatic control of bedrock river incision, Nature, 496(7444), 206–209, doi:10.1038/nature11982, 2013.

Flowers, G. E.: Modelling water flow under glaciers and ice sheets, Proceedings of the Royal Society A: Mathematical, Physical and Engineering Sciences, 471(2176), 20140907–20140907, doi:10.1098/rspa.2014.0907, 2015.

Foster, G. L. and Vance, D.: Negligible glacial–interglacial variation in continental chemical weathering rates, Nature, 444(7121), 918–921, doi:10.1038/nature05365, 2006.

Fullerton, D. S., Bush, C. A. and Pennell, J. N.: Map of Surficial Deposits and Materials in the Eastern and Central United States (East of 102° West Longitude), 2003.

Ganti, V., Hagke, C. Von, Scherler, D., Lamb, M. P., Fischer, W. W. and Avouac, J.: Time scale bias in erosion rates of glaciated landscapes, Science Advances, 2, doi:10.1126/sciadv.1600204, 2016.

Gasparini, N. M., Whipple, K. X. and Bras, R. L.: Predictions of steady state and transient landscape morphology using sediment-flux-dependent river incision models, Journal of Geophysical Research: Earth Surface, 112(3), 1–20, doi:10.1029/2006JF000567, 2007.

Golledge, N. R., Mackintosh, A. N., Anderson, B. M., Buckley, K. M., Doughty, A. M., Barrell, D. J. A., Denton, G. H., Vandergoes, M. J., Andersen, B. G. and Schaefer, J. M.: Last Glacial Maximum climate in New Zealand inferred from a modelled Southern Alps icefield, Quaternary Science Reviews, 46, 30–45, doi:10.1016/j.quascirev.2012.05.004, 2012.

Goutorbe, B., Poort, J., Lucazeau, F. and Raillard, S.: Global heat flow trends resolved from multiple geological and geophysical proxies, Geophysical Journal International, 187(3), 1405–1419, doi:10.1111/j.1365-246X.2011.05228.x, 2011.

Gran, K. B., Finnegan, N., Johnson, A. L., Belmont, P., Wittkop, C. and Rittenour, T.: Landscape evolution, valley excavation, and terrace development following abrupt postglacial base-level fall, Bulletin of the Geological Society of America, 125(11–12), 1851–1864, doi:10.1130/B30772.1, 2013.

Grimley, D. A., Anders, A. M. and Stumpf, A. J.: Quaternary Geology of the Upper Sangamon River Basin: Glacial, Postglacial, and Postsettlement History, in 1967–2016—Celebrating 50 Years of Geoscience in the Mid-Continent: Guidebook for the 50th Annual Meeting of the Geological Society of America–North-Central Section, Guidebook 43, edited by Z. Lasemi and S. Elrick, pp. 55–96, Illinois State Geological Survey, Prairie Research Institute, Champaign, Illinois., 2016a.

Grimley, D. A., Wang, J. J. and Oien, R. P.: Surficial Geology of Mahomet Quadrangle, Champaign and Piatt Counties, Illinois, , 13, 2016b.

Hajic, E. R.: Late Pleistocene and Holocene landscape evolution, depositional subsystems, and stratigraphy in the lower Illinois River Valley and adjacent central Mississippi River Valley, PhD Thesis, University of Illinois at Urbana-Champaign., 1990.

Hall, A. M., Ebert, K., Kleman, J., Nesje, A. and Ottesen, D.: Selective glacial erosion on the Norwegian passive margin, Geology, 41(12), 1203–1206, doi:10.1130/G34806.1, 2013.

Hallet, B.: A Theoretical Model of Glacial Abrasion, Journal of Glaciology, 23(89), 39–50, doi:10.1017/S0022143000029725, 1979.

Hallet, B.: Glacial quarrying: a simple theoretical model, Annals of Glaciology, 22, 1–8, doi:10.3189/1996AoG22-1-1-8, 1996.

Hamza, V. M., Dias, F. J. S. S., Gomes, A. J. L. and Terceros, Z. G. D.: Numerical and functional representations of regional heat flow in South America, Physics of the Earth and Planetary Interiors, 152(4), 223–256, doi:10.1016/j.pepi.2005.04.009, 2005.

Han, J., Gasparini, N. M. and Johnson, J. P. L.: Measuring the imprint of orographic rainfall gradients on the morphology of steady-state numerical fluvial landscapes, Earth Surface Processes and Landforms, 40(10), 1334–1350, doi:10.1002/esp.3723, 2015.

Hanson, G. J.: Development of a jet index to characterize erosion resistance of soils in earthen spillways, Transactions of the ASAE, 34(5), 2015–2020, doi:10.13031/2013.31831, 1991.

Heimsath, A. M., Chappell, J., Dietrich, W. E., Nishiizumi, K. and Finkel, R. C.: Soil production on a retreating escarpment in southeastern Australia, Geology, 28(9), 787, doi:10.1130/0091-7613(2000)28<787:SPOARE>2.0.CO;2, 2000.

Herman, F. and Brandon, M.: Mid-latitude glacial erosion hotspot related to equatorial shifts in southern Westerlies, Geology, 43(11), 987–990, doi:10.1130/G37008.1, 2015.

Herman, F. and Braun, J.: Evolution of the glacial landscape of the Southern Alps of New Zealand: Insights from a glacial erosion model, Journal of Geophysical Research: Earth Surface, 113(2), doi:10.1029/2007JF000807, 2008.

Herman, F., Beaud, F., Champagnac, J. D., Lemieux, J. M. and Sternai, P.: Glacial hydrology and erosion patterns: A mechanism for carving glacial valleys, Earth and Planetary Science Letters, 310(3–4), 498–508, doi:10.1016/j.epsl.2011.08.022, 2011.

Herman, F., Seward, D., Valla, P. G., Carter, A., Kohn, B., Willett, S. D. and Ehlers, T. a.: Worldwide acceleration of mountain erosion under a cooling climate, Nature, 504(7480), 423–426, doi:10.1038/nature12877, 2013.

Herman, F., Beyssac, O., Brughelli, M., Lane, S. N., Leprince, S., Adatte, T., Lin, J. Y. Y., Avouac, J.-P. and Cox, S. C.: Erosion by an Alpine glacier, Science, 350(6257), 193–195, doi:10.1126/science.aab2386, 2015.

Hindmarsh, R. C. A.: The role of membrane-like stresses in determining the stability and sensitivity of the Antarctic ice sheets: back pressure and grounding line motion, Philosophical Transactions of the Royal Society A: Mathematical, Physical and Engineering Sciences, 364(1844), 1733–1767, doi:10.1098/rsta.2006.1797, 2006.

Hobley, D. E. J., Adams, J. M., Nudurupati, S. S., Hutton, E. W. H., Gasparini, N. M., Istanbulluoglu, E. and Tucker, G. E.: Creative computing with Landlab: an open-source toolkit for building, coupling, and exploring two-dimensional numerical models of Earth-surface dynamics, Earth Surface Dynamics, 5(1), 21–46, doi:10.5194/esurf-5-21-2017, 2017.

Howard, A. D.: A detachment limited model of drainage basin evolution, Water Resources Research, 30(7), 2261–2285, doi:10.1029/94WR00757, 1994.

Humphrey, N. F. and Raymond, C. F.: Hydrology, erosion and sediment production in a surging glacier: Variegated Glacier, Alaska, 1982–83, Journal of Glaciology, 40(136), 539–552, doi:https://doi.org/10.3189/S0022143000012429, 1994.

Hutter, K.: Theoretical Glaciology, D. Reidel Publishing Company, Dordrecht, Netherlands., 1983.

Huybrechts, P.: Sea-level changes at the LGM from ice-dynamic reconstructions of the Greenland and Antarctic ice sheets during the glacial cycles, Quaternary Science Reviews, 21(1–3), 203–231, doi:10.1016/S0277-3791(01)00082-8, 2002.

Iken, A.: The Effect of the Subglacial Water Pressure on the Sliding Velocity of a Glacier in an Idealized Numerical Model, Journal of Glaciology, 27(97), 407–421, doi:10.3189/S0022143000011448, 1981.

Iverson, N. R.: Potential effects of subglacial water-pressure fluctuations on quarrying, Journal of Glaciology, 37(125), 27–36, doi:10.1017/S0022143000042763, 1991.

Iverson, N. R.: A theory of glacial quarrying for landscape evolution models, Geology, 40(8), 679–682, doi:10.1130/G33079.1, 2012.

Janda, R. J., Meyer, D. F. and Childer, D.: Sedimentation and Geomorphic changes during and following the 1980-1983 eruptions on Mount ST. Helens, Journal of the Japan Society of Erosion Control Engineering, 37(2), 10–21, 1984.

Johnson, M. D., Addis, K. L., Ferber, L. R., Hemstad, C. B., Meyer, G. N. and Komai, L. T.: Glacial Lake Lind, Wisconsin and Minnesota, Geological Society of America Bulletin, 111(9), 1371–1386, doi:10.1130/0016-7606(1999)111<1371:GLLWAM>2.3.CO;2, 1999.

Kleman, J.: Preservation of landforms under ice sheets and ice caps, Geomorphology, 9(1), 19–32, doi:10.1016/0169-555X(94)90028-0, 1994.

Kleman, J. and Glasser, N. F.: The subglacial thermal organisation (STO) of ice sheets, Quaternary Science Reviews, 26(5–6), 585–597, doi:10.1016/j.quascirev.2006.12.010, 2007.

Kleman, J. and Stroeven, A. P.: Preglacial surface remnants and Quaternary glacial regimes in northwestern Sweden, Geomorphology, 19(1–2), 35–54, doi:10.1016/S0169-555X(96)00046-3, 1997.

Kooi, H. and Beaumont, C.: Escarpment evolution on high-elevation rifted margins: Insights derived from a surface processes model that combines diffusion, advection, and reaction, Journal of Geophysical Research: Solid Earth, 99(B6), 12191–12209, doi:10.1029/94JB00047, 1994.

Koppes, M. and Montgomery, D. R.: The relative efficacy of fluvial and glacial erosion over modern to orogenic timescales, Nature Geoscience, 2(9), 644–647, doi:10.1038/ngeo616, 2009.

Koppes, M., Hallet, B., Rignot, E., Mouginot, J., Wellner, J. S. and Boldt, K.: Observed latitudinal variations in erosion as a function of glacier dynamics., Nature, 526(7571), 100–3, doi:10.1038/nature15385, 2015.

Lai, J. and Anders, A. M.: Tectonic controls on rates and spatial patterns of glacial erosion through geothermal heat flux, Earth and Planetary Science Letters, 543, 116348, doi:10.1016/j.epsl.2020.116348, 2020.

Lord, M. L. and Kehew, A. E.: Sedimentology and paleohydrology of glacial-lake outburst deposits in southeastern Saskatchewan and northwestern North Dakota, Geological Society of America Bulletin, 99(5), 663, doi:10.1130/0016-7606(1987)99<663:SAPOGO>2.0.CO;2, 1987.

MacGregor, K. R., Anderson, R. S., Anderson, S. P. and Waddington, E. D.: Numerical simulations of glacial-valley longitudinal profile evolution, Geology, 28(11), 1031–1034, doi:10.1130/0091-7613(2000)028<1031:NSOGVL>2.3.CO;2, 2000.

Magnússon, E., Rott, H., Björnsson, H. and Pálsson, F.: The impact of jökulhlaups on basal sliding observed by SAR interferometry on Vatnajökull, Iceland, Journal of Glaciology, 53(181), 232–240, doi:10.3189/172756507782202810, 2007.

Magrani, F., Valla, P. G., Gribenski, N. and Serra, E.: Glacial overdeepenings in the Swiss Alps and foreland: Spatial distribution and morphometrics, Quaternary Science Reviews, 243, 106483, doi:10.1016/j.quascirev.2020.106483, 2020.

Matmon, A., Bierman, P. and Enzel, Y.: Pattern and tempo of great escarpment erosion, Geology, 30(12), 1135, doi:10.1130/0091-7613(2002)030<1135:PATOGE>2.0.CO;2, 2002.

Miller, B. A., Crumpton, W. G. and Valk, A. G.: Spatial distribution of historical wetland classes on the Des Moines Lobe, Iowa, Wetlands, 29(4), 1146–1152, doi:10.1672/08-158.1, 2009.

Mitchell, S. G. and Montgomery, D. R.: Influence of a glacial buzzsaw on the height and morphology of the Cascade Range in central Washington State, USA, Quaternary Research, 65(01), 96–107, doi:10.1016/j.yqres.2005.08.018, 2006.

Molnar, P. and England, P.: Late Cenozoic uplift of mountain ranges and global climate change: chicken or egg?, Nature, 346(6279), 29–34, doi:10.1038/346029a0, 1990.

Molnar, P., Anderson, R. S. and Anderson, S. P.: Tectonics, fracturing of rock, and erosion, Journal of Geophysical Research, 112(F3), F03014, doi:10.1029/2005JF000433, 2007.

Montgomery, D. R. and Dietrich, W. E.: Channel Initiation and the Problem of Landscape Scale, Science, 255(5046), 826–830, doi:10.1126/science.255.5046.826, 1992.

Montgomery, D. R., Balco, G. and Willett, S. D.: Climate, tectonics, and the morphology of the Andes, Geology, 29(7), 579, doi:10.1130/0091-7613(2001)029<0579:CTATMO>2.0.CO;2, 2001.

Moon, S., Page Chamberlain, C., Blisniuk, K., Levine, N., Rood, D. H. and Hilley, G. E.: Climatic control of denudation in the deglaciated landscape of the Washington Cascades, Nature Geoscience, 4(7), 469–473, doi:10.1038/ngeo1159, 2011.

Moon, S., Shelef, E. and Hilley, G. E.: Recent topographic evolution and erosion of the deglaciated Washington Cascades inferred from a stochastic landscape evolution model, Journal of Geophysical Research: Earth Surface, 120(5), 856–876, doi:10.1002/2014JF003387, 2015.

Morland, L. W.: Unconfined Ice-Shelf Flow, in Dynamics of the West Antarctic Ice Sheet, edited by C. J. van der Veen and J. Oerlemans, pp. 99–116, D. Reidel Publishing Company, Dordrecht, Netherlands., 1987.

Oien, R. P., Spagnolo, M., Rea, B. R., Barr, I. D. and Bingham, R. G.: Climatic controls on the equilibrium-line altitudes of Scandinavian cirque glaciers, Geomorphology, 352, 106986, doi:10.1016/j.geomorph.2019.106986, 2020.

Perron, J. T., Dietrich, W. E. and Kirchner, J. W.: Controls on the spacing of first-order valleys, Journal of Geophysical Research, 113(F4), F04016, doi:10.1029/2007JF000977, 2008.

Pethick, J. S.: Drainage in tidal marshes, The Coastline of England and Wales, (3), 1969.

PISM, a Parallel Ice Sheet Model, [online] Available from: http://www.pism-docs.org, 2015.

Porter, S. C.: Some Geological Implications of Average Quaternary Glacial Conditions, Quaternary Research, 32(03), 245–261, doi:10.1016/0033-5894(89)90092-6, 1989.

Porter, S. C.: Snowline depression in the tropics during the Last Glaciation, Quaternary Science Reviews, 20(10), 1067–1091, doi:10.1016/S0277-3791(00)00178-5, 2000.

Prasicek, G., Herman, F., Robl, J. and Braun, J.: Glacial Steady State Topography Controlled by the Coupled Influence of Tectonics and Climate, Journal of Geophysical Research: Earth Surface, 123(6), 1344–1362, doi:10.1029/2017JF004559, 2018.

Raymo, M. E., Ruddiman, W. F. and Froelich, P. N.: Influence of late Cenozoic mountain building on ocean geochemical cycles, Geology, 16(7), 649, doi:10.1130/0091-7613(1988)016<0649:IOLCMB>2.3.CO;2, 1988.

Rhoads, B. L., Lewis, Q. W. and Andresen, W.: Historical changes in channel network extent and channel planform in an intensively managed landscape: Natural versus human-induced effects, Geomorphology, 252, 17–31, doi:10.1016/j.geomorph.2015.04.021, 2016.

Roe, G. H.: Orographic precipitation, Annual Review of Earth and Planetary Sciences, 33(1), 645–671, doi:10.1146/annurev.earth.33.092203.122541, 2005.

Roy, M., Clark, P. U., Raisbeck, G. M. and Yiou, F.: Geochemical constraints on the regolith hypothesis for the middle Pleistocene transition, Earth and Planetary Science Letters, 227(3–4), 281–296, doi:10.1016/j.epsl.2004.09.001, 2004.

Ruhe, R. V: Topographic discontinuities of the Des Moines lobe, American Journal of Science, 250(1), 46–56, 1952.

Scherler, D. and Egholm, D. L.: Production and Transport of Supraglacial Debris: Insights From Cosmogenic 10Be and Numerical Modeling, Chhota Shigri Glacier, Indian Himalaya, Journal of Geophysical Research: Earth Surface, 125(10), 1–26, doi:https://doi.org/10.1029/2020JF005586, 2020.

Schildgen, T. F., van der Beek, P. A., Sinclair, H. D. and Thiede, R. C.: Spatial correlation bias in late-Cenozoic erosion histories derived from thermochronology, Nature, 559(7712), 89–93, doi:10.1038/s41586-018-0260-6, 2018.

Schroeder, D. M., Blankenship, D. D., Young, D. A. and Quartini, E.: Evidence for elevated and spatially variable geothermal flux beneath the West Antarctic Ice Sheet, Proceedings of the National Academy of Sciences, 111(25), 9070–9072, doi:10.1073/pnas.1405184111, 2014.

Sclater, J. G., Jaupart, C. and Galson, D.: The heat flow through oceanic and continental crust and the heat loss of the Earth, Reviews of Geophysics, 18(1), 269, doi:10.1029/RG018i001p00269, 1980.

Seguinot, J., Ivy-Ochs, S., Jouvet, G., Huss, M., Funk, M. and Preusser, F.: Modelling last glacial cycle ice dynamics in the Alps, The Cryosphere, 12(10), 3265–3285, doi:10.5194/tc-12-3265-2018, 2018.

Sella, G. F., Stein, S., Dixon, T. H., Craymer, M., James, T. S., Mazzotti, S. and Dokka, R. K.: Observation of glacial isostatic adjustment in “stable” North America with GPS, Geophysical Research Letters, 34(2), L02306, doi:10.1029/2006GL027081, 2007.

Shook, K. R. and Pomeroy, J. W.: Memory effects of depressional storage in Northern Prairie hydrology, Hydrological Processes, 25(25), 3890–3898, doi:10.1002/hyp.8381, 2011.

Simon, A.: Channel and drainage-basin response of the Toutle River system in the aftermath of the 1980 eruption of Mount St. Helens, Washington, , (96–633), 1999.

Small, E. E. and Anderson, R. S.: Pleistocene relief production in Laramide mountain ranges, western United States, Geology, 26(2), 123, doi:10.1130/0091-7613(1998)026<0123:PRPILM>2.3.CO;2, 1998.

Soil Survey Staff, Natural Resources Conservation Service, U. S. D. of A.: Web Soil Survey. Available online at the following link: https://websoilsurvey.sc.egov.usda.gov/. Accessed Feb. 2018, 2018.

Soller, D. R., Price, S. D., Kempton, J. P. and Berg, R. C.: Three-dimensional geologic maps of Quaternary sediments in east-central Illinois, Geologic Investigations Series Map I-2669, 1:500,000, 1999.

Spencer, J. E. and Pearthree, P. A.: Headward Erosion Versus Closed-basin Spillover as Alternative Causes of Neogene Capture of the Ancestral Colorado River by the Gulf of California, The Colorado River: Origin and Evolution: Grand Canyon, Arizona, Grand Canyon Association Monograph, 12, 215–219, 2001.

Springer, M. and Förster, A.: Heat-flow density across the Central Andean subduction zone, Tectonophysics, 291(1–4), 123–139, doi:10.1016/S0040-1951(98)00035-3, 1998.

Steer, P., Huismans, R. S., Valla, P. G., Gac, S. and Herman, F.: Bimodal plio-quaternary glacial erosion of fjords and low-relief surfaces in Scandinavia, Nature Geoscience, 5(9), 635–639, doi:10.1038/ngeo1549, 2012.

Stern, T. A., Baxter, A. K. and Barrett, P. J.: Isostatic rebound due to glacial erosion within the Transantarctic Mountains, Geology, 33(3), 221, doi:10.1130/G21068.1, 2005.

Stichling, W. and Blackwell, S.: Drainage area as a hydrologic factor on the glaciated Canadian prairies, Prairie Farm Rehabilitation Administration, Canada., 1957.

Teller, J. T.: Controls, history, outbursts, and impact of large late-Quaternary proglacial lakes in North America, in Developments in Quaternary Science, vol. 1, pp. 45–61., 2003.

Thomson, S. N., Brandon, M. T., Tomkin, J. H., Reiners, P. W., Vásquez, C. and Wilson, N. J.: Glaciation as a destructive and constructive control on mountain building., Nature, 467(7313), 313–317, doi:10.1038/nature09365, 2010.

Tomkin, J. H.: Erosional feedbacks and the oscillation of ice masses, Journal of Geophysical Research, 108(B10), 2488, doi:10.1029/2002JB002087, 2003.

Tomkin, J. H. and Braun, J.: The influence of alpine glaciation on the relief of tectonically active mountain belts, American Journal of Science, 302(3), 169–190, doi:10.2475/ajs.302.3.169, 2002.

Tucker, G. E. and Hancock, G. R.: Modelling landscape evolution, Earth Surface Processes and Landforms, 35(1), 28–50, doi:10.1002/esp.1952, 2010.

Tulaczyk, S., Kamb, W. B. and Engelhardt, H. F.: Basal mechanics of Ice Stream B, west Antarctica: 1. Till mechanics, Journal of Geophysical Research: Solid Earth, 105(B1), 463–481, doi:10.1029/1999JB900329, 2000.

Ugelvig, S. V. and Egholm, D. L.: The influence of basal-ice debris on patterns and rates of glacial erosion, Earth and Planetary Science Letters, 490, 110–121, doi:10.1016/j.epsl.2018.03.022, 2018.

Ugelvig, S. V, Egholm, D. L. and Iverson, N. R.: Glacial landscape evolution by subglacial quarrying: A multiscale computational approach, Journal of Geophysical Research: Earth Surface, 121(11), 2042–2068, doi:10.1002/2016JF003960, 2016.

Valla, P. G., Shuster, D. L. and van der Beek, P. a.: Significant increase in relief of the European Alps during mid-Pleistocene glaciations, Nature Geoscience, 4(8), 688–692, doi:10.1038/ngeo1242, 2011.

Ward, D. J., Anderson, R. S. and Haeussler, P. J.: Scaling the Teflon Peaks: Rock type and the generation of extreme relief in the glaciated western Alaska Range, Journal of Geophysical Research: Earth Surface, 117(F1), n/a-n/a, doi:10.1029/2011JF002068, 2012.

Wayne, W. J. and Thornbury, W. D.: Glacial Geology of Wabash County, Indiana, 1951.

Whipple, K. X. and Tucker, G. E.: Dynamics of the stream-power river incision model: Implications for height limits of mountain ranges, landscape response timescales, and research needs, Journal of Geophysical Research: Solid Earth, 104(B8), 17661–17674, doi:10.1029/1999JB900120, 1999.

Whipple, K. X., Kirby, E. and Brocklehurst, S. H.: Geomorphic limits to climate-induced increases in topographic relief, Nature, 401(6748), 39–43, doi:10.1038/43375, 1999.

Willenbring, J. K. and von Blanckenburg, F.: Long-term stability of global erosion rates and weathering during late-Cenozoic cooling., Nature, 465(7295), 211–4, doi:10.1038/nature09044, 2010.

Willett, S. D.: Orogeny and orography: The effects of erosion on the structure of mountain belts, Journal of Geophysical Research: Solid Earth, 104(B12), 28957–28981, doi:10.1029/1999JB900248, 1999.

Winkelmann, R., Martin, M. A., Haseloff, M., Albrecht, T., Bueler, E., Khroulev, C. and Levermann, A.: The Potsdam Parallel Ice Sheet Model (PISM-PIK) – Part 1: Model description, The Cryosphere, 5(3), 715–726, doi:10.5194/tc-5-715-2011, 2011.

Winsor, R. A.: Environmental imagery of the wet prairie of east central Illinois, 1820–1920, Journal of Historical Geography, 13(4), 375–397, doi:10.1016/S0305-7488(87)80047-6, 1987.

Winter, T. C. and Rosenberry, D. O.: Hydrology of Prairie Pothole Wetlands during Drought and Deluge: A 17-Year Study of the Cottonwood Lake Wetland Complex in North Dakota in the Perspective of Longer Term Measured and Proxy Hydrological Records, Climatic Change, 40(2), 189–209, doi:10.1023/A:1005448416571, 1998.

Yanites, B. J. and Ehlers, T. A.: Global climate and tectonic controls on the denudation of glaciated mountains, Earth and Planetary Science Letters, 325–326, 63–75, doi:10.1016/j.epsl.2012.01.030, 2012.

Zedler, J. B.: Wetlands at your service: reducing impacts of agriculture at the watershed scale, Frontiers in Ecology and the Environment, 1(2), 65–72, doi:10.1890/1540-9295(2003)001[0065:WAYSRI]2.0.CO;2, 2003.

Zhang, P., Molnar, P. and Downs, W. R.: Increased sedimentation rates and grain sizes 2--4 Myr ago due to the influence of climate change on erosion rates, Nature, 410(April), 891–897, doi:10.1038/35073504, 2001.

Ziemen, F. A., Hock, R., Aschwanden, A., Khroulev, C., Kienholz, C., Melkonian, A. and Zhang, J.: Modeling the evolution of the Juneau Icefield between 1971 and 2100 using the Parallel Ice Sheet Model (PISM), Journal of Glaciology, 62(231), 199–214, doi:10.1017/jog.2016.13, 2016.